Curvature Correlations in Quantum Gravity

A numerical study of two-point functions in 2D CDT

Master thesis of *Jesse van der Duin*
Supervised by *prof. Renate Loll*

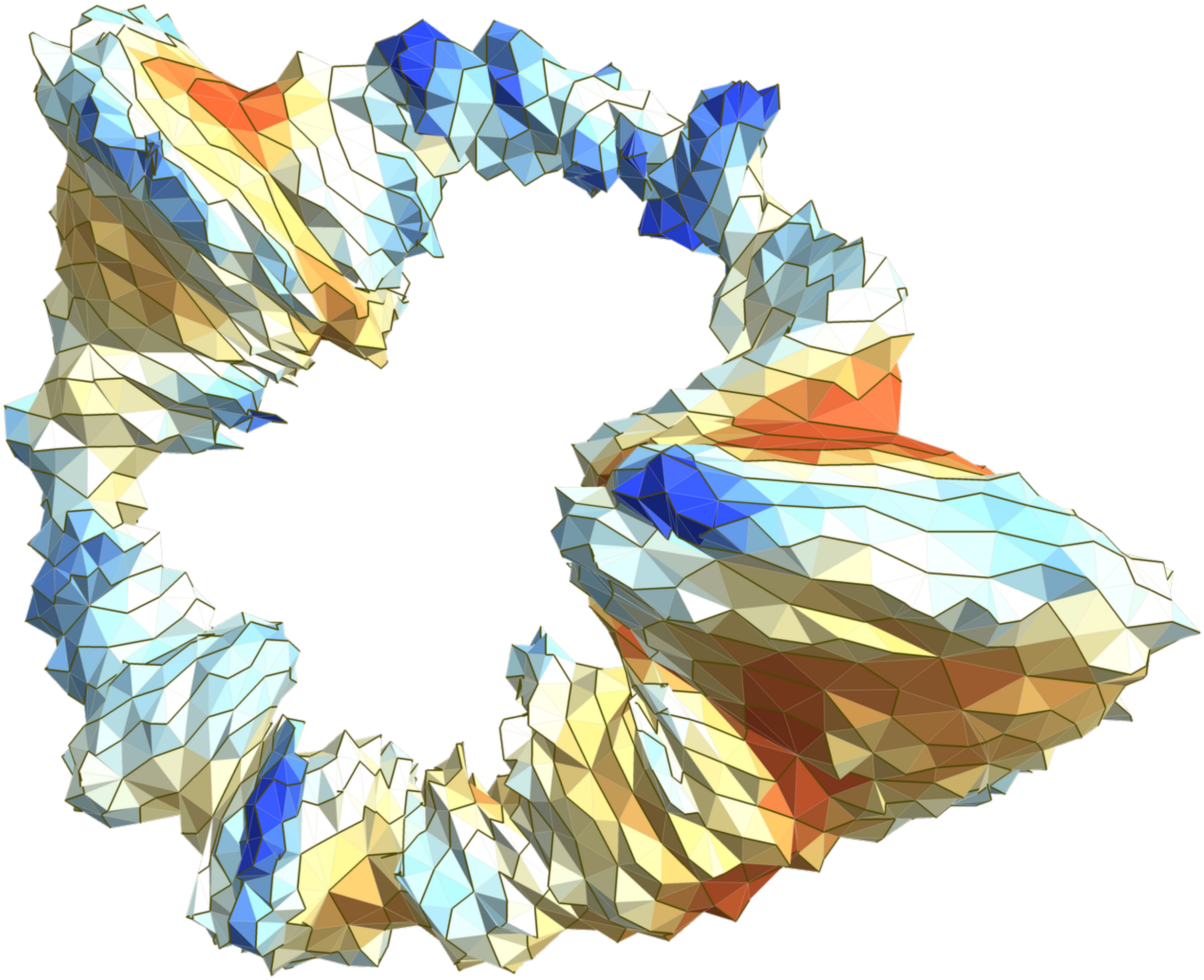

High Energy Physics, IMAPP
Radboud University Nijmegen

August 2023

Abstract

In this thesis, we present an analysis of two-point functions in quantum gravity, based on a nonperturbative path integral. Specifically, we consider the quantum gravity framework of two-dimensional causal dynamical triangulation (2D CDT). We perform a numerical study of the behaviour of curvature in 2D CDT, by measuring the two-point functions of the so-called quantum Ricci curvature. As a result we find that there are no curvature correlations in 2D CDT. Additionally, we give a detailed discussion of the computational methods used for numerical analysis in 2D CDT, based on Monte Carlo simulations, and we perform measurements of the local Hausdorff dimension and the spectral dimension.

Contents

1 Introduction 1

2 Causal Dynamical Triangulation 2
2.1 Causal triangulations . . . 2
2.2 Discretized path integral . . . 3

3 Numerical Model 5
3.1 Implementation . . . 5
3.2 Volume fixing . . . 6
3.3 Markov chain Monte Carlo . . . 7
3.4 Monte Carlo moves . . . 8
3.5 Ergodicity proof . . . 13

4 Model Verification 15
4.1 Vertex degree distribution . . . 15
4.2 Hausdorff dimension . . . 16
4.3 Spectral dimension . . . 19

5 Quantum Ricci Curvature 22
5.1 Discretization . . . 24
5.2 Implementation . . . 26
5.3 Results . . . 28

6 Topological effects 30
6.1 Cut-open triangulation . . . 32
6.2 Sphere volumes . . . 33
6.3 Average sphere distance . . . 34

7 Two-point functions 38
7.1 'Classical' two-point functions . . . 38
7.2 Quantum two-point functions . . . 47

8 QRC Correlations 51
8.1 Average sphere distance as curvature . . . 51
8.2 Results . . . 52

9 Conclusion 56

A Numerical implementation 57

B Additional material 58
B.1 Average sphere distance derivation . . . 58
B.2 Hausdorff dimension . . . 59
B.3 Distance matrix ASD . . . 59
B.4 ASD midpoint . . . 61

C Additional figures 62

1. Introduction

Quantum gravity has been a pursuit of theoretical physics for nearly a century. We are currently unable to measure physics at the Planck scale directly, but based on our understanding of quantum fields, we believe that at this scale the classical theory of General Relativity is insufficient to describe spacetime. There have been numerous attempts to describe the curved spacetimes of General Relativity with the principles of Quantum Field Theory, but so far none have succeeded. In this thesis, we will follow one candidate theory of quantum gravity called Causal Dynamical Triangulation (CDT), which is a nonpertubative lattice path integral approach, originally introduced by Ambjørn and Loll in 1998 [1]. In this framework we study two-point functions of a quantum notion of spacetime curvature, to try to gain a better understanding of the geometry of the quantum spacetimes. We perform this study in a two-dimensional toy model of CDT, to allow us to make a first investigation into the two-point functions of quantum curvature, without the complications of the higher-dimensional theory, such that our insights can be used for the study of curvature in the full four-dimensional theory.

First, chapter 2 gives a short overview of the (for this thesis) relevant points of the theory of 2D CDT, to set the scene for the following chapters. Chapter 3 continues with a detailed description of the numerical model used to computationally simulate 2D CDT, based on Markov chain Monte Carlo methods. This chapter also aims to serve as a reference for those who wish to perform their own numerical simulations, by highlighting some details that should be considered in an implementation and what choices we made. Chapter 4 presents the measurement results for some standard observables: vertex degree distribution, Hausdorff dimension and spectral dimension. The measurements are performed as a consistency check for our numerical model, as well as serving as a reference of the numerical results of these observables in 2D CDT, which are infrequent in the literature. Next, chapter 5 discusses a notion of curvature called *quantum Ricci curvature* based on average sphere distance, as first presented by Klitgaard and Loll [2]. The construction of this notion of curvature is introduced, and the average curvature measured for 2D CDT. Additionally, the complications that arise with the numerical measurements due to sampling and the required computational effort of the curvature measurements are discussed. Thereafter, chapter 6 discusses the topological effects of the measurement results that arise due to the compact geometry. A method is presented to determine a length scale range where topological effects are largely absent. Chapter 7 presents two-point functions in a quantum gravity setting based on a nonperturbative path integral. It focusses on the difficulties that arise in defining two-point functions, because of the need for diffeomorphism invariance, the non-uniform geometry of quantum spacetime, and the potential non-commutativity of the manifold and ensemble averages. It also discusses how to make numerical estimates of these two-point functions, and the complications that arise due to sampling. This is followed by chapter 8, which presents the measured two-point functions of quantum Ricci curvature in 2D CDT. Finally, chapter 9 concludes this thesis, giving an overview of the main results. Additionally, appendix A presents our open-source implementation of the numerical model that was used for the simulation and measurements of this thesis. The implementation includes extensive documentation with the aim to provide a useful reference to those who wish to make their own (C)DT simulations, or use (parts of) our implementation.

2. Causal Dynamical Triangulation

THIS chapter provides a short introduction to the theory of CDT (Causal Dynamical Triangulation) and will mainly be concerned with introducing and defining the terms and expression necessary for the following chapters. This is not a full explanation of (Causal) Dynamical Triangulation; for a more complete overview we refer to [3] or to [4] for a complete discussion.

CDT is a nonperturbative path integral approach to quantum gravity, which is to say that it provides a method of calculating the gravitational path integral

$$Z = \int_{\mathcal{M}} \mathcal{D}[g_{\mu\nu}]\, e^{iS_{\mathrm{EH}}[g_{\mu\nu}]}, \tag{2.1}$$

where the path integral is over all geometries represented by four-metric $g_{\mu\nu}$, where $\mathcal{D}[g_{\mu\nu}]$ denotes the measure over all equivalence classes of the metric under diffeomorphism, since we only want to integrate over inequivalent *geometries* without the redundancy of coordinates. We consider pure gravity (vanishing stress-energy tensor) using the *Einstein-Hilbert action*

$$S_{\mathrm{EH}} = \frac{1}{16\pi G_N} \int d^4x\, \sqrt{-g(x)}\big(R - 2\Lambda\big), \tag{2.2}$$

where we have a volume integral with metric determinant[1] $g(x)$, Ricci scalar R, cosmological constant Λ and Newton's gravitational constant G_N. First we explain how in the two-dimensional toy model we consider, spacetime is represented by something we call causal triangulations. Then we discuss how these triangulations can be used to regularize and calculate the gravitational path integral (2.1).

2.1 Causal triangulations

Causal Dynamical Triangulation gives a lattice discretization of Lorentzian spacetime as a way to approximate the curved geometries. This provides a regularization method for the gravitational path integral (2.1) by interpreting the smallest length unit of the discretization as a lattice UV cutoff a, and taking a continuum limit by $a \to 0$.

In 2D CDT these geometric lattices take the form of 2-dimensional simplicial manifolds T_2 with a *sliced* structure built up from fixed 2-dimensional *building blocks*. For 2D CDT we use only a single building block, which is a triangular piece of flat Minkowski space, with one spacelike edge with (square) edge length[2] $a_s^2 = a^2$ and two timelike edges with $a_t^2 = -\alpha a^2$ where $\alpha > 0$, as displayed on the left side of Fig. 2.1. These triangles can be "glued" together to create a simplicial manifold, called a *triangulation*. We only allow gluing of spacelike to spacelike and timelike to timelike edges, and allow at most two spacelike edges to meet in each vertex.

Using only this building block gives rise to [5] *spatial slices* (also called *time-slices*) that are 1-dimensional "spatial hypersurfaces" $T_1(t)$ of constant proper time $t = 1, 2, \dots$; five of these spatial slices are displayed on the right of Fig. 2.1 with the red edges forming a circle (left and right sides are identified). Each of these *spatial slice*s form a 1-dimensional simplicial manifold itself, which we will fix to have a spherical topology; each spatial slice is simply a circle of vertices connected with spacelike edges.

Now, consider the simplicial submanifold connecting $T_1(1)$ and $T_1(2)$ with the discussed building block, which we call a *slab*. The triangular building block can have two orientations: one where the spacelike edge is on the past side of the triangle, i.e. part of $T_1(1)$; and the time reversal where

---

[1] Note we use the spacelike $(-,+,+,+)$, or $(-,+)$ in 2D, metric signature convention in this thesis.

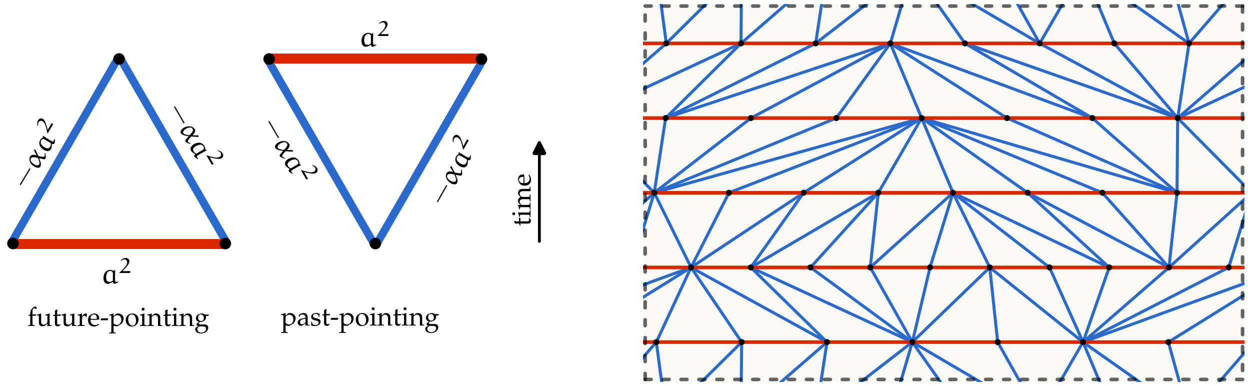

Figure 2.1: *Left*: CDT triangular building blocks; pieces of flat Minkowski space with spacelike and timelike edges highlighted in red and blue respectively with their (square) lengths. *Right*: An example triangulation of $N_2 = 80$ and $\tau = 5$ with periodically identified time and highlighted edges; note that the left and right sides of the figure should be identified as well as the top and bottom.

the spacelike edge is on the future side of the triangle, i.e. part of $T_1(2)$. We will call these triangles the *future-pointing* triangle, and the *past-pointing* triangle respectively, as displayed on the left side of Fig. 2.1.

We will call τ the number of time-slices in a triangulation T_2, where we choose to identify time periodically[3] for convenience in numerical simulations, such that $T_1(1) = T_1(\tau + 1)$. Furthermore, we will denote the number of k-simplices with N_k; so a triangulation T_2 has N_0 vertices, N_1 edges and N_2 triangles. For numerical simulations the relative number of spatial slices to the total number of vertices is important, so we will define the ratio[4] $\daleth = \tau^2/N_0$ expression the relative "length" of the triangulation.

Finally, we require all triangulations to obey the *simplicial manifold condition* [6]. For 2D CDT this means we forbid the occurrence of spatial slices with length $l \leqslant 2$, i.e. each spatial slice must have at least three edges. The same condition can also be viewed as requiring at least three future-pointing and three past-pointing triangles in each slab of the triangulation.

2.2 Discretized path integral

By approximating Lorentzian manifolds with these triangulations we can discretize the gravitational path integral (2.1). Moreover, we are able to perform a Wick rotation to Euclidean signature, yielding triangles that are pieces of Euclidean space. This is essentially achieved by performing the rotation $\alpha \mapsto -\alpha$; see [4, p. 30] for a proper discussion. After Wick rotation we set $\alpha = 1$, such that the Euclidean triangles are equilateral with edge lengths a. In the end we get the 2D CDT Wick-rotated Euclidean path integral, or partition function

$$Z_{\mathrm{CDT}} = \sum_{T \in \mathcal{T}} \frac{1}{C(T)} e^{-S_{\mathrm{CDT}}(T)}, \tag{2.3}$$

where $\mathcal{T}$ denotes the ensemble of all Wick-rotated CDTs (in our case with toroidal topology), i.e. all Euclidean triangulations with the causal structure dictated by the causal gluing rules obeying the simplicial manifold condition as explained earlier. Note that these causal gluing rules make the ensemble $\mathcal{T}$ different from the ensemble of all Euclidean triangulations without restrictions, also called EDT (Euclidean Dynamical Triangulation). The $C(T)$ is a symmetry factor, specifically the number of elements of the automorphism group of triangulation T; see [4, p. 33] for more details.

---

[3] Alternatively one could have fixed boundaries $T_1(1)$ and $T_1(\tau)$ as is usually done in theoretical treatments.

[4] Note: the $\daleth$ symbol is a letter in the Hebrew alphabet called 'daleth'.

The Euclidean CDT action S_{CDT} is the Wick-rotated discretization of the Einstein-Hilbert action $S_{\mathrm{EH}}[g_{\mu\nu}]$ (2.2), and is given by

$$S_{\mathrm{CDT}} = \lambda N_2(T), \tag{2.4}$$

where λ is the rescaled dimensionless cosmological constant and $N_2(T)$ the number of triangles of T. We take the continuum limit of the partition function by letting $a \to 0$ and $N_2 \to \infty$, while keeping the continuum volume $N_2 a^2 = \mathrm{const}$. This is achieved by tuning λ to its critical value, analytically known to be $\lambda_c = \ln 2$, such that in the continuum limit we obtain

$$\lambda \to \lambda_c + \Lambda a^2 + \mathcal{O}(a^3),$$

where Λ is the physical cosmological constant.

Note that S_{CDT} only contains the volume term of the Einstein-Hilbert action and not the curvature term. This is because the integrated curvature is 0 in two dimensions by the Gauss-Bonnet theorem [4]. In the discretized setting the geometry is restricted by the Euler characteristic formula

$$N_2 - N_1 + N_0 = \chi,$$

where χ is called the Euler characteristic and is fixed by the topology; $\chi = 0$ for a toroidal topology.

Finally, we note that the triangulations in $\mathcal{T}$ are naturally without coordinates or labels, so these triangulations are by construction already diffeomorphism-invariant. However, we can also consider labelled triangulations, which is how we work with the triangulations in a numerical simulation. For example, if we label each triangle[5] we get the Euclidean partition function

$$Z_{\mathrm{CDT}} = \sum_{T_l \in \mathcal{T}_l} \frac{1}{N_2(T_l)!} e^{-S_{\mathrm{CDT}}(T_l)}. \tag{2.5}$$

Here $\mathcal{T}_l$ is the ensemble of all distinct *labelled* triangulations, and we have an additional factor of $N_2(T)!$, which divides out the number of ways to relabel a triangulation.

With these partition functions we are now able to determine expectation values observables of the triangulation $\mathcal{O}(T)$ as

$$\langle \mathcal{O} \rangle = \frac{1}{Z} \sum_{T \in \mathcal{T}} \mathcal{O}(T) \, \frac{1}{C(T)} e^{-S(T)} = \frac{1}{Z} \sum_{T_l \in \mathcal{T}_l} \mathcal{O}(T_l) \, \frac{1}{N_2(T_l)!} e^{-S(T_l)}. \tag{2.6}$$

We now drop the CDT subscript, as will be done in the rest of this thesis unless otherwise specified. By determining the expectation values of interesting observables $\mathcal{O}$, we are able to analyse the properties of 2D CDT. We will discuss some interesting observables in the following chapters, but first we discuss how we can study CDT numerically, for which dynamical triangulation is very well suited because of its combinatorial and computational nature.

---

[5] In our numerical model this is how we represent the triangulations.

3. Numerical Model

Numerical methods allow us to study two-dimensional Causal Dynamical Triangulations using more complicated quantities like quantum Ricci curvature[1], which is (currently) unavailable analytically due to its quasi-local nature. Moreover, this two-dimensional "toy model" serves as good testing ground for the fully fledged 4D CDT.

In order to numerically study dynamical triangulations we can compute expectation values (2.6) by summing over all (labelled)[2] triangulations. However, computationally we are not able to actually sum over all triangulations as there are far too many and the number of them grows exponentially with N_2. Instead, we use Monte Carlo methods, which in a nutshell entails estimating expectation values by using the sample average of a limited sample of triangulations from the ensemble. That is we wish to generate a sample $\Sigma_m = \{T_{l,1}, T_{l,2}, \ldots, T_{l,m}\} \subset \mathcal{T}_l$ of m labelled triangulations, each of which follows the same probability distribution

$$\mathcal{P}(T_l) = \frac{1}{Z}\frac{1}{N_2(T_l)!}\, e^{-S(T_l)} = \frac{1}{Z}\frac{1}{N_2(T_l)!} e^{-\lambda N_2(T_l)}. \tag{3.1}$$

We can then estimate the ensemble average $\langle O \rangle$ of an observable O using the sample average

$$\hat{O}_m \coloneqq \frac{1}{m}\sum_{i=1}^{m} O(T_{l,i}), \tag{3.2}$$

which serves as an unbiased estimator[3] for $\langle O \rangle$, whose uncertainty vanishes for $m \to \infty$:

$$E\left[\hat{O}_m\right] = \langle O \rangle, \qquad \lim_{m\to\infty} E\left[\left(\hat{O}_m - \langle O \rangle\right)^2\right] = 0.$$

The details of how such a sampling can be achieved are discussed later in this chapter. First, we turn our attention to renormalization and using a fixed-volume ensemble. Note that for the numerical model we only consider labelled triangulations, as this is how they are stored on a computer when they are simulated. To avoid clutter we will suppress the subscript l denoting the use of labelling, but all triangulations should be considered labelled unless otherwise specified.

3.1 Implementation

We will not discuss the full details of the implementation of the Monte Carlo simulation, but we will present some of the details which are important for the rest of this section. For further information on our implementation, see appendix A. Firstly, we consider triangulations with a toroidal topology and a fixed number of spatial slices τ; we compactify both the spatial and time-direction. Computationally this is more convenient to work with than fixed boundaries $T_1(1)$ and $T_1(\tau)$, and we do not have the additional problem of choosing appropriate boundary sizes. To represent the triangulation, we store the triangles with their connectivity. Specifically, we store an ordered list where each element of the list represents a triangle, which contains the label of its *left*, *right*[4] and *timelike* neighbour, as well as its *orientation* (future- or past-pointing). This list then uniquely represents triangle-labelled triangulation. However, for measurement of observables we are also interested in the geometry of the vertex graph, for which the connectivity of the vertices must be known. So, for every measurement we need to reconstruct the vertex connectivity from the triangle connectivity, which adds a non-negligible computational cost. Alternatively one might choose to label the vertices instead and keep track of the vertex connectivity; this has the downside that the number of vertex neighbours is not constant while each triangle always has three neighbours. So, we label the triangles, justifying the use of $\mathcal{T}_l$ as the ensemble of triangulation with labelled triangles.

---

[1] This quantity [2] will be introduced in section 5.

[2] When we simulate the numerical model on a computer the triangulations are labelled because they are stored with a labelling; in our case we chose to label the triangles. So for this chapter we will be working with labelled triangulations as we indicate by the l subscript T_l.

[3] We will use the notation $E[\cdots]$ for the statistical expectation value.

3.2 Volume fixing

In order to obtain the infinite-volume limit of the theory, we have to tune λ to its critical value λ_c. Numerically we should fix $\lambda > \lambda_c$ such that the relevant contributions to the sum have a finite (two-)volume N_2; and systematically decrease λ toward λ_c until large enough volumes are reached to get a reasonable estimate of the continuum limit. While this is possible, it is computationally far more effective to fix the total volume N_2. We can perform simulations at increasingly large fixed volumes N_2, checking to see if there are still finite-size effects or the infinite-volume limit is already closely approximated [4].

Formally we switch to an ensemble of all triangulations with constant volume. Analytically, this can be achieved by a Laplace transform:

$$Z = \sum_{N}^{\infty} e^{-\lambda N} Z_N, \tag{3.3}$$

where Z_N is the partition function of constant two-volume N. The constant-volume partition function is special in 2D in that all its configurations have equal weight. Ensemble averages are computed in this ensemble with the expectation value

$$\langle O \rangle_N = \frac{1}{Z_N \, N!} \sum_{T \in \mathcal{T}_N} O(T), \tag{3.4}$$

where $\mathcal{T}_N$ denotes the ensemble of all labelled triangulations with constant volume. So, this constant-volume ensemble average can be estimated by taking the sample average of a sample from only triangulations with the desired volume N.

So, instead of finding a sampling method that samples all triangulations, we should find a method which only samples triangulations with a given volume N. For 2D CDT this is possible, and this method will be presented in the following section. However, in general and for higher-dimensional models such a sampling method is a lot more difficult to find. Instead, one can add a volume-fixing constraint to the action, usually of the quadratic form [7]

$$S_E \to S_E + \delta S = \lambda N_2(T) + \epsilon \Big(N_2(T) - \hat{N}_2 \Big)^2, \tag{3.5}$$

where $\hat{N}_2$ is the desired volume, and $\epsilon > 0$ is a constant controlling the strength of the constraint. The volume-fixed probability distribution for triangulations then becomes

$$\mathcal{P}(T) = \frac{1}{Z \, N_2(T)!} e^{-\lambda N_2(T) - \epsilon \left(N_2(T) - \hat{N}_2 \right)^2}. \tag{3.6}$$

---

[4] Note that we are able to distinguish the left and right neighbours as we have a distinguished forward time direction. Specifically, right is chosen to be the direction, such that a rotation from right to future-pointing is positive on the toroidal surface.

From this probability distribution we can see that for large ϵ this constraint assigns a low probability to sample triangulations with volumes away from $\hat{N}_2$, such that only samples with the correct volume can be used for measurements without wasting many samples on unwanted volumes. In principle one would want to have the ϵ as large as possible to have the volume distribution as narrow around the desired volume as possible. However, the way the samples are made requires the distribution to have some fluctuations of volume to remain ergodic and be an effective sampling method, so there will be a largest possible ϵ after which the results start to be affected. So one has to tune ϵ to give a narrow distribution whilst making sure the results are independent of this choice. Additionally, for a given volume one needs to tune[5] λ to its pseudo-critical value (this depends weakly on the volume) [4], to keep the probability distribution of the sampled volumes symmetric around $\hat{N}_2$.

3.3 Markov chain Monte Carlo

Now we turn to the problem of sampling triangulations. Preferably we want some method of sampling a triangulation directly following probability distribution (3.1), that is, constructing a random triangulation from scratch for every sample, as this is usually the fastest way to sample. However, it is very challenging to construct such a method as the structure of the triangulations is rather complex; this is even more the case for higher dimensions. So, usually a different method is used called *Markov chain Monte Carlo* [9, 10]. In this method we start with a triangulation that is constructed by hand. This is usually a very regular triangulation, which is far from a typical triangulation, as these are simpler to construct. From this starting triangulation we can transition to other triangulations by making 'small' changes to the triangulation $T \to T'$, called *moves*. Repeated application of these moves yields a sequence of triangulations $\{T_0, T_1, \dots\}$, which form a Markov chain, hence the name. This Markov chain effectively explores the ensemble, by walking through it using the moves. Then to generate triangulations with the desired probability distribution (3.1), we assign a *transition probability* $\Pi(T \to T')$ to each move, which must obey the following properties:

- *Ergodicity*: Every triangulation in the ensemble must be reachable by a finite number of moves with non-zero probability.
- $\Pi(T \to T')$ must be chosen such that the distribution of the limiting triangulation of the Markov chain is stationary and follows the desired distribution, i.e. $\lim_{n\to\infty} P(T_n) = \mathcal{P}(T)$.

Here $P(T_n)$ denotes the probability distribution of the triangulation, which is obtained after performing n Markov chain moves, and $\mathcal{P}(T)$ denotes the desired probability distribution of the triangulations, in our case (3.1) or (3.6). The ergodicity condition must be checked for the chosen move set to be certain the full ensemble is being sampled, and this will be done for the presented moves. We will use the standard *detailed balance* condition to ensure the second property is obeyed, for which Π must satisfy

$$\mathcal{P}(T)\Pi(T \to T') = \mathcal{P}(T')\Pi(T' \to T). \tag{3.7}$$

In order to perform a move we must have some way of selecting a specific move with some probability, which may be different from the required transition probability Π. We will call this the selection or *proposal probability* $S(T \to T')$ of the proposed move $T \to T'$. To obtain the required transition probability we will only accept the proposed move with some *acceptance probability* $A(T \to T')$. The move will only be performed if it is accepted, otherwise it will be rejected. Rejection means the proposed move is not performed but instead the 'identity' move, which leaves the triangulation unchanged. We obtain the transition probability: $\Pi(T \to T') = A(T \to T')\, S(T \to T')$, and for a given $S(T \to T')$ we then have to find an $A(T \to T')$ such that detailed balance (3.7) is obeyed. This acceptance probability is not unique. We will choose it such that it is maximal (so there are as few rejections as possible), which is called the *Metropolis-Hastings acceptance probability* [11], given by

---

[5] We did not actually use this method for this research project. As such, the tuning procedure will not be explained any further; see for example [8] for more details.

$$A(T \to T') = \min\left(1, \frac{S(T' \to T)}{S(T \to T')} \frac{\mathcal{P}(T')}{\mathcal{P}(T)}\right) = \min\left(1, \frac{S(T' \to T)}{S(T \to T')} \frac{N_2(T)}{N_2(T')} e^{\lambda(N_2(T)-N_2(T'))}\right), \quad (3.8)$$

where we have used probability distribution (3.1) without volume fixing. Often, one has some freedom in the method used to propose moves. It is usually preferable to pick the method with the proposal probability S that yields the largest acceptance probability A, such that the least amount of computation time is spent on computing moves that get rejected.

Finally, there are few practical issues[6] to consider. In practice, we cannot perform an infinite number of moves to obtain samples. Instead, we perform a limited number of moves until it seems the samples are practically distributed like the desired stationary distribution. This is called *thermalizing* or *equilibrating* the simulation, and the number of moves it takes to reach this point is referred to as the *equilibration time*. Depending on how 'far from typical' the starting triangulation is this can take more or less moves. So, if we know the equilibration time we only use samples from after the equilibration time to ensure the samples have the correct probability distribution. Secondly, the moves that are typically used make only very minor changes to the triangulation T, such that an observable $O(T)$ after a move will likely yield a very similar result. This means that consecutive triangulation samples in the Markov chain are not identically independently distributed[7]. This means that observable measurements $O(T_i)$ and $O(T_i')$ are highly correlated if the number of moves $|i' - i|$ between them is small. These correlated triangulations do not improve the statistical error of the sample average much. So, if we wish to determine a good estimate of the ensemble average we should attempt to only perform measurements on triangulations that are not correlated. After many small moves however, the resulting triangulation will be significantly different. The number of moves it takes for the triangulations to be effectively independently distributed is called the *correlation time*, which can be estimated by measuring the autocorrelation over Markov chain steps of the observable of interest. So instead of making measurements after every move, we will only make them after every k moves, where we choose k to be close to the correlation time.

3.4 Monte Carlo moves

Now, we present moves that can be used to perform Markov chain Monte Carlo on 2D CDT, and compute the acceptance probabilities of those moves. Several options of moves are presented, that we do not use in our simulation, but are included to provide the reader with an overview of some possible options. The last of these moves is a volume-preserving move, which to our knowledge has not been previously presented in the literature.

3.4.1 Shard move

A single move that is ergodic is the one presented in Fig. 3.1, which we will call the *shard move* [12]. For this move a shard (two oppositely oriented triangles, sharing a spacelike edge) is collapsed to two connected timelike edges by collapsing the spacelike edge to a vertex. Or conversely, two connected timelike edges that are part of different slabs[8] and their connecting vertex are split into two, creating a spacelike edge connecting two triangles. This move can be implemented by

---

[6] An accessible discussion of these issues is presented in the lecture notes of the course: *Monte Carlo Techniques* of Timothy Budd, at Radboud University, `https://hef.ru.nl/~tbudd/mct/lectures/mcmc_in_practice.html`

[7] They are identically distributed after thermalization but not independent.

[8] We remind the reader a slab is simplicial manifold between two adjacent spatial slices, see chapter 2.

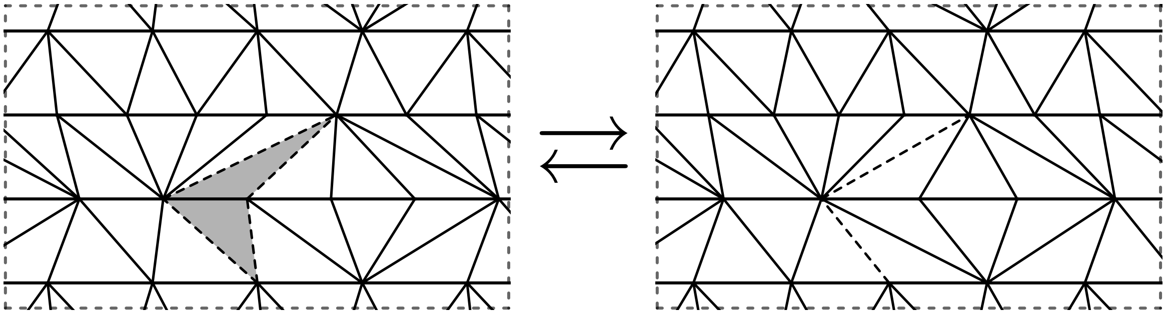

Figure 3.1: Illustration of the *shard move* in a triangulation.

uniformly selecting a triangle and collapsing the shard it is part of, or conversely by uniformly selecting two connected timelike edges that belong to adjacent slabs, splitting them and creating two new triangles in between. This inverse move is computationally expensive to implement for us, as we only keep track of the triangle connectivity, not having direct access to the existing edges and their connections. A search of the local neighbourhood would be necessary to implement this move with our setup, which makes it computationally unfavourable. Note that it is possible to violate the simplicial manifold condition with this move, as it can create spatial slices with less than three vertices. So after every move the simplicial manifold condition has to be checked, rejecting the move if it is not satisfied. Finally, note that the shard move is ergodic [12] without the need for additional moves.

3.4.2 Flip move

The standard move used for Euclidean Dynamical Triangulation (EDT) [13], where there is no foliated structure, is to flip an edge. Given a pair of triangles which share two vertices, flip the connecting edge such that the other vertices are now shared. In EDT this move can be performed on any edge and is ergodic for the constant-volume ensemble. However, in 2D CDT we cannot perform this flip move on space-like edges as this would create triangles that are not part of the CDT prescription. Hence, in CDT we are restricted to performing the flip move on timelike edges. So, the *flip move* of CDT amounts to flipping a timelike edge, as visualized in Fig. 3.2. Effectively this move swaps two neighbouring triangles with opposite orientation (one future- and one past-pointing).

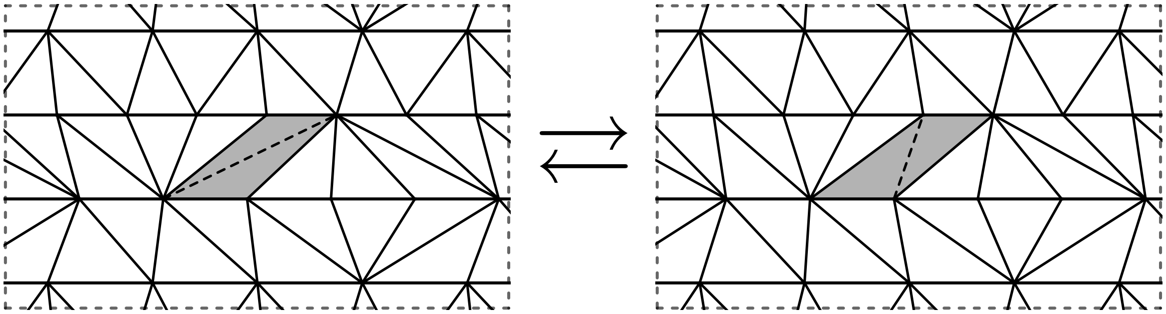

Figure 3.2: Illustration of the *flip move* in a triangulation.

This move can be selected in two ways. We could uniformly select a triangle a, with which we associate the pair consisting of triangle a and its left neighbour b, and flip the triangle pair a, b if they have opposite orientations, otherwise we reject the move. This satisfies detailed balance (3.7) without needing any additional rejections, meaning the acceptance probability is $A(T \to T') = 1$. This follows from the fact that the volume N_2 remains constant (so $\mathcal{P}(T) = \mathcal{P}(T')$) and selection probability[9] $\Pi(T \to T') = \Pi(T' \to T) = 1/N_2$. Selecting triangles in this was has an overall rejection rate of around 0.5^{10}., due to the rejection when selecting a triangle that is not associated with a flip pair. Alternatively, one could keep a list of all the 'flip pairs' and uniformly sample a pair from that list, giving a proposal probability $S(T \to T') = 1/n_f(T)$, with $n_f(T)$ denoting the number of flip pairs in triangulation T. In this case we satisfy detailed balance (3.7) by using the Metropolis-Hastings acceptance probability

$$A(T \to T') = \begin{cases} 1 & \text{for } \big(n_f(T') - n_f(T)\big) \leqslant 0 \\ \dfrac{n_f(T)}{2 + n_f(T)} & \text{for } \big(n_f(T') - n_f(T)\big) = 2. \end{cases} \tag{3.9}$$

Note that n_f can only change with $-2, 0,$ or $+2$. Now, since the expectation value of n_f is[10] $N_2/2$ this method gives a small rejection rate for large volumes. However, it brings the additional cost of keeping track of a list. We opted for the first option.

Finally, in CDT this flip move is not ergodic on its own, unlike for EDT with fixed volume. It obviously does not change the volume, so it is definitely not ergodic in the ensemble $\mathcal{T}$ of all triangulations. Moreover, it also does not change the number of vertices in each spatial slice, making it also not ergodic in the ensemble $\mathcal{T}_N$ of triangulations with constant volume.

3.4.3 Diamond move

The flip move on its own is not ergodic, as discussed. So we introduce an additional move [4], which we call the *diamond move*; a diagram of the move is presented in Fig. 3.3. We select a diamond (a set of four triangles that fully surround a vertex, meaning that the degree of this vertex must be 4) and collapse it to a shard, effectively removing the interior two timelike edges. Conversely, we select a shard which can be split up in two, forming a diamond. Like the shard move, the diamond move can create triangulations that violate the simplicial manifold condition, as it can create spatial slices with less than three vertices. So, we need to check this condition after every proposed move, and reject the move if it violates the condition[11].

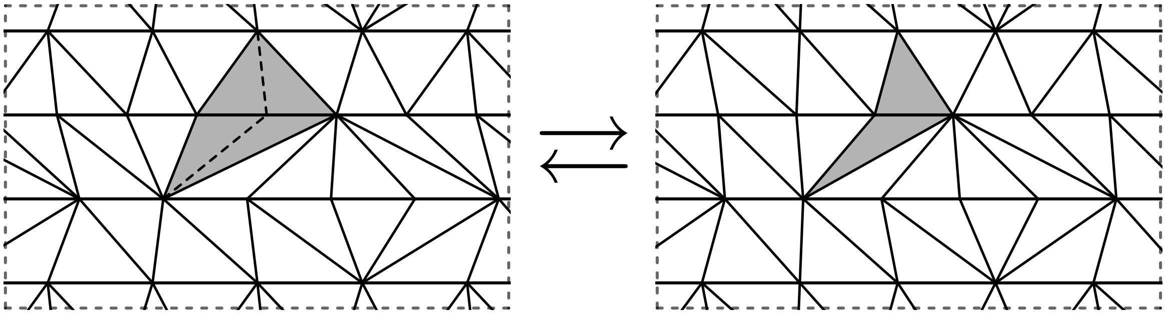

Figure 3.3: Illustration of the *diamond move*.

The diamond move with its inverse are not ergodic on their own. For example, it is impossible to go from a triangulation with no vertices with degree 4 to a triangulation with smaller volume. This is because the diamond move only removes a degree 4 vertex and its inverse creates just one.

---

[9] Since the acceptance probability is 1, the selection probability is directly identical to the proposal probability.

[10] Using the known distribution of future-pointing vertex neighbours (4.1) and the fact that 1 neighbour contributes no flip pairs and $\geqslant 2$ neighbours contribute 2 flip pairs, one easily obtains $\langle n_f \rangle = N_2/2$. So half the triangles are associated with flip pairs, meaning that the probability of selecting one is 0.5.

[11] By mistake, we did not check this condition in the simulation we performed. So in principle triangulations could have been created with spatial slices with lengths as small as 1. However, this should have a negligible effect on the systems we considered, as we discuss in the conclusion, chapter. 9.

So, a combination of these moves can never go to a triangulation with smaller volume. However, the diamond move together with the flip move does give us an ergodic[12] move set, see [4].

The selection for this move can be implemented by uniformly selecting a triangle and proposing the diamond move if there is a diamond associated with that triangle, otherwise we reject the move. In our implementation we associate both of the right triangles to the diamond. This association gives an expected[13] fraction of $\frac{1}{4}$ of triangles to be associated with a diamond, so we expect to be able to perform this move on $\frac{1}{4}$ of the selected triangles. The inverse move can be selected easily by uniformly selecting a triangle and using the shard it is a part of, then adding the shard to its right. So, we get the selection probabilities $P(T \to T') = 2/N_2(T)$ and $P(T' \to T) = 2/N_2(T')$ for the move and its inverse respectively. To get a higher acceptance probability, we will also reassign all labels after performing the moves, i.e. performing a random relabelling of all triangles; so each relabelled triangulation T has a probability of $1/N_2(T)!$ of getting selected. This way a labelled triangulation can reach any labelled triangulation that corresponds to the abstract triangulation after the move. So with the reassigning of the labels, the new selection probabilities become $P(T \to T') = 2/\big(N_2(T)N_2(T')!\big)$ and $P(T' \to T) = 2/\big(N_2(T')N_2(T)!\big)$ for the diamond move and its inverse respectively. To satisfy detailed balance (3.7) with the desired volume-fixed probability distribution (3.6) we use the Metropolis-Hastings acceptance probabilities

$$A(T \to T') = \min\left(1, \frac{N_2(T)}{N_2(T)-2}\, e^{2\lambda+4\epsilon\left(N_2(T)-\hat{N}_2-1\right)}\right), \tag{3.10}$$

$$A(T' \to T) = \min\left(1, \frac{N_2(T')}{N_2(T')+2}\, e^{-2\lambda-4\epsilon\left(N_2(T')-\hat{N}_2+1\right)}\right), \tag{3.11}$$

using the fact that $N_2(T) = N_2(T') + 2$. To get the acceptance probabilities for the normal action without volume fixing simply take $\epsilon = 0$. Note that these acceptance probabilities assume the diamond move and its inverse are proposed equally often. This is not necessary, and one could change the proposal probabilities to get less rejections in some cases.

Alternatively, we could also keep a list of the diamonds[14] and uniformly sample a diamond from that list, giving proposal probability $S(T \to T') = 1/n_d(T)$, with $n_d(T)$ denoting the number of diamonds in T. Naturally, the inverse proposal probability $S(T' \to T) = 1/N_2(T')$ remains the same. Then, using the same reassignments of the labels, we obtain the Metropolis-Hastings acceptance probabilities

$$A(T \to T') = \min\left(1, \frac{n_d(T)}{N_2(T)-2}\, e^{2\lambda+4\epsilon\left(N_2(T)-\hat{N}_2-1\right)}\right), \tag{3.12}$$

$$A(T' \to T) = \min\left(1, \frac{N_2(T')}{n_d(T')+1}\, e^{-2\lambda-4\epsilon\left(N_2(T')-\hat{N}_2+1\right)}\right), \tag{3.13}$$

using the fact that $n_d(T) = n_d(T') + 1$. Note that this way of proposing moves with an additional list has an overall acceptance rate that is close to 1 for both the move and its inverse, when the volume N_2 is near the desired $\hat{N}_2$. So we get very few rejections when the simulation is in equilibrium. In contrast, the previous method without a list of diamonds has an overall acceptance rate close to 0.25 in equilibrium. Hence, depending on the additional computational cost of keeping the list of diamonds in one's implementation, one or the other method may be desirable.

---

[12] One can see this fairly easily by showing that a combination of flip and diamond moves can be used to give the same transition as a shard move. Flip moves can be used to create a diamond at the place of the shard, then the diamond move can be performed, and finally the flip moves can be used again to restore the rest of the triangulation to its original state. The inverse move can be reproduced in an analogous way.

[13] To see where this expectation value comes from, we can uniquely associate the centre vertex with degree 4 to each diamond. So, the fraction of vertices associated with a diamond is precisely the fraction of vertices with degree 4. The distribution of vertex degrees is known (4.3), giving $2\langle n_d \rangle = N_2/4$ where n_d denotes the number of diamonds.

[14] For our implementation we keep a list of the future-pointing triangle of the right shard of the diamond.

3.4.4 Relocation move

Combining the flip move and diamond move, we have an ergodic move set that can be used efficiently in our implementation, where we keep track of the triangle connectivity. However, this move set will still require volume fixing, while it is preferable to have a sampling that only samples from a fixed volume ensemble. So we propose another move, which keeps the total volume fixed, and – to the best of our knowledge – has never been used in literature[15]. We will call this move the *relocation* move as it effectively relocates a diamond to another location in the triangulation. For this move a diamond and a shard have to be selected. Then the diamond gets collapsed into a shard; and the shard gets expanded into a new diamond. Effectively this is the same as performing the diamond move and immediately thereafter performing the inverse diamond move, which will keep the overall volume constant. A diagram of this move is presented in Fig. 3.4.

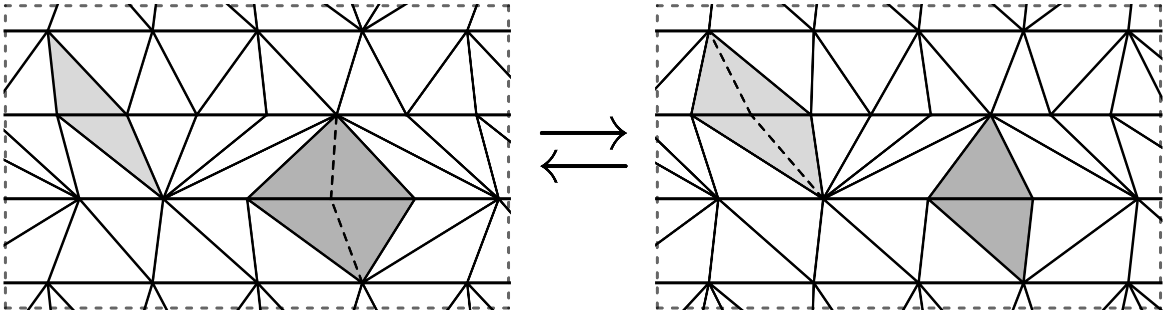

Figure 3.4: Illustration of the *relocation move* in a triangulation.

Even though the diamond move combined with the flip move is ergodic in the ensemble of triangulations of all volumes, this does not necessarily mean this relocation move combined with the flip move is ergodic in the ensemble of all triangulations with fixed volume. It may be possible that other moves performed in the Markov chain in-between the diamond move and its inverse can reach a larger set of triangulations than the relocation move can. So, we will have to prove its ergodicity to make sure it forms a valid move set together with the flip move. A proof for this will be presented in the next section; for now we will assume it is valid and proceed to discuss its implementation and acceptance probability.

We can select a diamond and shard in the same way as we did for the diamond move, with or without a list of diamonds in the triangulation. Note, that if the selected diamond and shard overlap the relocation move does not make sense, and we will define the move to keep the triangulation unchanged to keep the proposal probabilities simple[16]. In this case the total volume N_2 remains fixed, hence $\mathcal{P}(T) = \mathcal{P}(T')$. Moreover, the proposal probability $S(T \to T') = 2/N_2 \cdot 2/N_2$ without a list of diamonds, or $S(T \to T') = 1/n_d \cdot 2/N_2$ with a list of diamonds. This is identical to the proposal probability of the inverse, as we have that $n_d(T) = n_d(T')$. Thus, we see that both selection procedures already give a proposal probability that satisfies detailed balance, so no additional rejection is required. One can again decide which of the selection methods to use based on the implementation of the move and diamond list. Our implementation uses the second selection method, keeping an additional list of the diamonds in the triangulations, as we have very efficient implementations for the operations necessary on this list (see appendix A).

For our numerical model we choose to use the combination of the relocation move and the flip move to simulate all the 2D CDT triangulations on which the all presented measurements are taken. Finally, we note that one can choose the relative selection probabilities of the flip move with respect to the relocation move, which is most effectively chosen to minimize the correlation time of the Monte Carlo simulation. We tested different ratios of the selection probabilities and found it had little to no impact on the correlation time for ratios between 0.3 and 0.7. Outside this range a negative impact was observed, so we have chosen to use a ratio of 0.5, selecting the flip move and relocation move equally often.

---

[15] Thanks to Timothy Budd for suggesting this move.

[16] In our implementation where we only store the triangle connectivity by label, we select a diamond by either its right triangles and the shard by either of its triangles. Then we first remove the right shard of the diamond and second add a shard to the right of the selected shard. This only fails when the selected shard is the same as the right shard of the selected diamond, in which case we simply do not change the triangulation.

3.5 Ergodicity proof

As explained in the previous section, we use Markov chain Monte Carlo to sample triangulations with a fixed volume N_2 using a combination of the *flip move* and *relocation move*. To make sure this move set is able to sample the full ensemble of fixed-volume triangulations, we will show it is ergodic in this ensemble. For definiteness, we will consider only triangulations with toroidal topology. So the spatial slices $T_1(t)$ are circles of vertices and $T_1(t+\tau) = T_1(t)$, where τ denotes the number of spatial slices. Recall that each spatial slice $T_1(t)$ has length denoted by l_t. Note that for a toroidal topology without boundaries the number of triangles N_2 is necessarily even.

First we show that the flip move is ergodic the ensemble of all triangulations that have a given length distribution $\{l_1, l_2, \cdots, l_\tau\}$ of the spatial slices. Consider a single slab, the triangles between two spatial slices $T_1(1)$ of length l_1 and $T_1(2)$ of length l_2, which we denote with $(T_1(1), T_2(2))$. The slab contains l_1 future-pointing triangles and l_2 past-pointing triangles. Let us encode the slab as a periodic sequence of future-pointing triangles (which we will denote with a 0) and past-pointing triangles (which we will denote with a 1). For example 01110100011 encodes the slab displayed in Fig. 3.5. Note that the sequence is periodic so 01110100011, 11101000110, 11010001101, 10100011011, etc. are equivalent. We only consider triangulations obeying the simplicial manifold condition, so there will be at least three 0's and three 1's in each sequence. In this encoding the flip move entails swapping an adjacent 0 and 1, i.e. $01 \to 10$ or $10 \to 01$.

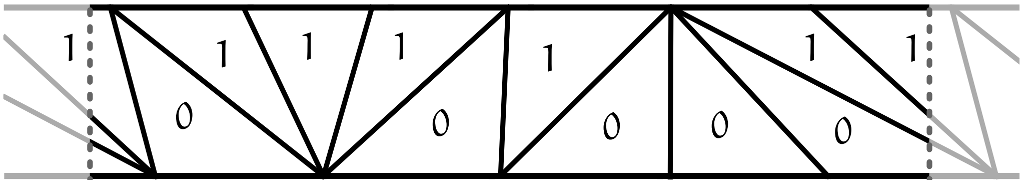

Figure 3.5: An example triangulation slab. Note that the slab is periodic: the first '1' is the same as the last '1'. The slab has been visualized with a region that is slightly larger than the period of the slab, such that one can see overlap.

To encode how the slabs are glued together to form the full triangulation we mark one 0 (future-pointing triangle) and one 1 (past-pointing triangle) in each slab. And we glue each marked future-pointing triangle 0 in a slab $(T_1(t), T_1(t+1))$ to each marked past-pointing triangle 1 in the next slab $(T_1(t+1), T_1(t+2))$. This uniquely defines the gluing, as the rest of the triangles can only be glued together in a single way. For example, the gluing of slab $(T_1(1), T_1(2))$ given by $\underline{0}11\underline{1}0100011$ and $(T_1(2), T_1(3))$ given by $01\underline{1}011\underline{0}00011$ is shown in Fig. 3.6. Using the marked encoding for each slab, we uniquely encode any triangulation in the ensemble with a fixed spatial slice length distribution.

To show that we can go from any triangulation to any other triangulation using a finite number of flip moves, it is enough to show that we can go from a single marked slab to any other marked slab. This is because the flip move does not affect triangles in other slabs, and the two marked triangles makes sure all possible gluings are considered. To see that we can reach any marked sequence encoding a slab from any other marked sequence, consider the *standard marked sequence*. The standard marked sequence is given by l_1 0's followed by l_2 1's, where the leftmost 0 and the

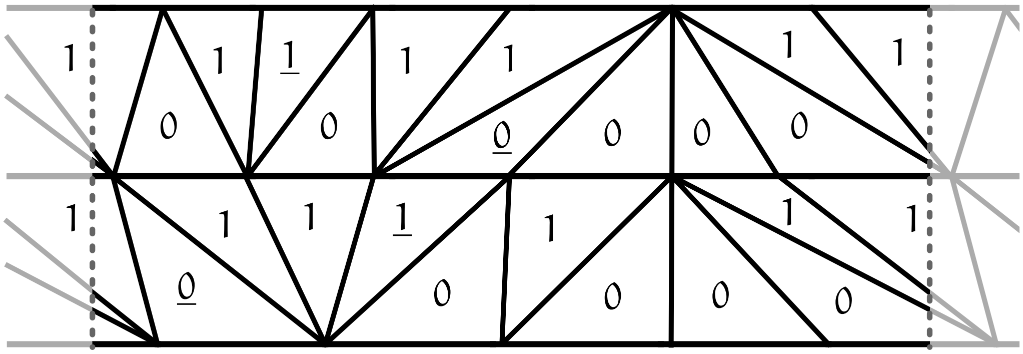

Figure 3.6: An example of two slabs glued together, by gluing the marked $\underline{1}$ future-pointing triangle of the bottom slab to the marked $\underline{0}$ past-pointing triangle of the top slab. Note that the slabs are periodic.

leftmost 1 are marked,

$$\overbrace{\underline{0}0\ldots0}^{l_1}\overbrace{\underline{1}1\ldots1}^{l_2}.$$

We can go from any marked sequence to the standard marked sequence by repeatedly applying the flip moves, which in this encoding are given by $01 \to 10$ or $10 \to 01$. To do so, we first perform the $10 \to 01$ move as many times as possible using only unmarked 0's. This will result in a sequence where the leftmost 0 is marked. An example of this process is

$$00\underline{0}01\underline{1} \to 0\underline{0}010\underline{1} \to 0\underline{0}001\underline{1} \to \underline{0}0010\underline{1} \to \underline{0}0001\underline{1}.$$

Next, we perform the $01 \to 10$ move as many times as possible using only unmarked 1's. This will result in a sequence in the standard marked form. Continuing the example for this process gives

$$\underline{0}0001\underline{1} \to \underline{0}0010\underline{1} \to \underline{0}0100\underline{1} \to \underline{0}1000\underline{1} \to \underline{0}000\underline{1}1.$$

We can get from any sequence to the standard marked sequence by a finite number of flip moves. We can then perform this procedure in reverse to get from the standard marked sequence to any other marked sequence. Using this procedure and thereafter a reverse procedure we can get from any marked sequence to any other. This shows that the flip move is ergodic in the ensemble with a fixed length distribution of spatial slices $\{l_1, l_2, \cdots, l_\tau\}$ using a finite number of flip moves.

To be ergodic in the ensemble of triangulations with a fixed volume, we need to also allow the relocation move. Using the relocation move, it is possible to move a vertex from a spatial slice $T_1(i)$ to another timeslice $T_1(j)$. Given a length distribution of the spatial slices $\{l_1, \cdots, l_i, \cdots, l_j, \cdots, l_\tau\}$ the relocation move from slice $T_1(i)$ to $T_1(j)$ gives a distribution $\{l_1, \cdots, l_i - 1, \cdots, l_j + 1, \cdots, l_\tau\}$. Repeated application of the relocation move can yield any length distribution of spatial slices with fixed total volume $N_0 = \sum_t l_t$. However, performing the relocation move is only possible if the vertex that is moved has vertex order four. Fortunately, we know we can get each slab to the standard marked form using the flip moves. And in the standard marked form each spatial slice $T_1(t)$ has $l_t - 1$ vertices with degree 4, meaning we have at least 2. So indeed using the flip move it is always possible to make sure each spatial slice has a vertex with degree four, such that the relocation move can be performed between any spatial slices.

This concludes the proof showing that it is possible to go from any triangulation with fixed volume N_2 to any other triangulation with volume N_2, using the flip and relocation moves. Thus, the Markov chain Monte Carlo move set consisting of the flip and relocation moves are ergodic in the ensemble triangulations with fixed volume.

4. Model Verification

In order to verify the validity of the numerical model and get an idea of the possibilities and limitations of the model, we will measure the vertex degree distribution, which is known analytically. Additionally, we measure some standard observables, namely the Hausdorff dimension and the spectral dimension.

Besides verifying the numerically obtained observables with their analytical predictions, they also serve as a useful tool in analysing the equilibration as well as the correlation of the numerical measurements.

4.1 Vertex degree distribution

One of the simplest properties of a triangulation is the degree distribution of the vertex graph. With *vertex degree* we mean the number of edges connected to the vertex or equivalently[1] the number of directly neighbouring vertices.

4.1.1 Theoretical distribution

The expected distribution can be derived by realizing that for a CDT triangulation with infinite volume N_2, the number of future $k_{(f)}$ and past $k_{(p)}$ time-like links from a vertex are completely independent of the number of links of other vertices [12]. Now, consider only the future time-like links; each of these links adds a triangle contributing a weight factor of $e^{-\lambda}$ to the partition function. So k future time-like links give a weight factor of $e^{-k\lambda}$. Hence, the probability of a vertex having k future-directed links is proportional to $e^{-k\lambda}$, giving the (normalized) probability distribution

$$p_\lambda[k] = \left(e^{\lambda} - 1\right) e^{-k\lambda} \qquad \text{for } k \geqslant 1. \tag{4.1}$$

By symmetry the probability distribution of the past-directed links is identical to (4.1). With the addition of the fixed two space-like links of every vertex and remembering that there is a minimum of one future and one past time-like link, one obtains

$$\begin{aligned} p_\lambda[c] &= \sum_{k=1}^{j-3} p_\lambda[k]\, p_\lambda[c-2-k] \\ &= (e^{\lambda}-1)^2 \sum_{k=1}^{c-3} e^{(2-c)\lambda} \\ &= (c-3)(e^{\lambda}-1)^2\, e^{(2-c)\lambda}. \end{aligned} \tag{4.2}$$

In the thermodynamic limit, where $\lambda \to \lambda_c = \ln 2$, we obtain that the distribution of the vertex degree c is given by

$$p[c] = \frac{c-3}{2^{c-2}} \qquad \text{for } c \geqslant 4 \tag{4.3}$$

which is properly normalized.

---

[1] This is only true because we are working with triangulations that obey the simplicial manifold condition.

4.1.2 Numerical distribution

The distribution of vertex degrees is easily measured in the numerical model by counting the number of neighbouring vertices of each vertex. We can measure the ensemble average of the distribution of vertex degrees and compare it to the expected distribution (4.3). The results are shown in Fig. 4.1, and estimate the ensemble average using 50 configurations. From the figure it is clear that the numerical model correctly reproduces the expected vertex distribution, and is thus consistent with the theoretical model in this respect. Also note that the difference in distribution between different configurations in the ensemble is negligible, as can be seen from the small[2] standard deviation between the different configurations as displayed in Fig. 4.1.

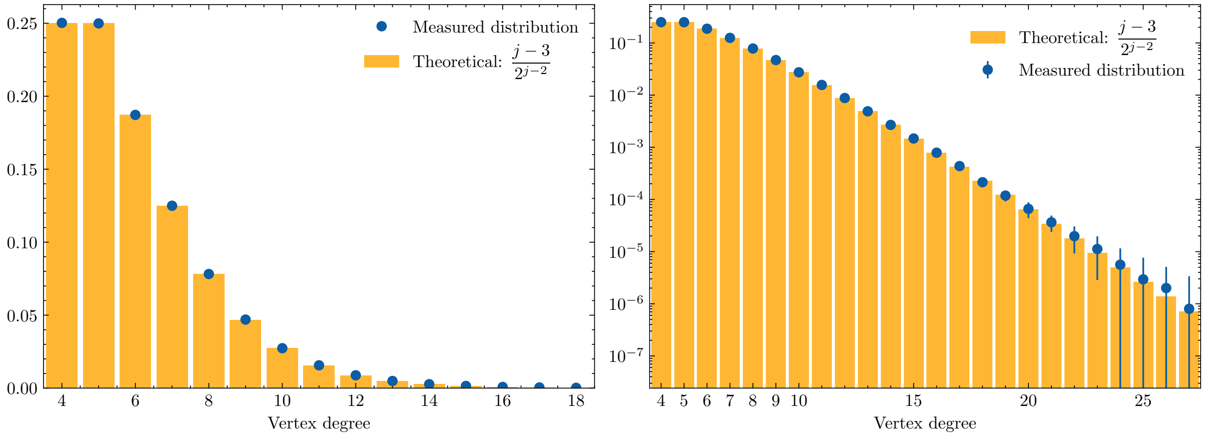

Figure 4.1: Measured vertex degree distribution compared to the theoretical distribution (4.3). On the right a logarithmic scale is used to better compare higher vertex degree frequencies; this plot also shows the standard deviation of the vertex degree distribution over different configurations.

4.2 Hausdorff dimension

One of the standard results of 2D causal dynamical triangulation is the intrinsic Hausdorff dimension of $d_H = 2$, which is equal to the topological dimension. This result is in contrast to EDT where a Hausdorff dimension of $d_H = 4$ is found [1]. Whilst it may seem a trivial result to obtain a dimension of 2 for a 2D model, this is not the case. The topological dimension of the triangulations does in general not determine the dimension of the continuum limit of dynamical triangulations. This is for example the case for 2D EDT, which have a fractal geometry in the continuum limit. In these cases what we do is determine scaling dimensions like the Hausdorff dimension.

The idea of the Hausdorff dimension is motivated by the following observation. Consider a (geodesic) sphere in a d-dimensional Riemannian manifold (M, g), by which we mean the submanifold $S_x(r) := \{y \in M \mid d_g(x, y) = r\}$, where $d_g(x, y)$ is the shortest geodesic distance between x and y. Its volume is given by $\mathrm{Vol}\, S_x(r) = \int_{S_x(r)} d^d y \sqrt{h(y)}$ where h denotes the determinant of the induced metric $h_{\mu\nu}$ on the sphere. Then for a smooth Riemannian manifold the volume of the sphere scales with its radius r like

$$\mathrm{Vol}\, S_x(r) \propto r^{d-1}\Big(1 + \mathcal{O}\big(r^2\big)\Big),$$

---

[2] A non-negligible standard deviation can be seen for the larger vertex degrees in the logarithmic plot on the right of Fig. 4.1. This is caused by statistical errors, since the higher vertex degrees are very rare and the limited measurements performed for this test are not enough to obtain reliable statistics for those vertex degrees.

where the higher-order terms are curvature corrections depending on the Riemann tensor and its covariant derivatives. We can extract the dimension from the ball volume, using

$$\lim_{r\to 0} \frac{d\log(\mathrm{Vol}\, S(r))}{d\log r} = d - 1,$$

where the dependence on the origin point x vanishes in the limit $r \to 0$. For the continuum limit of CDT we would like to use this relation to define the *local* Hausdorff dimension, similar to analysis in [14] at a given point x to be

$$d_H(x) = 1 + \lim_{r\to 0} \frac{d\log(\mathrm{Vol}\, S_x(r))}{d\log r}, \tag{4.4}$$

where for a quantum geometry this local Hausdorff dimension does in general depend on the origin point x. So, we define the overall local Hausdorff dimension of the quantum geometry to be

$$d_H = 1 + \lim_{r\to 0} \frac{d\log\left(\left\langle \overline{\mathrm{Vol}\, S(r)} \right\rangle_V\right)}{d\log r}, \tag{4.5}$$

where $\left\langle \overline{\mathrm{Vol}\, S(r)} \right\rangle_V$ denotes the fixed-volume ensemble average of the manifold average $\overline{\mathrm{Vol}\, S(r)}$ of the sphere volume.

We discretize this definition by measuring distance and volume on the vertex graph of the triangulation, using link distance as geodesic distance. For (unlabelled) triangulations with fixed finite two-volume $N_2 = N$ we get that

$$\left\langle \overline{\mathrm{Vol}\, S(r)} \right\rangle_N = \frac{1}{Z_N} \sum_{T\in\mathcal{T}_N} \frac{1}{N_0} \sum_{p\in T} \mathrm{Vol}\, S_p(r), \tag{4.6}$$

where $\mathcal{T}_N$ denotes the fixed-volume ensemble (see section 3.2) with partition function Z_N, and N_0 the number of vertices. Also, r is now discrete and denotes the link distance, and $\mathrm{Vol}\, S_p(r) = \sum_q 1\ \delta_{d(p,q),r}$. In the discrete setting we can no longer take the limit $r \to 0$ for discrete r. Instead[3], we *fit* a two-parameter (c, d_H) power law

$$\left\langle \overline{\mathrm{Vol}\, S(r)} \right\rangle = c r^{d_H - 1}, \tag{4.7}$$

for an appropriate region of r to extract the Hausdorff dimension d_H. The measured sphere volumes at different volumes N_2 are presented in Fig. 4.2, which are based on 100 triangulations with 50 origin point p samples on each of them. For small r the sphere volume is subject to discretization artefacts which we want to exclude, so we choose to only fit to $r \geqslant 5$. Moreover, for large r one can see in Fig. 4.2 that the sphere volume starts to deviate from power law like behaviour. This is due to finite-size effect where the spheres are large enough that they wrap around the triangulation and overlap with themselves. This effect appears later for larger N_2 as the spheres need to be larger before they start wrapping around. We choose the upper bound of our fitting region at least before finite-size effects start to appear. It is not trivial to determine at what r this happens, and we will discuss this in more detail in chapter 6. For now, it suffices to know we have a method to determine a maximum r for which finite-size effects are negligible, which we use as the upper bound of our fitting region. Finally, we introduce a shift to r in the fitting $r \mapsto r - r_0$, to improve the fit quality as is commonly done [15, 16], which is the same for different N_2. For our measurements we found the best shift to be $r_0 = 0.63$. With this fitting

---

[3] We have also analysed the logarithmic derivative (4.5) directly using finite differences as a function of r. This yields the same estimate for d_H but gives rise to some different considerations which are presented in appendix B.2.

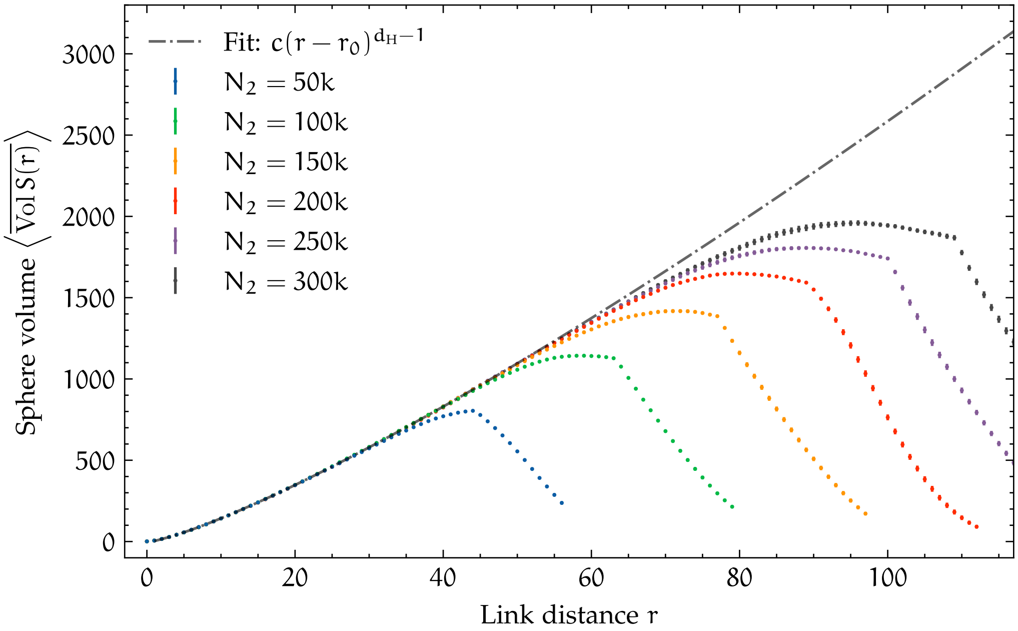

Figure 4.2: Estimated average of sphere volume $\left\langle \overline{\mathrm{Vol}\, S(r)} \right\rangle$ in 2D CDT at several two-volumes N_2 with $\daleth = 0.32$. This includes a power law fit to the sphere volume at the largest volume $N_2 = 300k$ to extract the Hausdorff dimension.

procedure we are able to estimate the local Hausdorff dimension at increasing volumes N_2; an example of such a fit is also displayed in Fig. 4.2. The obtained estimates of d_H are displayed as a function of volume N_2 in Fig. 4.3. From this figure we can see that in this volume range there appears to be no significant difference in the d_H estimates for different N_2. This leads us to conclude that the measured local Hausdorff dimension of 2D CDT is $d_H = 2.23 \pm 0.01$ for $\daleth = \tau^2/N_2 = 0.32$[4].

This result deviates from the theoretically expected $d_H = 2$ [1]. Other numerical estimates that have been previously obtained are $d_H = 2.2 \pm 0.2$ [17] and $d_H = 2.03 \pm 0.04$ [12]. Our result is consistent with the first source, but not with the second, while both of these are consistent with the theoretically expected value. However, both these results are obtained using a different method than the one we use, namely using finite-size scaling of the sphere volume profile. For this method the full sphere volume profile is considered, not just small r. This gives a global Hausdorff dimension, which need not be the same as our local Hausdorff dimension, but previous results [12, 14] find they are the same for 2D CDT. Note that using finite-size scaling in CDT is more difficult than in Euclidean Dynamical Triangulation (EDT) where the Hausdorff dimension has been consistently measured using finite scaling to great precision [15]. For EDT finite-size scaling can be performed with respect to a single scale N_2, giving a scaling limit where the sphere volume profiles collapse to a known limiting curve for all r. This is more challenging in CDT, where we have the additional scale of time extension. The most natural treatment is to keep the ratio $\daleth = \frac{\tau^2}{N_0}$ [14] fixed, although it is not stated in [17] and [12] what choice is made here. Moreover, we find that the collapse is not nearly as good for CDT as is the case in EDT, as was also seen by [17]. For our analysis we use only a small range of r to base our estimate on. A problem our result may still have is that the range we use is already subject to significant curvature corrections, giving a deviation from power law behaviour, as our range continues up until finite-size effects start to appear. However, experimenting with a smaller upper bound on the radius r range yielded no significant difference; only decreasing the error due to having less points to fit to.

---

[4] Investigation at other $\daleth$ up to $\daleth = 4$ seems to give no significant difference.

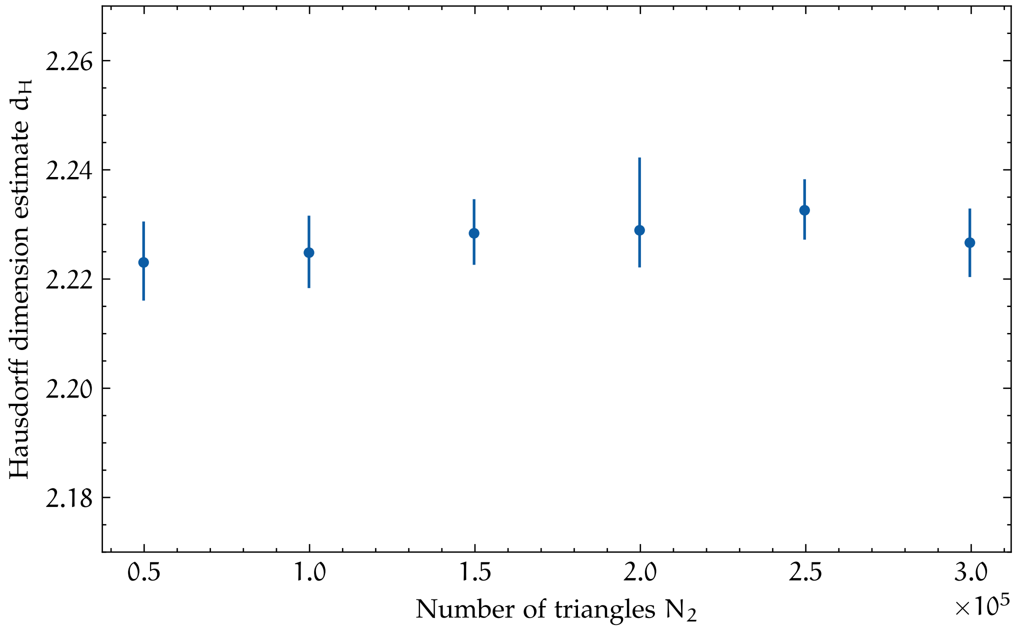

Figure 4.3: Estimates of the Hausdorff dimension d_H based on a power law fit (4.7) of the sphere volume in 2D CDT at several volumes N_2 with $\daleth = 0.32$. The displayed error bars are 95% confidence intervals based on bootstrap resampling of the sampled triangulations.

In conclusion, it seems that for CDT sphere volume profiles are not well suited to extract the Hausdorff dimension, at least for the volumes considered here. It may be better to extract the Hausdorff dimension using other methods, like looking at the scaling of the length distribution of the spatial slices [12, 14]. However, since investigating the Hausdorff dimension is not the focus of this study we will not spend more time on this investigation.

4.3 Spectral dimension

Another notion of dimension is the *spectral dimension*, which is a scaling dimension of a diffusion process,

$$\frac{\partial \rho(x, x_0; \sigma)}{\partial \sigma} = \eta \, \nabla^2 \rho(x, x_0; \sigma), \tag{4.8}$$

where $\rho(x, x_0; \sigma)$ is the probability density of diffusion from x_0 to x in diffusion time $\sigma \in \mathbb{R}$, ∇^2 the Laplace operator on a d-dimensional Riemannian manifold (M, g), and $\eta > 0$ a diffusion constant. From $\rho(x, x_0; \sigma)$ we can construct the return probability P on manifold M as the manifold average

$$P(\sigma) = \frac{1}{\operatorname{Vol} M} \int d^d x \, \sqrt{g(x)} \, \rho(x, x; \sigma), \tag{4.9}$$

with metric determinant g. Then the return probability $P(\sigma)$ has the expansion [18]

$$P(\sigma) = \frac{1}{(4\pi\eta\sigma)^{d/2}} \big(1 + \mathcal{O}(\sigma)\big)$$

So we are able to extract the dimension from the return probability with

$$\lim_{\sigma \to 0} -2 \frac{d \log P(\sigma)}{d \log \sigma} = d.$$

Using this relation, we define the *spectral dimension* of dynamical triangulations at constant two-volume $N_2 = N$ to be

$$d_s(\sigma) = \left\langle -2\frac{d \log P_T(\sigma)}{d \log \sigma} \right\rangle_N, \tag{4.10}$$

where now $\sigma \in \mathbb{Z}$ is discrete, $P_T(\sigma)$ is the return probability on the triangulation T, and the derivative is realized using finite differences. Since σ is discrete we cannot simply take the limit $\sigma \to 0$, so instead we measure $d_s(\sigma)$ up to large σ and determine a region of small σ where curvature corrections are still negligible to approximate the limit.

To measure the return probability on a triangulation T, we will perform a diffusion process (4.8) with a discrete probability field $\rho_T(i, i_0; \sigma)$, which represents the probability of diffusing from *triangle*[5] i_0 to i in σ diffusion steps. The diffusion process is implemented using the evolution rule

$$\rho_T(i, i_0; \sigma + 1) = (1 - \eta)\, \rho_T(i, i_0; \sigma) + \frac{\eta}{3} \sum_{k \to i} \rho_T(k, i_0; \sigma), \tag{4.11}$$

where $k \to i$ signifies the set of all *triangles* neighbouring i, and $\eta \in (0, 1]$ takes the role of the diffusion constant. We initialize the diffusion process by setting $\rho_T(i, i_0; 0) = \delta_{i,i_0}$. An example of the first steps of such a diffusion process on the triangles of a triangulation is illustrated in Fig. 4.4. One can check that using this evolution rule ρ_T will remain properly normalized, $\sum_i \rho(i, i_0; \sigma) = 1$. The return probability is then calculated with the triangulation average

$$P_T(\sigma) = \frac{1}{N_2(T)} \sum_i \rho_T(i, i; \sigma), \tag{4.12}$$

where $N_2(T)$ again denotes the number of triangles in the triangulation. The diffusion constant η can be freely chosen within its range $(0, 1]$, as it only rescales the dimensionless σ. If $\eta = 1$, the small-σ behaviour of $P_T(\sigma)$ is very different for odd and even σ, due to the discretized nature of the set-up; this effect can be seen in the example in Fig. 4.4. To alleviate this strong dependence it can help to choose $\eta < 1$, as this smoothes out this even-odd effect; a value around $\eta = 0.8$ is common [8, 19].

To measure the spectral dimension $d_s(\sigma)$ for 2D CDT, we estimate the ensemble average by taking a sample average over 1370 configurations. In each triangulation we only measured the return probability for a single origin triangle, instead of taking a triangulation average, i.e. we estimate $P_T(\sigma)$ by $\rho_T(i_0, i_0, \sigma)$ for some randomly sampled triangle i_0. We consider a single triangle sample to be sufficient for large enough N_2, because we expect that for a local quantity like the spectral dimension, taking the ensemble average over single triangle samples will be equivalent to an ensemble average over a manifold average. For the finite differences implementing the derivatives in (4.10) we have used second-order central differences. The results of this measurement are displayed in Fig. 4.5. The figure shows a region with discretization artefacts up to around $\sigma = 300$. These discretization artefacts are caused by the previously discussed even-odd effect, the discretization of the derivative, and the discretized nature of the triangulation. After the discretization region the $d_s(\sigma)$ estimate shows a plateau, which remains constant up to $\sigma = 2000$. This seems to indicate that in the diffusion step σ region that is shown there are no visible curvature effects. So to approximate the limit $\sigma \to 0$ in this discretized setting it appears sufficient to use any region in $\sigma \in [300, 2000]$, in which case we obtain that the spectral dimension of 2D CDT is measured to be: $d_s = 2.013 \pm 0.007$. This is within the 95% confidence interval of the expected theoretical value of $d_s = 2$ [20]. Moreover, it is compatible with the numerical result 2.02 ± 0.02 of [17]. Note that the measurement is only shown for a single N_2. Small measurement sets have been

---

[5] Note that this diffusion process is performed on the dual graph of triangulations, that is, the probability is associated with the triangles.

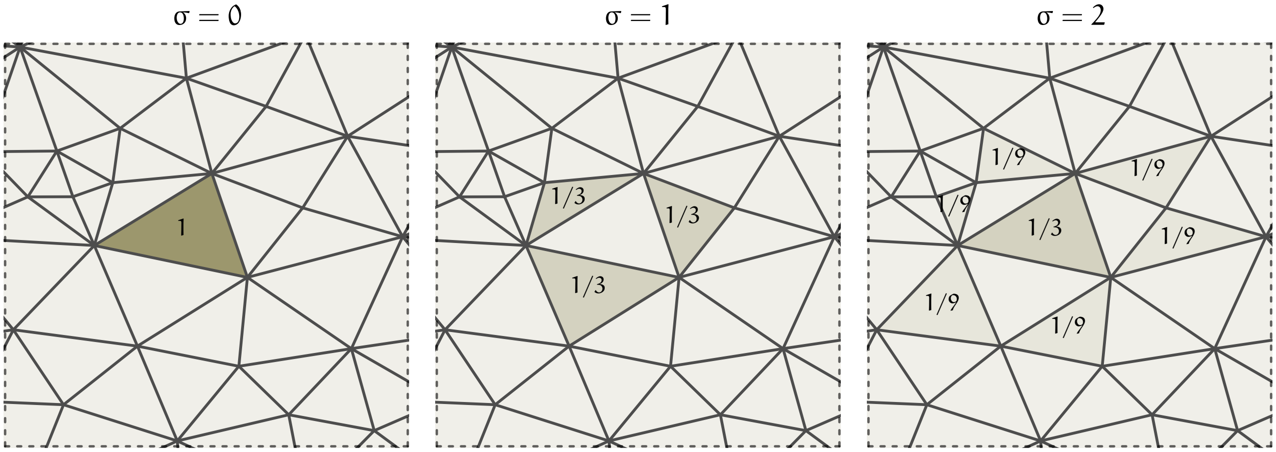

Figure 4.4: Example of the first three steps of a diffusion process on a triangulation with $\eta = 1$, where each triangle has its $\rho_T(i, i_0; \sigma)$ displayed (note that the $\rho_T = 0$ values are not shown). The return probabilities of the first few steps are $P_T(0) = 1, P_T(1) = 0, P_T(2) = 1/3, P_T(0) = 0, \ldots$, showing the odd-even effect by the vanishing return probability at odd σ. This can be understood for the triangulation in the figure by considering the paths that start at and return to triangle i_0 (the triangle with $\rho_T(\sigma = 0) = 1$). For short lengths, only paths with an even length can be constructed.

performed on smaller sizes ($N_2 = 100\text{k}, 200\text{k}$) that have no significant difference in the region up to $\sigma = 2000$, which seems to indicate that there are no significant finite-size effects for $N_2 = 300\text{k}$ up to this $\sigma = 2000$. However, to be certain that there are no finite-size effects significantly altering the estimated spectral dimension, more measurements should be performed at different volumes N_2. Since estimating the spectral dimension is not the focus of this research project, we will not investigate this further.

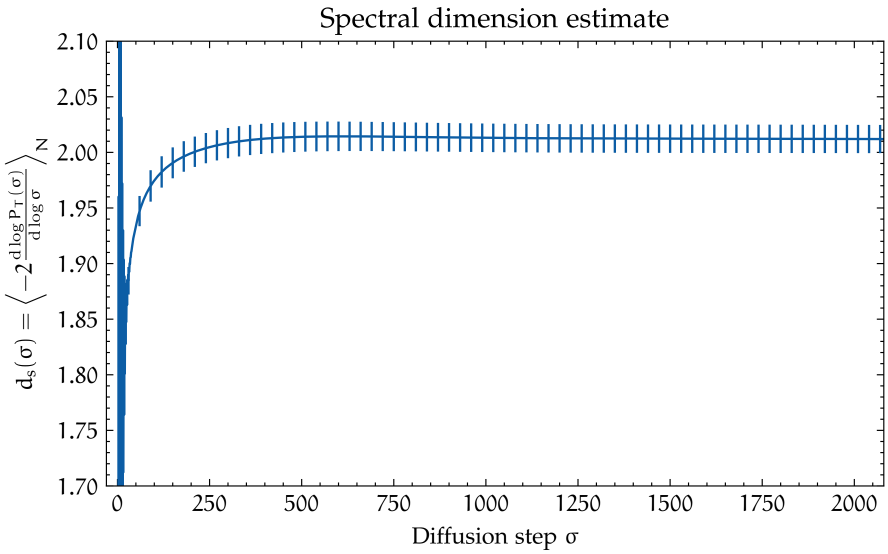

Figure 4.5: Spectral dimension estimate for 2D CDT at $N_2 = 300\text{k}$ and $\tau = 219$ using a diffusion process with $\eta = 0.9$. Only 1 in 30 error bars is shown to avoid clutter, and they display the 95% confidence interval.

5. Quantum Ricci Curvature

Measuring curvature in quantum gravity, where the geometries are non-smooth, is challenging; one cannot use normal Ricci curvature in terms of derivatives of the metric since no such smooth metric may exist. Klitgaard and Loll [2] defined an alternative *coarse-grained* construction of curvature, inspired by Ollivier [21], by comparing the distance of two nearby infinitesimal spheres with the distance of their centres. In a smooth Riemannian space this construction is shown to retrieve Ricci curvature, but crucially this construction can be defined in non-smooth metric spaces as it depends solely on geodesic distance. For this quantum Ricci curvature a notion of distance between spheres is necessary. In [2] the *average sphere distance* (ASD) between spheres[1] $S_x(\delta)$ and $S_{x'}(\delta)$, centred at x and x', is defined as

$$\bar{d}\big(S_x(\delta), S_{x'}(\delta)\big) := \frac{1}{\mathrm{Vol}\, S_x(\delta)} \frac{1}{\mathrm{Vol}\, S_{x'}(\delta)} \int_{S_x(\delta)} d^{n-1}y \sqrt{h(y)} \int_{S_{x'}(\delta)} d^{n-1}y' \sqrt{h'(y')}\, d_g(y, y'). \tag{5.1}$$

Here, $d_g(y, y')$ is the geodesic distance between y and y' with respect to metric g, and h and h' are the determinants of the induced metrics on the geodesic spheres[1] $S_x(\delta)$ and $S_{x'}(\delta)$ respectively. The volume of these spheres is given by the volume integral with respect to their induced metric.

We call the centre distance $\epsilon \equiv d(x, x')$, meaning we have two length scales δ and ϵ. Since this construction only relies on geodesic distance, it can be used in a more general setting than differentiable manifolds. Importantly, it can be applied to triangulations, meaning we can measure it numerically for our dynamical triangulations. For the case of a Riemannian manifold where the distances are sufficiently small, one finds that the point x' can be expressed uniquely using the exponential map from x, such that $x' = \exp_x(\epsilon v)$ where v is a unit vector in the tangent space of x. The relative positioning of x and x' therefore serves as the 'direction' or 'vector' of the average sphere distance. It is precisely this direction that reproduces the directional nature of the Ricci curvature in the limit of $\delta = \epsilon \to 0$. This construction is further illustrated by a two-dimensional example in Fig. 5.1, where one should imagine averaging the distance $d(y, y')$ over all possible combinations of y and y' on the spheres.

In practice, it is convenient to have a curvature prescription which only depends on a single length scale. As such it is convenient to fix the distances between the spheres to be $\epsilon = \delta$, such that the spheres intersect one another; this is the standard choice made in previous works on average sphere distance [2, 22]. For this choice of ϵ we will sometimes denote the average sphere distance by $\bar{d}_{xx'}(\delta)$ for convenience. For sufficiently small δ it is related to the Ricci curvature in a two-dimensional Riemannian manifold in the following way [13]:

$$\frac{\bar{d}\big(S_x(\delta), S_{x'}(\delta)\big)}{\delta} \approx 1.5746 - 0.0720\, R\, \delta^2 + O\big(\delta^3\big), \qquad \text{where } d_g(x, x') = \delta, \tag{5.2}$$

where R is the Ricci scalar[2]. An alternative is to set $\epsilon = 0$, such that the two spheres overlap, and we have the average distance of a single sphere to itself; in this case we will sometimes denote this $\bar{d}_x(\delta)$. However, doing this loses all directional information. This means that the average sphere distance for $\epsilon = 0$ can only retrieve scalar curvature, without direction. In this case we find (see section B.1 for a derivation) the average sphere distance to be related to Ricci curvature in a two-dimensional Riemannian manifold for sufficiently small δ according to

$$\frac{\bar{d}\big(S_x(\delta), S_x(\delta)\big)}{\delta} = \frac{4}{\pi} - \frac{R}{9\pi}\,\delta^2 + O\big(\delta^3\big) \approx 1.273 - 0.0354 R\, \delta^2 + O\big(\delta^3\big). \tag{5.3}$$

---

[1] A geodesic sphere with centre point x is the submanifold given by $S_x(r) = \{y \in M \mid d_g(x, y) = r\}$ together with the induced metric h.

[2] In two dimensions the Ricci scalar is algebraically equal to twice the Ricci curvature in the direction of v.

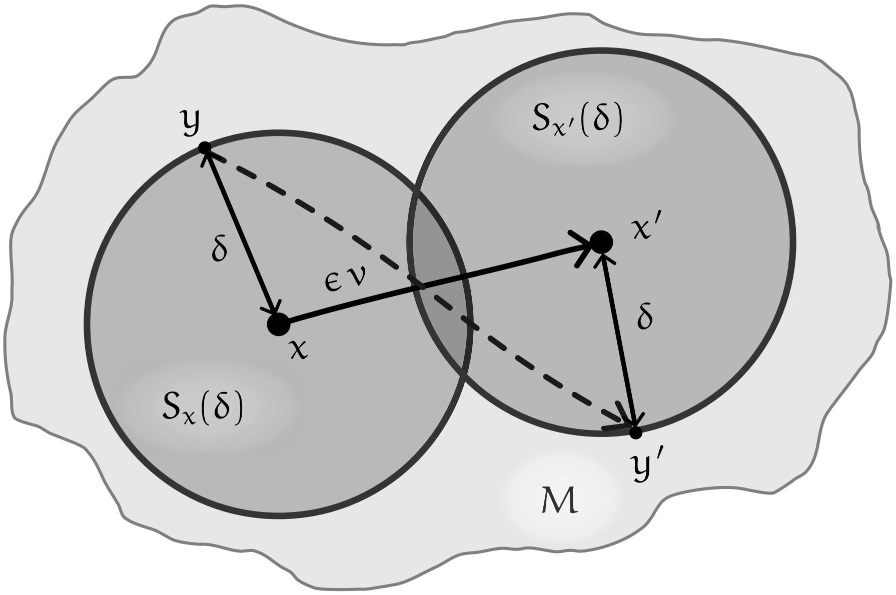

Figure 5.1: Diagram illustrating the construction of the average sphere distance on a manifold M for infinitesimal ϵ and δ. ϵ is the geodesic distance between x and x', and ν is the vector at x which points along the geodesic.

From (5.2) and (5.3) we can see that the largest difference between these two prescriptions can be seen as a rescaling of δ (of about 1.24). This makes sense as for the same δ the area covered by the spheres of the ASD with $\epsilon = \delta$ is larger than the area covered by the sphere of the ASD with $\epsilon = 0$. So for the same δ the average sphere distance is larger, and the effect of curvature is stronger with $\epsilon = \delta$. So if one wishes to extract the curvature from average sphere distance using $\epsilon = 0$, one may expect that one needs to measure up to slightly larger values of δ to see the same curvature effects as for $\epsilon = \delta$.

The relation of average sphere distance to Ricci curvature in continuum motivates to define the coarse-grained *QRC (quantum Ricci curvature)* as $K(x, x'; \delta)$ for $\epsilon = \delta$, such that

$$\frac{\bar{d}\big(S_x(\delta), S_{x'}(\delta)\big)}{\delta} := c_q\big(1 - K(x, x'; \delta)\big), \tag{5.4}$$

with prefactor $c_q := \lim_{\delta\to 0} \bar{d}/\delta$. For the case of $\epsilon = 0$, we only measure scalar curvature and have a quantum Ricci scalar $K(x; \delta)$, such that

$$\frac{\bar{d}\big(S_x(\delta), S_x(\delta)\big)}{\delta} := c'_q(1 - K(x; \delta)), \tag{5.5}$$

where c'_q is a prefactor defined equivalently to c_q. Note that in the continuum c_q and c'_q are constants that only depend on the dimension. However, in a discrete setting this constant also depends on the type of lattice – it is for example different for a hexagonal and a square lattice. In a dynamical triangulation situation where the lattice is not uniform, c_q and c'_q are in general not constant, and can have a point dependence.

We want to highlight the δ dependence of this prescription of curvature. For non-infinitesimal δ the quantum Ricci curvature measures curvature based on a non-infinitesimal area of a manifold. Because of this, the quantum Ricci curvature is called a 'coarse-grained' prescription of curvature. In a way it measures the average curvature of a region, smoothing out the details of that region. The coarse-grained nature of this prescription of curvature allows us to renormalize the quantum Ricci curvature of CDT in the continuum limit. This is something that we do not know how to do in 4D CDT for the Regge curvature [23], which is based on the deficit angle.

In quantum gravity, we are only able to measure diffeomorphism-invariant quantities as there is no way to identify a specific point in multiple configurations of the ensemble. So to measure average sphere distance in quantum gravity, we consider the manifold average of the average sphere distance. This gives an averaged measure of curvature associated with the scale δ in the manifold. In order to get a better idea of how the curvature changes throughout the manifold, we can also measure two-point correlations of the quantum Ricci curvature. However, to be able to do this we first need to define what two-point functions are in a quantum setting, which we will discuss in section 7. For now, we will consider the manifold average of the average sphere distance [24], which is called the curvature profile $\bar{d}_{\mathrm{av}}(\delta)$, for a manifold M with metric g,

$$\bar{d}_{\mathrm{av}}(\delta) := \frac{1}{G_g^{\mathbf{11}}(\delta)} \int_M d^n x \sqrt{g(x)} \int_M d^n x' \sqrt{g(x')}\, \bar{d}\big(S_x(\delta), S_{x'}(\delta)\big)\, \delta_D(d_g(x,x'),\delta), \tag{5.6}$$

for $\epsilon = \delta$ where $G_g^{\mathbf{11}}(\delta)$[3] is given by

$$G_g^{\mathbf{11}}(\delta) = \int_M d^n x \sqrt{g(x)} \int_M d^n x' \sqrt{g(x')}\, \delta_D(d_g(x,x'),\delta).$$

On a lattice this becomes the number of point pairs separated by distance δ. When we take a manifold average in this way, we also average over all directions between x and x'. So the directional information is lost in the average. If there is a distinguished direction in the quantum geometries one considers, it is also possible to average over point pairs that are only separated along this direction. This has been done for 2D CDT using the timelike and spacelike separation in [22], although the authors note that this time direction is not strictly well-defined. For the present work, we will only consider $\bar{d}_{\mathrm{av}}(\delta)$, the manifold average over all point pairs. This means we can only measure scalar curvature without directional information. Since we will not try to extract directional information, we can also use average sphere distance with $\epsilon = 0$. ASD $\bar{d}_x(\delta)$ itself has no directional information, so it does not need to be averaged over all directions, just over all points x in the manifold. For $\epsilon = 0$ the manifold-averaged ASD becomes

$$\bar{d}^0_{\mathrm{av}}(\delta) := \frac{1}{\operatorname{Vol} M} \int_M d^n x \sqrt{g(x)}\, \bar{d}\big(S_x(\delta), S_x(\delta)\big), \tag{5.7}$$

where $\operatorname{Vol} M = \int_M d^n x \sqrt{g(x)}$. We can define the (averaged) *quantum Ricci scalar* $K_{\mathrm{av}}(\delta)$, such that

$$\frac{\bar{d}_{\mathrm{av}}(\delta)}{\delta} =: c_{\mathrm{av}}\big(1 - K_{\mathrm{av}}(\delta)\big), \tag{5.8}$$

where $c_{\mathrm{av}} := \lim_{\delta\to 0} \bar{d}_{\mathrm{av}}/\delta$, and we define $K^0_{\mathrm{av}}(\delta)$ using $\bar{d}^0_{\mathrm{av}}(\delta)$ equivalently. Like we discussed for c_q and c'_q this c_{av} is known to be non-universal in the discrete setting, where it for example depends on the type of lattice [2, 13]. $K_{\mathrm{av}}(\delta)$ now takes the role of the Ricci scalar in quantum gravity setting.

5.1 Discretization

To be able to measure average sphere distance on dynamical triangulations we need to discretize the definitions for (manifold-averaged) average sphere distance. To discretize (5.1) we substitute the sphere integrals by sums over all vertices in the spheres[4] $S_p(\delta), S_{p'}(\delta)$, with the local volume elements equal to 1 in our discretization. The geodesic distance is given by the geodesic distance on the vertex graph $d(q, q')$, i.e. the link distance. In this discretization the sphere volume $\mathrm{Vol}\, S_p(\delta)$ is given by the number of elements in its set $S_p(\delta)$. The discretization of (5.1) becomes

---

[3] This is the same notation we use for two-point functions, which will become more clear in section 7.

[4] In the discrete case the spheres become a set of vertices (or triangles in the dual) $S_p(r) = \{q \in T \mid d_T(p,q) = r\}$.

$$\bar{d}\big(S_p(\delta), S_{p'}(\delta)\big) := \frac{1}{\mathrm{Vol}\, S_p(\delta)} \frac{1}{\mathrm{Vol}\, S_{p'}(\delta)} \sum_{q \in S_p(\delta)} \sum_{q' \in S_{p'}(\delta)} d(q, q'), \tag{5.9}$$

where δ now is a discrete distance.

To discretize the manifold averaging of (5.6) and (5.7) we substitute it with a sum over all vertices of the triangulation T with local volume elements 1, giving

$$\bar{d}_{\mathrm{av}}(\delta) := \frac{1}{G^{\mathbf{11}}_{T}(\delta)} \sum_{p \in T} \sum_{p' \in T} \bar{d}\big(S_p(\delta), S_{p'}(\delta)\big)\, \delta_{d(p,p'),\delta}\ , \tag{5.10}$$

$$\bar{d}^{0}_{\mathrm{av}}(\delta) := \frac{1}{\mathrm{Vol}\, T} \sum_{p \in T} \bar{d}\big(S_p(\delta), S_p(\delta)\big), \tag{5.11}$$

where $G^{\mathbf{11}}_{T}(r)$ is the number of point pairs of distance r,

$$G^{\mathbf{11}}_{T}(r) = \sum_{p \in T} \sum_{p' \in T} \delta_{d_T(p,p'),r},$$

and $\mathrm{Vol}\, T$ is the number of vertices in the triangulation.

Finally, in the quantum setting we are interested in the expectation value of the manifold-averaged ASD. For the fixed-volume ensemble $\mathcal{T}_N$ with $N_2(T) = N$, we get that the expectation value of the average *curvature profile* $\bar{d}_{\mathrm{av}}(\delta)/\delta$ is given by

$$\left\langle \frac{\bar{d}_{\mathrm{av}}(\delta)}{\delta} \right\rangle_N = \frac{1}{\delta\, Z_N} \sum_{T \in \mathcal{T}_N} \bar{d}_{\mathrm{av}}(\delta). \tag{5.12}$$

5.1.1 Analytical average sphere distance

For 2D CDT it is possible to analytically determine the average sphere distance for $\epsilon = 0$ and $\delta = 1$. This is because it only depends on the direct neighbours of the origin point, and none of the geodesic paths can go outside the $\delta = 1$ sphere, because of the simplicial manifold condition and the sliced structure[5] of the triangulations. The derivation is rather simple, so it is presented here. The average sphere distance at a vertex p on a triangulation at $\epsilon = 0$ and $\delta = 1$ can be expressed as a function of its vertex degree c,

$$\bar{d}_p(\delta = 1) = \frac{1 \cdot 0 + 2 \cdot 1 + (c - 3) \cdot 2}{c} = 2 - \frac{4}{c}.$$

We know the distribution of vertex degrees in a 2D CDT triangulation, namely (4.3), which allows us to compute the expectation value $\langle 1/c \rangle = \frac{17}{2} - 12 \ln 2$. So, we can determine the expectation value of the average sphere distance and find

$$\big\langle \bar{d}^{0}_{\mathrm{av}}(\delta = 1) \big\rangle = 16\big(3 \ln 2 - 2\big) \approx 1.271 \tag{5.13}$$

This result is not particularly useful as it only gives us the average sphere distance at $\delta = 1$, which does not allow us to determine the quantum Ricci curvature. However, it can serve as a good consistency check for numerical results, which is why it is presented here.

---

[5] For example in 2D Euclidean dynamical triangulation with no sliced structure the geodesic paths can go outside the $\delta = 1$ sphere.

5.2 Implementation

In order to numerically measure the average sphere distances we need to be able to measure distances on the vertex graph and construct geodesic spheres. This is most effectively done using a breadth-first search. To be able to determine the averaged ASD with $\epsilon = \delta$ we also need a method of finding all point pairs p, p' to average over them. However, averaging over all point pairs can be very computationally expensive, because there are many point pairs in a triangulation and computing the ASD between a single point pair is already quite expensive. Computationally it is therefore a lot more effective to take a sample point pairs and only average over those, instead of taking the average over the full triangulation. To be able to do this, we need a way to effectively sample point pairs. However, first we will turn our attention to measuring geodesic distance.

5.2.1 Breadth-first search

A breadth-first search (BFS) is a *graph* exploration algorithm that works by exploring outwards from a starting node first exploring all nodes at a given distance before moving on to nodes at a further distance, making it ideal to identify nodes at a given distance. The basis of the breadth-first search exploration algorithm is illustrated using pseudocode in Alg. 1. This algorithm crucially relies on the use of *queue*[6] or a first-in first-out data structure, which is ordered collection where elements are added on one side (enqueued) and removed (dequeued) on the other. Such a data structure can be implemented in several ways. The most effective implementation depends on size of the triangulation and the maximum required distance. For the implementation we used, see appendix A. Furthermore, to keep track of the distance of each node to the chosen initial node, one can store the distance along with the node in the *toExplore* queue or the *explored* list. Then, one can determine the distance of the *neighbour* node based on the distance of the *currentNode*. One can decide to break the exploration early when the desired distance has been reached. The BFS algorithm has a computation time complexity of $O(\hat{N}_0 + \hat{N}_1)$, where $\hat{N}_0$ and $\hat{N}_1$ are the number of vertices and edges region over which the breadth first search is performed. Note that in the 2D triangulations we are considering, the number of edges is proportional to the number of vertices. So in our case the time complexity is $O(\hat{N}_0)$.

Algorithm 1 A breadth-first search that will iterate through the entire graph in breadth-first fashion.

```
Require: An initial node, startNode, in the graph
Let explored be an empty list
  ADD(explored, startNode)
Let toExplore be an empty queue                         // A queue is a first-in first-out list
  ENQUEUE(toExplore, startNode)                         // Add node to end of the queue
repeat
    currentNode ← DEQUEUE(toExplore)                    // Remove node from the front of the queue
    neighbours ← GETNEIGHBOURS(currentNode)
    for all neighbour $\in$ neighbours and $\notin$ explored do
        ENQUEUE(toExplore, neighbour)                   // Add all new neighbours to queue
        ADD(explored, neighbour)                        // And mark new neighbours as visited
until toExplore is empty
```

---

[6] For a simple example see `deque`, an implementation in Python `https://docs.python.org/3/library/collections.html#collections.deque`. Or for an informal introduction to *queue*s see `https://www.geeksforgeeks.org/introduction-to-queue-data-structure-and-algorithm-tutorials/`.

Next we consider how to measure average sphere distance with $\epsilon = \delta$ for a given pair of δ-seperated points p, p'. First we need to construct the spheres $S_p(\delta)$ and $S_{p'}(\delta)$ by making use of two breadth-first searches up to distance δ, starting from p and p'. Then we need to determine the distances between all pairs of points in the spheres. This is done by performing a BFS from each of the nodes of one sphere up to 3δ, which is the maximal distance between a pair. Then, we average over all the distances at which the BFS finds the nodes of the other sphere. A simple and effective optimization [22] is to pick the smaller sphere to do the BFS from. This means we need to do a total of two BFSs up to δ, and $\min\big(\mathrm{Vol}\, S_p(\delta), \mathrm{Vol}\, S_{p'}(\delta)\big)$ BFSs up to 3δ. This gives an average time complexity of[7] $O\big(\overline{\mathrm{Vol}\, S(\delta)}\, \overline{\mathrm{Vol}\, \mathcal{B}(3\delta)}\big)$. We can estimate the average size of spheres and balls using the local Hausdorff dimension, as this is the scaling exponent of the volume of a ball. We obtain that the time complexity with respect to δ and d_H is given by $O\big(3^{d_H}\, \delta^{2d_H - 1}\big)$. For 2D CDT we find approximately $O\big(\delta^3\big)$ and for 2D EDT $O\big(\delta^7\big)$; the higher the power, the stronger the limit on the maximum δ we can feasibly reach for numerical measurements.

To measure average sphere distance with $\epsilon = 0$ for a given vertex p, we need to construct only a single sphere $S_p(\delta)$. For this case, one needs to determine the distances between all pairs of points on the sphere, for which one only needs a BFS to go up to 2δ. This means we need to do a total of one BFS up to δ and $\mathrm{Vol}\, S_p(\delta)$ BFSs up to 2δ. This gives an average time complexity of $O\big(\overline{\mathrm{Vol}\, S(\delta)}\, \overline{\mathrm{Vol}\, \mathcal{B}(2\delta)}\big)$ or $O\big(2^{d_H}\, \delta^{2d_H - 1}\big)$ in terms of δ. In this case, we have the same time complexity order in δ as for $\epsilon = \delta$, but the exploration need not go as far, making it faster for the same δ. However, as we discussed earlier, we likely need to go to higher δ to see the same curvature effects, because the area explored for the same δ is smaller.

5.2.2 Point sampling

To be able to determine the manifold-averaged ASD (5.11) for $\epsilon = 0$, we need to determine the average sphere distance at every vertex and average over all of them. While this is not difficult to do, it is very inefficient. The ASDs of neighbouring points are correlated (see section 8), so if we are interested in a manifold average, we can estimate it well by taking the average over a limited sample of points. This way we do not lose computation time by determining average sphere distances that bring little 'new' information. To do this, we can sample nodes uniformly and determine the sample average, estimating (5.11). Here, uniform sampling means that each vertex is selected with a probability proportional to its local volume element. In our discretization all vertices have local volume element 1, so each vertex is sampled with equal probability.

Similarly, we can determine the averaged ASD for $\epsilon = \delta$ (5.10) by only averaging over a sample of point pairs p, p'. To this end, we can use the following sampling as used by other authors [13, 22]:

1. Uniformly sample a *first point* p from T;
2. Identify the geodesic sphere $S_p(r)$;
3. Uniformly sample a *second point* p' from $S_p(r)$.

However, using this sampling the sample average estimates the following manifold-averaged ASD

$$\bar{d}_{\mathrm{av}}(\delta) := \frac{1}{\mathrm{Vol}\, T} \sum_{p \in T} \frac{1}{\mathrm{Vol}\, S_p(\delta)} \sum_{p' \in T} \bar{d}\big(S_p(\delta), S_{p'}(\delta)\big)\, \delta_{d_T(p,p'),\delta}, \tag{5.14}$$

not (5.10) as other authors [13, 22] take it to be[8]. Why this sampling gives this result is discussed in great detail in the section 7.1.4. To estimate the manifold-averaged ASD as given in (5.10), we can use another sampling. We construct a list of pairs of points at distance δ and uniformly sample a pair from that list. Here, *uniform* sampling means that each point pair is selected with a probability equal to the product of their local volume elements, which in our case is 1. In order to do this, a list of all point pairs needs to be constructed. This requires N_0 breadth-first searches up to the maximum δ that we want to measure. This can be done, and is in fact what we do for some measurements[9]. However, if only a smaller sample of the triangulation is required, performing a BFS for every vertex in the triangulation is rather inefficient. So, alternatively we can use a *weighted* sample average using the non-uniform sampling described previously,

---

[7] We use $\mathcal{B}$ to denote a geodesic ball.

[8] Note that is not per se wrong of these authors to use this sampling. They are just estimating a different discrete triangulation average of ASD than they state, but (5.14) is in principle a valid alternative definition of taking the triangulation average.

$$\bar{d}_{\mathrm{av}}(\delta) = \frac{\mathbb{E}\left[\mathrm{Vol}\, S_p(\delta)\, \bar{d}\left(S_p(\delta), S_{p'}(\delta)\right)\right]}{\mathbb{E}\left[\mathrm{Vol}\, S_p(r)\right]}, \quad \text{where } \epsilon = \delta, \tag{5.15}$$

where $\mathbb{E}$ represents the statistical expectation value of a sample using the non-uniform sampling. This estimates (5.10) as desired, and it has no additional computational cost as $\mathrm{Vol}\, S_p(r)$ is already computed for the ASD computation. Again this result is explained in detail in section 7.1.4.

5.3 Results

By using the sampling methods discussed in the previous sections we are able to estimate the ensemble average of the manifold-averaged average sphere distance (5.12) on 2D CDT triangulations generated by the previously described Monte Carlo methods. For the ASD with $\epsilon = \delta$ we obtain the results presented in Fig. 5.2, where both the non-uniform sampling (5.14) and uniform sampling (5.10) are used. The first points (for $\delta < 5$) are understood to be lattice artefacts, due to

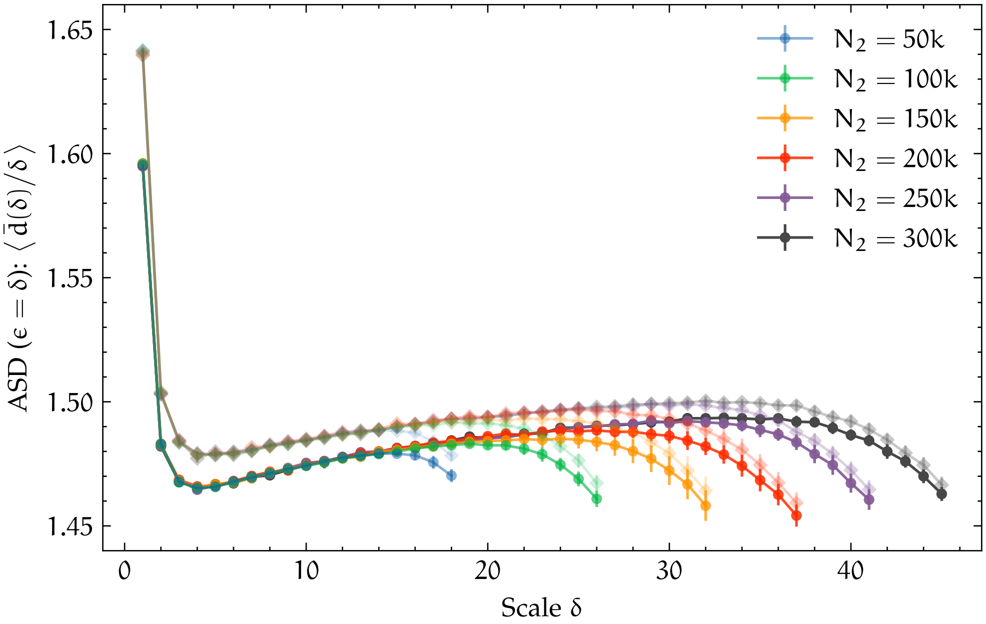

Figure 5.2: Ensemble average of the curvature profile or normalized average sphere distance $\langle \bar{d}_{\mathrm{av}}(\delta)/\delta \rangle_{N_2}$ (with $\epsilon = \delta$) for different system sizes at $\daleth = 0.32$. The higher-saturated colours with round markers are the ASD estimates using the non-uniform sampling (5.14). The lower-saturated colours with diamond markers are the ASD estimates using uniform sampling (5.10). In both cases 5k point pairs are used to estimate the triangulation average, and the ensemble average is estimated using a sample of 50 configurations.

---

[9] In this case we store the found distances in a distance matrix. This allows the distance measurements to be reused for many distance-related quantities, which is discussed in section B.3.

the specific discretization of the geometry and are irrelevant in the continuum limit. The last few points of each plot are understood to be finite-size effects, due to wrapping effects of the geodesics around the triangulation as will be discussed in chapter 6. From this figure it can be seen that the largest difference between the samplings is a vertical shift. A different vertical shift corresponds to a different c_{av} as given in (5.8). As discussed earlier, this prefactor c_{av} is not universal and its specific value is not important for the curvature interpretation. Additionally, the difference slightly decreases with increasing δ, meaning that the slope is smaller for (5.14) than for (5.10).

These results can serve as a good consistency check, as average sphere distance has been measured before in 2D CDT. Our results, using the non-uniform sampling (5.14), are identical to those of Brunekreef and Loll [22] for small enough δ. This suggests that our implementation is consistent with the implementation of these authors. Note that for larger δ where finite-size effects start to play a role, the results start to differ. This is to be expected, because different sizes and $\daleth$ have been used, giving rise to different finite-size effects.

The average sphere distance profile is not constant (for $\delta \geqslant 5$) as one might expect, but instead curves upwards indicating a negative quantum Ricci scalar. This result is discussed in the previously mentioned work [22], and we will not discuss it any further in this thesis.

Additionally, we present the results of the average sphere distance for $\epsilon = 0$ in Fig. 5.3. From this figure we can see that the curvature profile is qualitatively very similar to the profile with $\epsilon = \delta$. The jump between the initial points from $\delta = 1$ to $\delta = 2$ appears to be considerably smaller compared to the $\epsilon = \delta$ case (note the difference in the scale on the y-axis). In addition, the entire curvature profile is shifted downwards, starting at $\bar{d}^0_{av}(\delta = 1) \approx 1.27$ instead of $\bar{d}_{av}(\delta = 1) \approx 1.60$. This is consistent with the expectation from the local continuum expansion on a Riemannian manifold, where the additive constant is larger for $\epsilon = \delta$ than for $\epsilon = 0$. In fact, these additive constants are reasonably close to the $\delta = 1$ point of our results. Finally, we know from (5.13) what the average sphere distance of the first point $\delta = 1$ should be, namely $\bar{d}^0_{av}(\delta = 1) \approx 1.271$. Our results give $\bar{d}^0_{av}(\delta = 1) = 1.271 \pm 0.004$, which is perfectly consistent with the analytical expectation, providing another consistency check for the validity of our numerical setup.

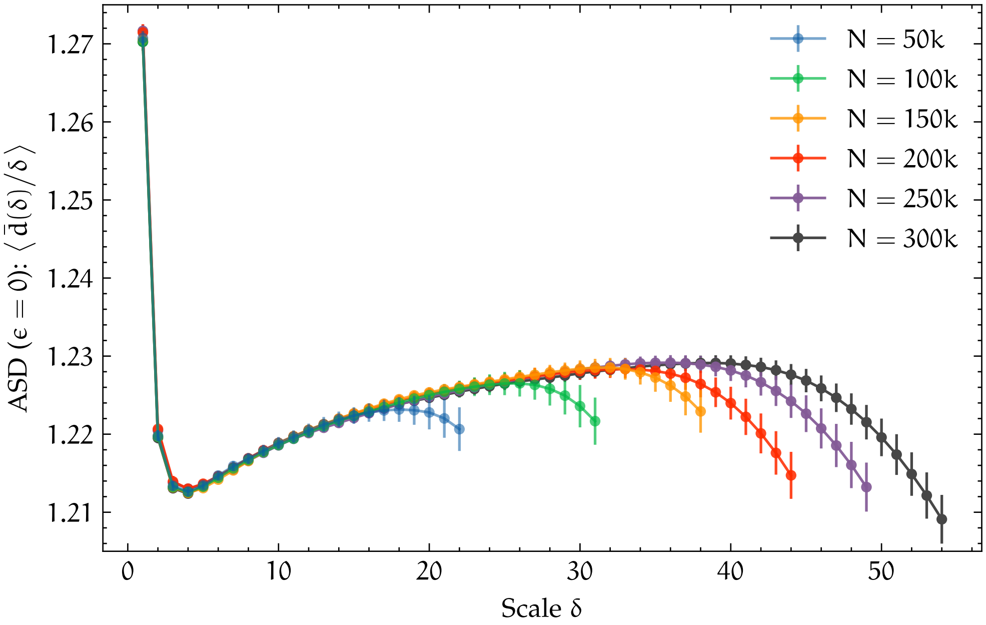

Figure 5.3: Ensemble average of the curvature profile or normalized average sphere distance $\langle \bar{d}^0_{av}(\delta)/\delta \rangle_{N_2}$ ($\epsilon = 0$) for different system sizes at $\daleth = 0.32$. The triangulation average (5.11) estimate is based on 5k point samples, and the ensemble average is estimated using 50 triangulations.

6. Topological effects

For the numerical study of 2D causal dynamical triangulations we use a toroidal topology, i.e. each spatial slice is a circle, and we identify the first and last slice. We are interested in studying the quasi-local geometry of CDT like the coarse-grained quantum Ricci curvature introduced in section 5, and the two-point functions that will be introduced in chapter 7. To be able to properly interpret these results we need to make sure that they are evaluated at length scales that reflect the local geometry of the triangulations, and are not influenced by the finite size of the triangulations.

A simple example of this effect can be illustrated with the volume of balls. Consider a classical flat two-torus created by identifying the opposing sides of a unit square (side lengths 1), inside which we place a geodesic ball[1] $\mathcal{B}(r)$ of radius r; a diagram of this situation is shown in Fig. 6.1. As long as the radius $r \leqslant \frac{1}{2}$ the ball will have the same shape and 2-volume $\operatorname{Vol}\mathcal{B}(r) = \pi r^2$ as in a flat infinite plane. However, when the radius $r > \frac{1}{2}$ the ball will overlap with itself and its volume will increase less, so $\operatorname{Vol}\mathcal{B}(r) < \pi r^2$. This continues until $r \geqslant \frac{1}{2}\sqrt{2}$, when the ball has filled the entire torus and the volume is $\operatorname{Vol}\mathcal{B}(r) = 1$. This means the 1-volume of the geodesic sphere $S(r)$ (the boundary of the geodesic ball) will decrease for $r > \frac{1}{2}$ until it is 0. The volume profiles of the ball and sphere on a torus, compared to those on an infinite plane are shown in Fig. 6.2.

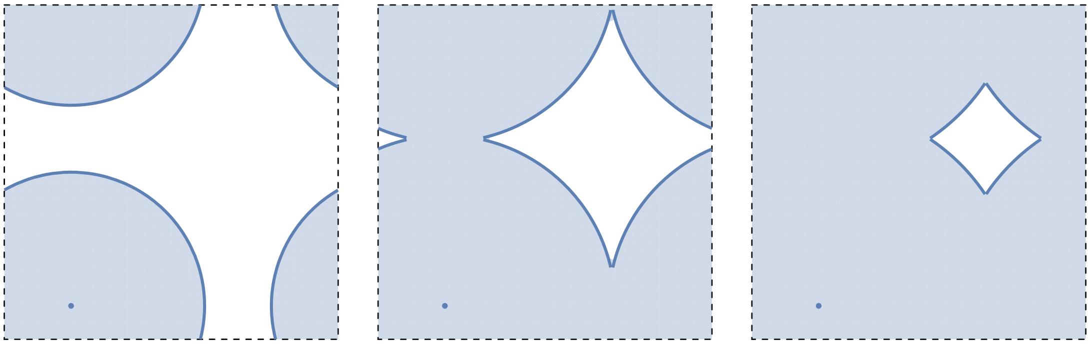

Figure 6.1: Visualization of a growing ball in a two-torus (the opposing sides of the square are associated with one-other), where one can see the ball starts to overlap with itself after its radius becomes half that of the square side. The sphere (the boundary of the ball) is marked by a thick line.

We see the ball and sphere volumes are not the same for a flat torus and a flat plane at large enough radii; they are influenced by the global topology of the manifold, even though these manifolds have the same local geometry. We will call these effects *topological effects*. In a discretized setting the term *finite-size effects* is often used, as was done in the previous sections. Thus, if we want to investigate the quasi-local geometry using geodesic balls and spheres we can only correctly interpret results for radii smaller than half the smallest diameter L_{min} of toroidal manifold we consider. We define the smallest diameter L_{min} to be the length of the smallest non-contractible loop. For other quasi-local quantities with some length scale there will also be a maximum length scale, such that the results can still be interpreted correctly. For the average sphere distance $\bar{d}_{\text{av}}(\delta)$ ($\delta = \epsilon$) we need to make sure the spheres do not have any additional overlap. Additionally, we need to make sure that a geodesic between a point pair on the spheres does not wrap around the torus, giving a shorter distance than we would have had on a plane. The longest geodesic distance between points on the spheres can be 3δ, so no such wrapping will occur for $6\delta < L_{\text{min}}$. For the

---

[1] With a geodesic ball $\mathcal{B}(r)$ we mean the set of points that have the geodesic distance of r or less to a given origin, and the geodesic sphere $S(r)$ is its boundary given by the set of all points with geodesic distance r.

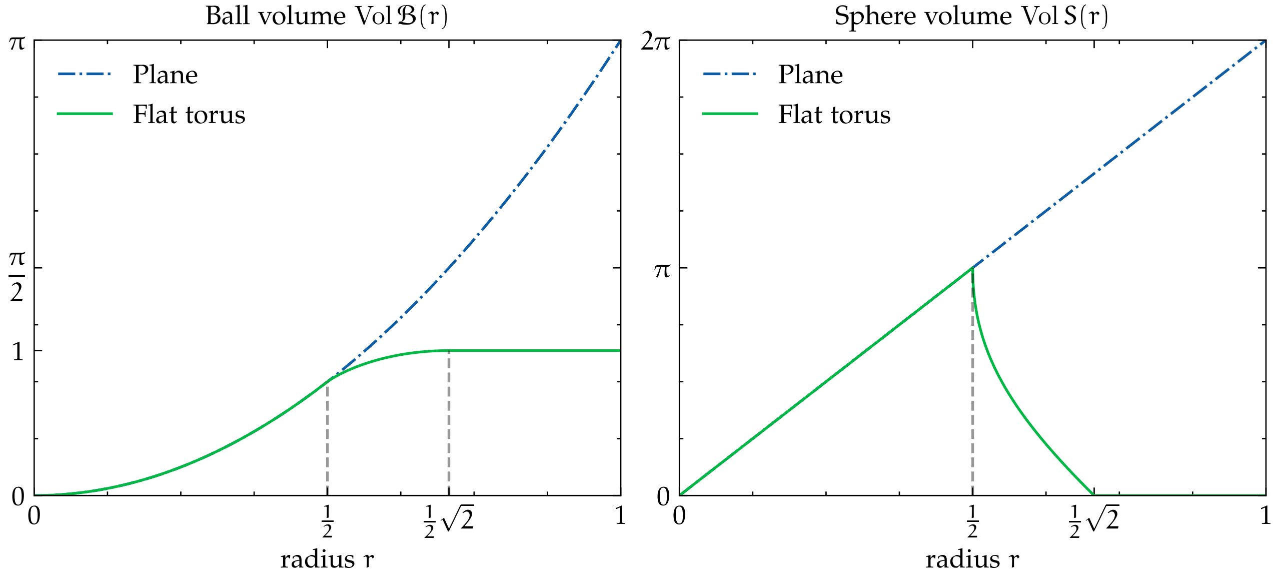

Figure 6.2: The volume profiles of a 2-ball (disk) and its boundary 1-sphere (circle), comparing an infinite plane with a flat torus.

average sphere distance with $\epsilon = 0$ the analogous condition is $4\delta < L_{\mathrm{min}}$.

Hence, to be able to correctly interpret our results for CDT we need to know what the smallest diameter[2] L_{min} of our toroidal triangulations is. We can easily get an upper bound on the smallest diameter, namely the number of spatial slices τ, as this will be the length of the smallest non-contractible timelike loop. However, the situation is much more complicated in the spatial direction. From the analytical analysis of 2D CDT [4] we know that the length of the spatial slices and the standard deviation are of the order of $\lambda^{-\frac{1}{2}}$, or on the order of $\sqrt{N_0}$ for a fixed volume. This means the length of the spatial slices can fluctuate strongly, and a triangulation may have some spatial slices with much shorter length than the average length; the smallest diameter L_{min} may be a lot smaller than the average spatial slice length N_0/τ. An example triangulation snapshot is shown in Fig. 6.3, illustrating the large difference in spatial slice lengths. In fact, if $\daleth = \tau^2/N_0$ is large enough we get a substantial number of triangulations with spatial slices of link length[3] 3. In this case $L_{\mathrm{min}} = 1$, so the interpretation range for the average sphere distance would be $6\delta < 1$.

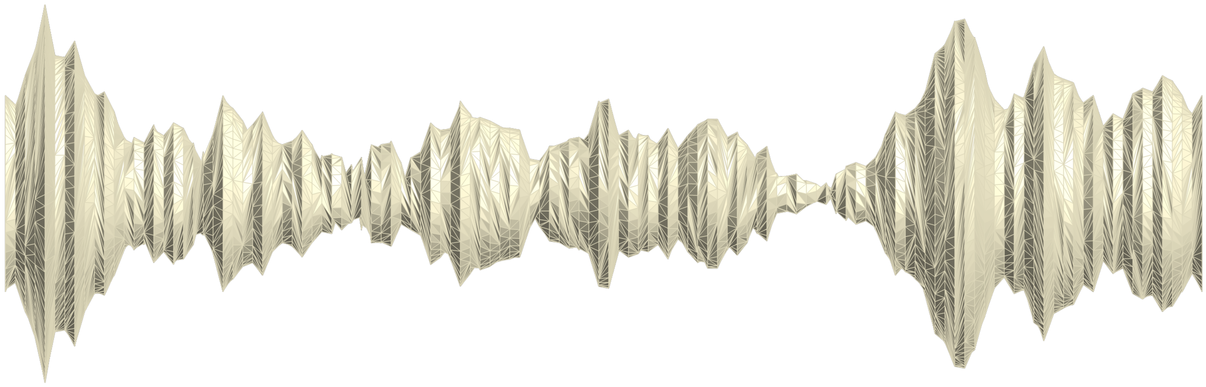

Figure 6.3: A visualization of a snapshot of a CDT triangulation of $N_2 = 10\text{k}$ and $\tau = 122$ ($\daleth = 3$), time runs from left to right and the first and last spatial slice should be identified.

---

[2] In the following we take the geodesic distance to be the link distance.

[3] Recall this is the smallest possible length a triangulation satisfying the simplicial manifold condition can have.

This means we cannot interpret the average sphere distance to be without finite-size effects for any δ. Moreover, even if we measure quantities in spatial slices with large lengths the short length spatial slices can still influence the results, because of the coarse-grained nature of the quantities we consider. Notably, a closed geodesic through a vertex that is situated in a spatial slice of large length, can be much shorter than the length of that spatial slice, because it may be shorter to go through neighbouring shorter spatial slices and back. Thus, for 2D CDT it is practically impossible to put a strict bound on the length scale of any quantity we want to consider, because in some small degree finite-size effects can occur at any length.

Instead of putting a strict bound on the length scales of the quantity by the minimal diameter of our triangulations, we will estimate how many of the measurements of the quantity are affected by finite-size effects, and determine an effective bound by measuring at what length scale the number of affected measurements is still acceptably low. This is very similar to what has been done for the average sphere distance in [22]. The method of determining when a measurement is affected by finite-size effects depends on the observable. But they all rely on determining how many times a geodesic has wrapped around the compact direction of the toroidal triangulation.

6.1 Cut-open triangulation

To identify how many times a path wraps around the triangulation we will cut open the triangulation, unfolding it to a ‘rectangle’. In order to do this we need to identify paths along which to cut. We will use two closed non-contractible loops: one timelike and one spacelike loop. For the spacelike loop we can use a time-slice and for the timelike loop we can use any closed timelike geodesic. The original toroidal triangulation can then be retrieved from the cut-open triangulation by identifying the opposing sides. We use this ‘rectangle’ to tile a two-dimensional plane. We do this by making copies, which we call *patch*es, of the cut-open triangulation and gluing them to each other. These steps are illustrated in Fig. 6.4. This results in an infinite triangulation with a repeating geometry. We will then assign a unique label[4] to every vertex by using the label of the corresponding vertex of the original triangulation together with which copy of the original triangulation it is in. As such we can easily see which vertices correspond to the same vertex on the

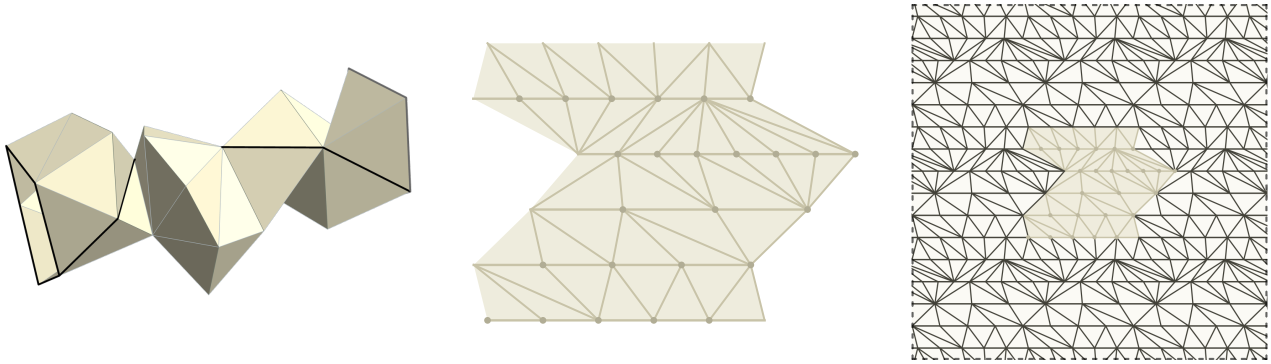

Figure 6.4: Illustration of the cutting procedure. Starting from a toroidal triangulation on the left (the marked leftmost and rightmost spatial slices should be identified), we cut it open along the spatial slice and time-like geodesic marked with a thick black line. This yields the cut-open triangulation in the middle. The cut-open triangulation is used to tile the plane as displayed in the right figure, where a single patch of the vertices, edges and triangles of the triangulation is marked.

---

[4] In the numerical simulation we specifically use the label (i, t, x). The i is the corresponding original label, t the ‘time’ label of the patch (the base patch has $t = 0$ the following future-directed patches $t = 1, 2, \ldots$ and the past-directed patches $t = -1, -2, \ldots$), and x the ‘space’ label of the patch (the base patch has again $x = 0$ and the following right patches $x = 1, 2, \ldots$ and the left patches $x = -1, -2, \ldots$). Strictly speaking there is no ‘base’ patch as all patches are

original triangulation. We can now do measurements on this cut-open triangulation instead of the toroidal triangulation, which will give the same results for length scales for which no wrapping occurs. But crucially, on the cut-open triangulation no wrapping can occur as it has planar topology. However, we can determine when wrapping would have occurred in the original toroidal triangulation by tracking when another copy of a vertex is/would have been used for the measurement. We will illustrate this more clearly for the specific observables.

Note that we can do measurements on the cut-open triangulation without having wrapping effects. However, this does not necessarily mean measurements on the cut-open triangulation give the same results as measurements on a toroidal triangulation with infinite volume. This is because the geometry of the cut-open graph is periodic, which will affect some observables, like two-point functions for example. So, the cut-open triangulation is associated with a length scale. And for larger length scales results measured on this cut-open graph cannot be interpreted as free from finite-size effects. Finally, we note that this procedure can be extended to be applied to higher-dimensional toroidal topologies, if a systematic study of wrapping effects is desired.

6.2 Sphere volumes

To determine at what radius the volume of a geodesic ball and sphere are subject to finite-size effects is rather simple using the cut-open triangulation. We grow the geodesic ball $\mathcal{B}_p(r-1)$ with radius $r-1$ from a vertex p of the cut-open triangulation. Then we check the number $u_p(r)$ of the vertices $q \in S_p(r)$, which have another copy of q in $\mathcal{B}_p(r-1)$. If $u_p(r) \geqslant 1$ this means the result is subject to finite-size effects. As discussed before, we will not discard all measurements for $r \geqslant r_{\max}$ where $r_{\max}$ is the smallest r for which $u_p(r) \geqslant 1$. Instead, we will consider the fraction of vertices

$$w_p(r) := \frac{u_p(r)}{\operatorname{Vol} S_p(r)} \tag{6.1}$$

that are affected. We can compute the average of $w_p(r)$ for all the sphere volume measurements we perform, and take $r_{\max}$ to be the smallest r for which $w_p(r)$ exceeds some small ratio, which we no longer consider to be acceptable. The measurement results of the average of $w(r)$, for sphere volume $\operatorname{Vol} S(r)$ in 2D CDT for several two-volumes N_2, are displayed in Fig. 6.5. These show there is a considerable region of r where little to no wrapping effects occur, and where we can reasonably interpret the sphere volume results as being free of finite-size effects.

For the measurements of the Hausdorff dimension in section 4.2 we made use of $r_{\max}$, by performing a fitting procedure (as described in that section) to the average sphere volume, using the region $5 < r < r_{\max}$ (the first few points are excluded because of discretization effects). For this, we used a maximum allowed wrapping fraction of $w(r_{\max}) = 5 \times 10^{-3}$. To show the $r_{\max}$ that are used for this fitting on the average sphere volume $\left\langle \overline{\operatorname{Vol} S(r)} \right\rangle_{N_2}$, we present Fig. 6.6. This figure shows the estimates of the sphere volume $\left\langle \overline{\operatorname{Vol} S(r)} \right\rangle_{N_2}$ as measured on the toroidal triangulation and the cut-open triangulation. For each volume N_2 a vertical dashed line is included indicating the $r_{\max}$ used based on the maximum allowed wrapping fraction of $w(r_{\max}) = 5 \times 10^{-3}$. From this figure we can see that for $r < r_{\max}$ the average sphere volume is identical up to our statistical accuracy between the measurements on the toroidal triangulations and cut-open triangulations, as expected. For $r > r_{\max}$ these results start to be different, due to finite-size effects. From these measurements from the cut-open triangulation, we can see that also in the region $r > r_{\max}$ the estimates of the average sphere volume for different volumes N_2 overlap. This indicates that the periodic geometry of the cut-open triangulation has little influence on the average sphere volumes for $r > r_{\max}$ to at least $2r_{\max}$. This suggests that the average sphere volume as measured on

---

equivalent. We choose one of the patches to be $(t = 0, x = 0)$, and call this the *base patch*.

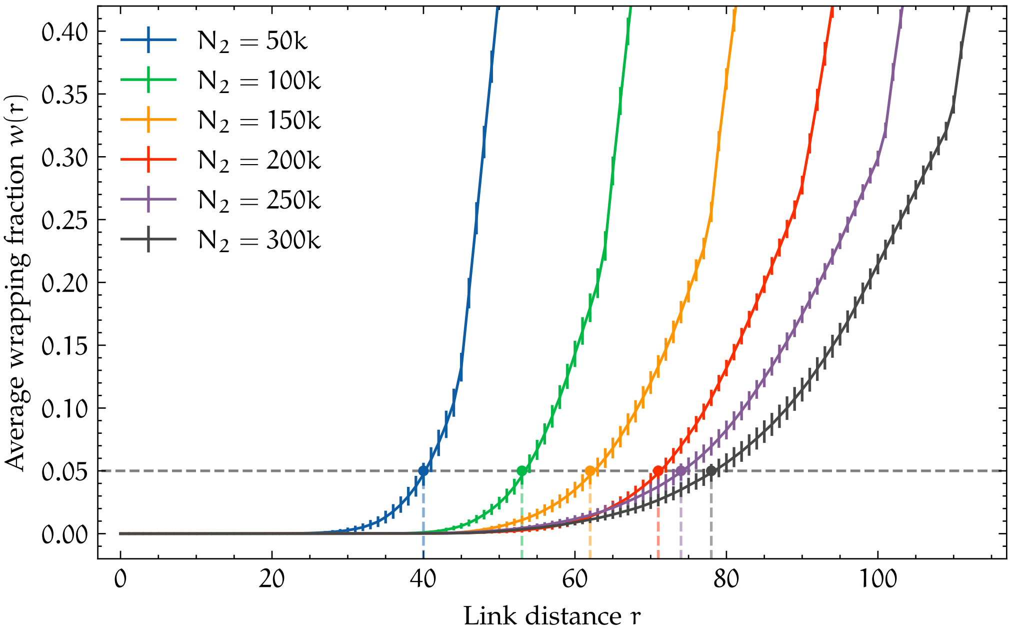

Figure 6.5: The average fraction $w(r)$ of vertices in the measured spheres $S(r)$ that are subject to wrapping effects for 2D CDT, as explained in section 6.2. For this example r_{max} is marked for each size N_2 of triangulation for a maximum acceptable $w(r_{max}) = 0.05$ (this is a lot larger than is actually considered acceptable for the Hausdorff dimension measurements). All the triangulations in this plot use $\daleth = \tau^2/N_0 = 0.32$.

the cut-open triangulation may be equal to the average sphere volume as measured on a toroidal triangulation with infinite volume N_2 for r significantly larger than r_{max}.

Finally, we want to note that we expect r_{max} to scale with the average length of the spatial slices, because we expect the effective minimal length of the spatial slices to be proportional to their average length. Given that we keep $\daleth = \tau^2/N_0$ constant, this means that the average length and r_{max} should scale with $\sqrt{N_2}$. We attempted to measure the behaviour of r_{max} with respect to the volume N_2, but our statistical uncertainty is too large to verify this claim.

6.3 Average sphere distance

To determine at what δ the average sphere distance $\bar{d}_{av}(\delta)$ is subject to finite-size effects, we will do essentially the same as in [22] using winding numbers. For the average sphere distance we can consider two different types of wrapping effects (called level-1 and level-2 violations in [22]):

1. The spheres themselves do not additionally overlap, but the paths of the shortest distance between points on the spheres wrap around the triangulation.
2. The spheres themselves overlap by wrapping around the triangulation (besides overlapping already without wrapping).

Note that wrapping effect 2 is stronger than 1, in that δ needs to be larger for 2 to occur. Wrapping effect 2 can be detected with the cut-open triangulation in the same way as is done for sphere volumes, by checking when the spheres contain copies of vertices that are already in their interior balls. For wrapping effect 1 we proceed as follows. We grow the two spheres from p and p' on the cut-open triangulation and determine the geodesic distance from vertex q to q' on the respective spheres $S_p(\delta)$ and $S_{p'}(\delta)$). This geodesic can never 'wrap around' on the cut-open triangulation, but we can check if there are geodesics to other copies of q' that are shorter. If this is the case, we

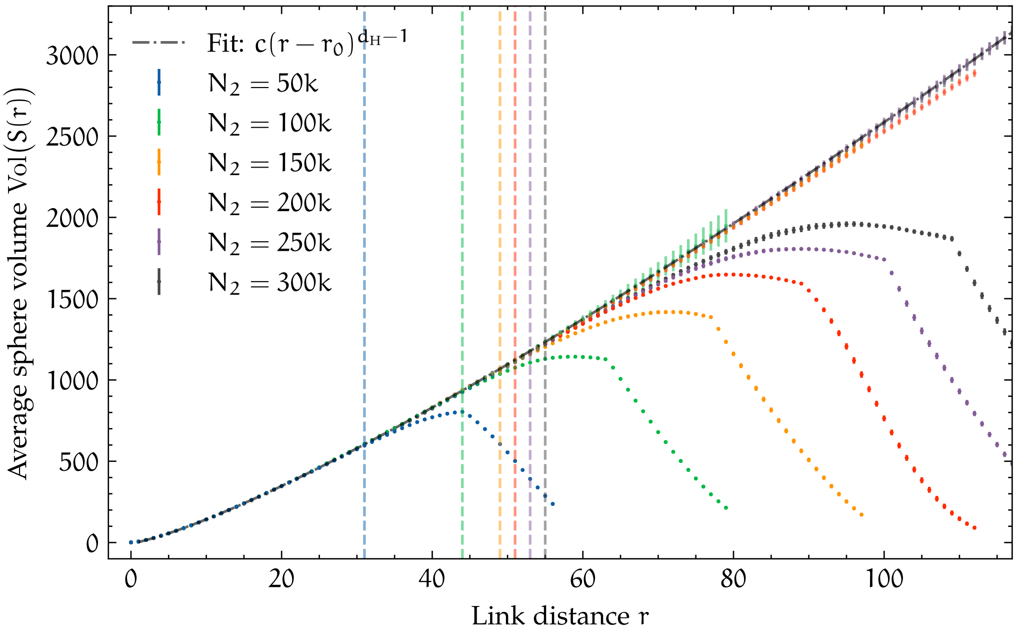

Figure 6.6: Sphere volume estimates for 2D CDT at several volumes N_2 with $\daleth = 0.32$. The results for both the measurements on the compact toroidal triangulation and on the cut-open triangulation are presented in the same colour. The results for the compact toroidal triangulation are the same as those presented in section 4.2, and decrease for large r. The results for the cut-open triangulation are presented with a lower opacity, and do not decrease for large r. Note that the results overlap, making them difficult to distinguish. The $r_{\max}$ used to determine the fitting region for the Hausdorff dimension in section 4.2 is displayed using dashed vertical lines. Finally, a power law fit used to estimate the Hausdorff dimension (see section 4.2) is included for the triangulation with the largest volume N_2 with a black dash-dotted line.

know we would have found a geodesic that wrapped around in the original toroidal triangulation. So we count the number of point pairs (q, q') on the spheres $S_p(\delta)$ and $S_{p'}(\delta))$ that have a geodesic that would have been subject to wrapping effects $u_{p,p'}(\delta)$ on the toroidal triangulation. Again we consider the fraction of point pairs

$$w_{p,p'}(\delta) = u_{p,p'}(\delta)\left(\mathrm{Vol}\, S_p(\delta)\, \mathrm{Vol}\, S_{p'}(\delta)\right)^{-1} \tag{6.2}$$

that are affected. Then we take the average of $w_{p,p'}(\delta)$ over all sphere pairs we measure for the average sphere distance. We take $\delta_{\max}$ to be the smallest δ for which the average $w(\delta)$ exceeds a small threshold, which we no longer consider to be acceptable. In this way we can consider the average sphere distance $\langle \bar{d}_{av}(\delta) \rangle$ to be without too many finite-size effects for $\delta < \delta_{\max}$.

Note that we determine $\delta_{\max}$ solely on the occurrence of wrapping effect 1, because wrapping effect 2 will occur for δ larger than 1 (this can be seen in the results of [22]). Since we are interested in a lower bound of $\delta_{\max}$, only considering wrapping effect 1 is sufficient.

Using the described method, we measured the wrapping fractions $w(\delta)$ as given by (6.2) for the average sphere distance $\bar{d}$ for $\epsilon = \delta$ and $\epsilon = 0$. We present the results for the average wrapping fraction $w(\delta)$ in Fig. 6.7 and Fig. C.3[5] for ASD with $\epsilon = \delta$ and $\epsilon = 0$ respectively. From these figures we can see there is a considerable region of δ, where the wrapping fractions are small, and we can reasonably argue that the result of the ASD measurements is not affected by finite-size effects. We did not measure many samples (around 600 varying for the different volumes N_2) of the wrapping fraction $w(\delta)$, as it is rather computationally expensive to compute the average sphere distance for

---

[5] Fig. C.3 is qualitatively very similar to 6.7, so it is put in the appendix to avoid needlessly much space being taken up by figures.

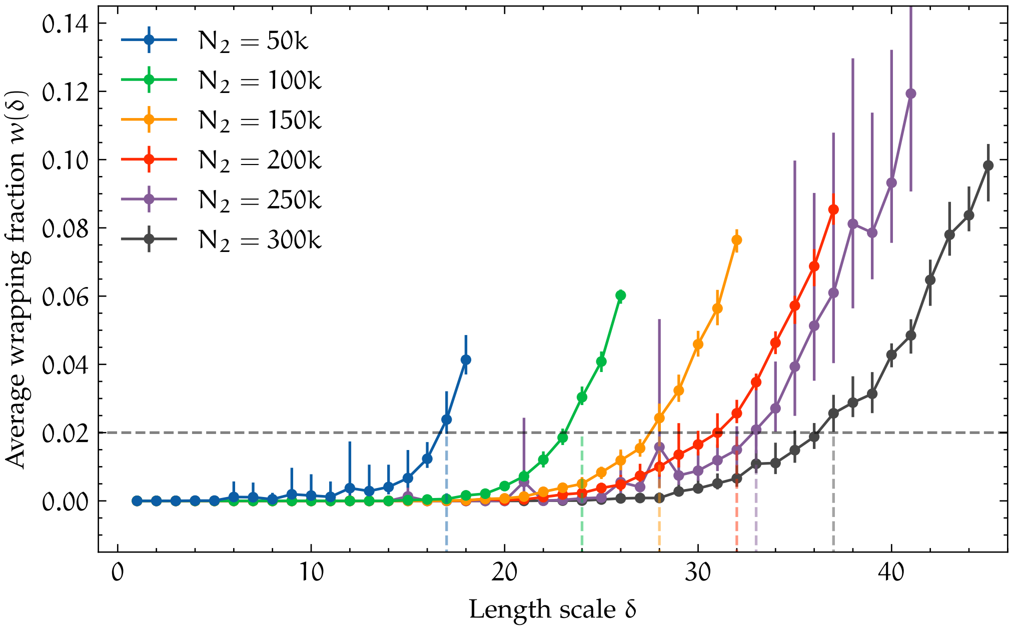

Figure 6.7: Average wrapping fraction $w_{p,p'}(\delta)$ (6.2) for average sphere distance $\delta_{p,p'}(\delta)$ with $\delta = \epsilon$ in 2D CDT with $\daleth = 0.32$. As an example, we include the $\delta_{\max}$ using a vertical dashed line for each triangulation volume N_2 for a maximum allowed wrapping fraction of $w(\delta_{\max}) = 0.02$ (this is a lot larger than what is actually considered an acceptable amount of wrapping effects).

larger δ on the cut-open triangulation. The estimation of the wrapping fraction is therefore not very accurate, as can be seen from the significant statistical uncertainty on the estimates of Fig. 6.7 and Fig. C.3. This means that our estimates of $\delta_{\max}$, the maximum δ for which the wrapping fraction $w(\delta_{\max})$ is acceptably small, also have a large uncertainty. For a proper analysis of the δ region where wrapping effects are negligible, more measurements should be performed. In Fig. 6.8 and Fig. 6.9 we again present our results of the average sphere distance in 2D CDT for ASD with $\epsilon = \delta$ and $\epsilon = 0$ respectively. Now, we included the $\delta_{\max}$ for each volume N_2 based on a maximum allowed wrapping fraction of $w(\delta_{\max}) = 1 \times 10^{-3}$ in case of $\epsilon = \delta$ and $w(\delta_{\max}) = 5 \times 10^{-4}$ for $\epsilon = 0$. From these figures we can see that the decreasing part of the average sphere distance for larger r only appears for $\delta > \delta_{\max}$. Thus, we can verify that this behaviour is due to finite-size effects, as we assumed in section 5.3.

Finally, we want to note that just like $r_{\max}$, we expect $\delta_{\max}$ to scale with the average length of the spatial slices. This would again mean that $\delta_{\max}$ should scale with $\sqrt{N_2}$. The statistical accuracy of our ASD wrapping fractions is even lower than for the sphere volumes, so also in this case we cannot numerically verify this claim.

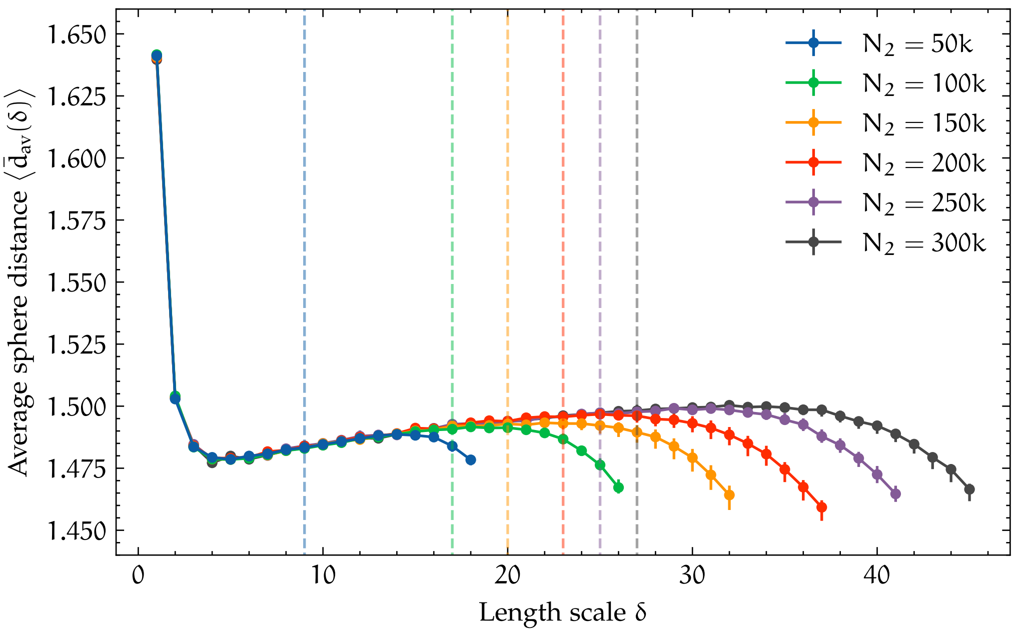

Figure 6.8: Curvature profile or normalized average sphere distance $\langle \bar{d}_{av}(\delta) \rangle$ (5.10) for $\delta = \epsilon$ in 2D CDT with $\daleth = 0.32$. We have marked the δ_{max} for every volume N_2 with a vertical dashed line, based on the maximum allowed wrapping fraction of $w(\delta_{max}) = 1 \times 10^{-3}$. We consider the average sphere distance to be minimally affected by finite-size effects for $\delta < \delta_{max}$.

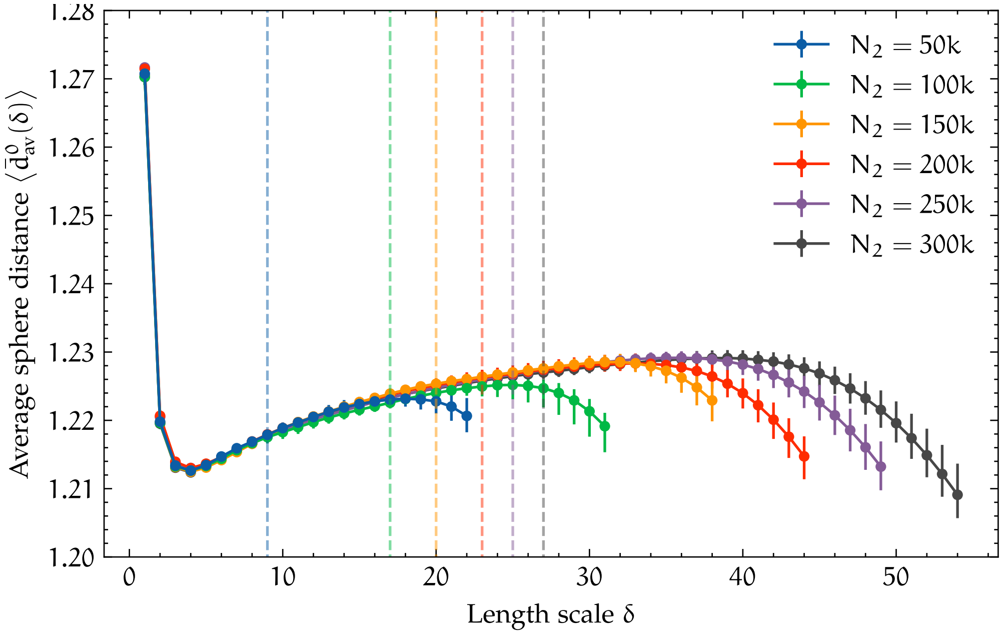

Figure 6.9: Curvature profile or normalized average sphere distance $\langle \bar{d}^0_{av}(\delta) \rangle / \delta$ (5.11) for $\epsilon = 0$ in 2D CDT with $\daleth = 0.32$. We have marked the δ_{max} for every volume N_2 with a vertical dashed line, based on the maximum allowed wrapping fraction of $w(\delta_{max}) = 5 \times 10^{-4}$. We consider the average sphere distance to be minimally affected by finite-size effects for $\delta < \delta_{max}$.

7. Two-point functions

Defining a two-point function is challenging in quantum gravity as we are severely restricted by diffeomorphism invariance, i.e. there can be no dependence on specific points. In a standard quantum field theory of a scalar field ϕ on a flat background the two-point function is defined as the vacuum expectation value[1]

$$G(x,y) = \langle\Omega|T\{\phi(x)\phi(y)\}|\Omega\rangle\,,$$

where $|\Omega\rangle$ denotes the vacuum state of the system. In a path integral formulation this is given by the functional integral

$$G(x,y) = \frac{1}{Z}\int \mathcal{D}\phi\,\phi(x)\phi(y)\,e^{iS[\phi]},$$

where $Z = \int \mathcal{D}\phi\,e^{iS[\phi]}$ and $S[\phi]$ is the action of the scalar field. In this standard QFT example we are able to make sense of the points x and y, because we are working on a fixed background. In quantum gravity the geometry itself is dynamical, so there is no way to identify specific points x and y between different geometries. Thus, our two-point function has to be diffeomorphism-invariant, there can be no dependence on a specific point. In the following sections we will discuss how we will define two-point functions in quantum spacetimes and what complications arise in these spacetimes. In fact, defining a diffeomorphism-invariant two-point function for a single configuration of the quantum ensemble already illuminates many of the difficulties, so we will start here.

7.1 'Classical' two-point functions

We will attempt to define a two-point function on a single manifold and forget about taking the path integral over all manifolds for a moment, hence the use of the word 'classical'. However, it is still important to realize that in the end we are interested in the behaviour of quantum spacetimes, and we will be taking a path integral over whatever two-point function we define. So one should think of the manifolds discussed here as a typical manifold in the quantum ensemble. In general, such a manifold is not smooth, in fact in some quantum gravity theories like 2D EDT and CDT the manifolds obtained in the continuum limit are nowhere differentiable.

With this and the restriction that our two-point function should be diffeomorphism-invariant in mind, we define an *integrated* two-point function, which is a function of the geodesic distance between two points. This restriction leads us to consider the unnormalized (integrated) two-point function[2] of two *local* field quantities ϕ_1 and ϕ_2, which themselves can depend on the geometry. On a given n-dimensional compact Riemannian manifold M with metric $g_{\mu\nu}$, it is given by

$$G_g^{\phi_1\phi_2}(r) = \int d^n x\,\sqrt{g(x)}\int d^n y\,\sqrt{g(y)}\,\phi_1(x)\phi_2(y)\,\delta(d_g(x,y)-r), \tag{7.1}$$

where[3] $g(x)$ denotes the metric determinant, and $d_g(x,y)$ is the geodesic distance between x and y with respect to metric $g_{\mu\nu}$. $G_g^{\phi_1\phi_2}(r)$ can be interpreted as the integral over all $\phi_1(x)\phi_2(y)$ over all possible point pairs (x, y) with geodesic separation r, where the Dirac delta $\delta(d_g(x, y) - r)$ realizes the selection of the point pairs. Note that this definition of a two-point function is symmetric under exchange of the fields, i.e. $G_g^{\phi_1\phi_2}(r) = G_g^{\phi_2\phi_1}(r)$. Interesting to note is that, when considering the path integral of this two-point function (7.1), we can view it as a kind of three-operator correlation function since $\delta(d_g(x, y) - r)$ is a complicated non-local operator for any non-trivial geometry as remarked by [25]; this is in contrast to flat space. We can also view (7.1) in an asymmetric looking way by removing the Dirac delta by evaluating one of the integrals,

---

[1] As viewed in the Heisenberg picture, the field operators having the time dependence.

[2] A lot of new notation will be introduced in this chapter, which may make it difficult to follow when the notation does not make sense to the reader. We will provide footnotes to highlight features and possible points of confusion.

[3] The (unnormalized) two-point functions will be denoted by $G_g^{\phi_1\phi_2}(r)$. We use subscript g to indicate that this is the two-point function of a single manifold. The superscript is used to indicate the two-point function is taken of the fields $\phi_1(x)$ and $\phi_2(y)$, where the left quantity corresponds to the first integration variable x and the right quantity

$$G_g^{\phi_1\phi_2}(r) = \int d^n x \sqrt{g(x)} \int_{S_x(r)} d^{n-1} y \sqrt{h(y)}\, \phi_1(x)\phi_2(y), \tag{7.2}$$

where $S_x(r)$ is the geodesic sphere around the point x with radius r[4], and $h(y)$ denotes the determinant of the induced metric on $S_x(r)$. In this form the two-point function no longer looks symmetric, but it still is of course; alternatively we could have evaluated one of the 'x' integrals, swapping around the integrals. In this form of the integrated two-point function we interpret it differently. Now we have an integral over all points in the geodesic sphere $S_x(r)$, which itself is then integrated over all points x in the manifold. The form (7.2) suggests a different way to normalize this two-point function than the original form (7.1), as we will see in the next section.

7.1.1 Normalization

Now that we have a definition for an unnormalized (integrated) two-point function on a given manifold as given by (7.1), we need to define how we normalize it and how we will define a connected two-point function. Doing so leads to ambiguities, which is what we will discuss in the following sections.

Starting from (7.1), the integral over all r-separated points pairs, it seems natural to normalize it by dividing by the number of such point pairs. Hence, a possible definition for the normalized two-point function[5] is

$$\tilde{G}_g^{\phi_1\phi_2}(r) = \frac{G_g^{\phi_1\phi_2}(r)}{G_g^{\mathbf{11}}(r)} = \frac{\displaystyle\int d^n x \sqrt{g(x)} \int d^n y \sqrt{g(x)}\, \phi_1(x)\phi_2(y)\, \delta(d_g(x, y) - r)}{\displaystyle\int d^n x \sqrt{g(x)} \int d^n y \sqrt{g(x)}\, \delta(d_g(x, y) - r)}, \tag{7.3}$$

which can be interpreted as the average of $\phi_1(x)\phi_2(y)$ over all r-separated point pairs. Note here that the normalization factor itself is a non-trivial object, due to the Dirac delta being a complex non-local object,

$$\begin{aligned} G_g^{\mathbf{11}}(r) &= \int d^n x \sqrt{g(x)} \int_{S_x(r)} d^{n-1} y \sqrt{h(y)} && (7.4) \\ &= \int d^n x \sqrt{g(x)}\, \mathrm{Vol}\, S_x(r) \\ &= \mathrm{Vol}\, M\, \overline{\mathrm{Vol}\, S(r)}, && (7.5) \end{aligned}$$

where the $\mathrm{Vol} \cdots$ denotes the total volume of the given (sub)manifold with respect to the induced metric, so $\mathrm{Vol}\, M = \int d^n x \sqrt{g(x)}$ and $\mathrm{Vol}\, S_x(r) = \int_{S_x(r)} d^{n-1} y \sqrt{h(y)}$; and the bar or overline is

---

to the second integration variable y (this difference will be important later when asymmetric two-point functions are introduced); if left and right the field quantities are not clearly separable we will also use the notation G^{ϕ_1,ϕ_2} to avoid ambiguity.

[4] The geodesic sphere is already defined in chapter 5

[5] We will use a tilde $\tilde{\dots}$ to denote normalized quantities like the normalized two-point function $\tilde{G}_g^{\phi_1\phi_2}(r)$.

used to denote the manifold average

$$\overline{Q} = \frac{1}{\mathrm{Vol}\, M} \int d^n x \, \sqrt{g(x)}\, Q(x). \tag{7.6}$$

Note that $G_g^{\mathbf{11}}(r)$ can in general also be different for manifolds with the same volume, which is something to take into account when taking the path integral later. Also, $\mathrm{Vol}\, S_x(r)$ is in general x-dependent, which is a complication that one does not have in maximally symmetric Riemannian spaces like flat space, where $\mathrm{Vol}\, S_x(r) = \overline{\mathrm{Vol}\, S(r)}$ for all x. The normalization factor (7.4) can be interpreted as the number of r-separated point pairs, or as a manifold average with an additional normalization by the average volume of geodesic spheres by (7.5).

This leads us to suggest another, inequivalent normalization of the two-point function, which seems more natural starting from the asymmetric looking form of (7.2),

$${}^*\tilde{G}_g^{\phi_1\phi_2}(r) = \frac{1}{\mathrm{Vol}\, M} \int d^n x \, \sqrt{g(x)}\, \frac{1}{\mathrm{Vol}\, S_x(r)} \int_{S_x(r)} d^{n-1} y \, \sqrt{h(y)}\, \phi_1(x)\phi_2(y), \tag{7.7}$$

where instead of normalizing the two integrals together, we normalize the inner integral for each point separately, so we have the average of $\phi_1(x)\phi_2(y)$ of the sphere around each point x and then averaged over all x. In a maximally symmetric space where $\mathrm{Vol}\, S_x(r) = \overline{\mathrm{Vol}\, S(r)}$, (7.3) and (7.7) are equivalent. However, on a general manifold they are not. It is important to note that (7.7) is not symmetric[6] under exchange of $\phi_1(x)$ and $\phi_2(y)$, if $\phi_1(x) \neq \phi_2(x)$ for some x. If one insists on having a symmetric two-point function one could symmetrize $\frac{1}{2}\left({}^*\tilde{G}_g^{\phi_1\phi_2}(r) + {}^*\tilde{G}_g^{\phi_2\phi_1}(r)\right)$; we will take (7.7) as is and investigate its properties.

Now, we wish to investigate how $\tilde{G}_g^{\phi_1\phi_2}(r)$ and ${}^*\tilde{G}_g^{\phi_1\phi_2}(r)$ differ. We first note that they can be related by an r-dependent weighting,

$$\begin{aligned}
\tilde{G}_g^{\phi_1\phi_2}(r) &= \frac{1}{\mathrm{Vol}\, M \overline{\mathrm{Vol}\, S(r)}} \int d^n x \, \sqrt{g(x)} \int_{S_x(r)} d^{n-1} y \, \sqrt{h(y)}\, \phi_1(x)\phi_2(y) \\
&= \frac{1}{\mathrm{Vol}\, M} \int d^n x \, \sqrt{g(x)} \frac{1}{\mathrm{Vol}\, S_x(r)} \int_{S_x(r)} d^{n-1} y \, \sqrt{h(y)}\, \frac{\mathrm{Vol}\, S_x(r)}{\overline{\mathrm{Vol}\, S(r)}} \phi_1(x)\phi_2(y) \\
&= {}^*\tilde{G}_g^{\hat{\phi}_1\phi_2}(r), \qquad \text{where } \hat{\phi}(x;r) := \frac{\mathrm{Vol}\, S_x(r)}{\overline{\mathrm{Vol}\, S(r)}} \phi(x).
\end{aligned} \tag{7.8}$$

So the different normalization are related by a weighting of the first field quantity. Note that this weighting cannot be understood as a different discretization with a different association of local volume element, because this weighting is non-local as it is r-dependent. An example of the different normalizations is shown in Fig. 7.1 using the vertex degree $\phi_1 = \phi_2 = c$ for 2D CDT[7]. From this figure we can see a significant difference for small correlation distances r, but for the vertex degree the different normalizations are indistinguishable for larger $r \gtrsim 10$.

7.1.2 Connected two-point function

Next we turn our attention to constructing the connected two-point function. The connected two-point function is the two-point function of the deviation from the mean of the field quantities.

---

[6] This normalized two-point function is not symmetric so the order matters. Important to note is that the notation ${}^*\tilde{G}^{\phi_1\phi_2}$ means the first superscript $\phi_1(x)$ is associated with the integration over x and the second superscript $\phi_2(y)$ is associated with the integration over y as defined in (7.7).

[7] At this stage we have not yet defined the discretization or ensemble averaging of the two-point function, which are used for the measurement of these two-point function in 2D CDT. This will be defined in the following sections, but for now this just serves to illustrate the difference.

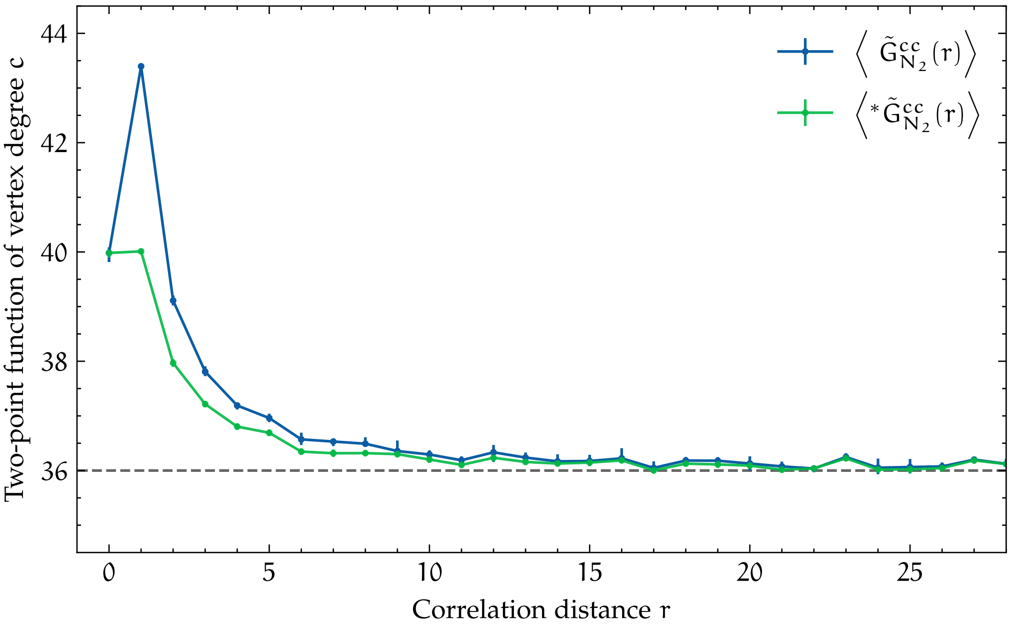

Figure 7.1: Comparison of the ensemble average of different normalizations $\left\langle \tilde{G}^{cc}_{T}(r) \right\rangle$ (7.3) and $\left\langle {}^{*}\tilde{G}^{cc}_{T}(r) \right\rangle$ (7.7) of the two-point function of vertex degree c. This is measured for 2D CDT with $N_2 = 300\mathrm{k}$ and $\tau = 219$ using link distance r on the vertex graph.

As such, we have to determine what mean to use. Most straightforward is to take the manifold average (7.6) of the field quantities $\overline{\phi_1}$ and $\overline{\phi_2}$. This results in the (unnormalized) connected two-point function[8] [25, 26]

$$\mathcal{G}^{\phi_1\phi_2}_{1,g}(r) = \int d^n x \sqrt{g(x)} \int d^n y \sqrt{g(y)} \left(\phi_1(x) - \overline{\phi}_1\right)\left(\phi_2(y) - \overline{\phi}_2\right) \delta(d_g(x,y) - r). \tag{7.9}$$

This connected two-point function $\mathcal{G}^{\phi_1\phi_2}_{1,g}$ can be written out:

$$\begin{aligned}\mathcal{G}^{\phi_1\phi_2}_{1,g}(r) &= \int d^n x \sqrt{g(x)} \int d^n y \sqrt{g(y)} \left(\phi_1(x) - \overline{\phi}_1\right)\left(\phi_2(y) - \overline{\phi}_2\right) \delta(d_g(x,y) - r) \\ &= G^{\phi_1\phi_2}_{g}(r) - \overline{\phi}_2\, G^{\phi_1\mathbf{1}}_{g}(r) - \overline{\phi}_1\, G^{\mathbf{1}\phi_2}_{g}(r) + \overline{\phi}_1\overline{\phi}_2\, G^{\mathbf{11}}_{g}(r).\end{aligned} \tag{7.10}$$

This can be normalized using the first prescription (7.3) to give

$$\tilde{\mathcal{G}}^{\phi_1\phi_2}_{1,g}(r) = \tilde{G}^{\phi_1\phi_2}_{g}(r) - \overline{\phi}_2\tilde{G}^{\phi_1\mathbf{1}}_{g}(r) - \overline{\phi}_1\tilde{G}^{\mathbf{1}\phi_2}_{g}(r) + \overline{\phi}_1\overline{\phi}_2. \tag{7.11}$$

Using the alternative asymmetric normalization of (7.7) yields

$${}^{*}\tilde{\mathcal{G}}^{\phi_1\phi_2}_{1,g}(r) = {}^{*}\tilde{G}^{\phi_1\phi_2}_{g}(r) - \overline{\phi}_1\, {}^{*}\tilde{G}^{\mathbf{1}\phi_2}_{g}(r) \tag{7.12}$$

Note that we get additional, perhaps unexpected, terms involving[9] $G^{\mathbf{1}\phi}_{g}(r)$. This is the $\mathbf{1}, \phi$ two-point function, which can be interpreted as the two-point function of the local volume element $d^n x \sqrt{g(x)}$ with $\phi(y)$. Investigating this term further we find

$$G^{\mathbf{1}\phi}_{g}(r) = \int d^n x \sqrt{g(x)} \int d^n y \sqrt{g(y)}\, \phi(x)\, \delta(d_g(x,y) - r)$$

---

[8] We introduce a calligraphic $\mathcal{G}$ to denote the connected two-point function. We will have two different definitions for the connected two-point function, so we differentiate between them with a subscript: $\mathcal{G}_1$ and $\mathcal{G}_2$.

[9] Recall that $G^{\mathbf{1}\phi}_{g}(r) = G^{\phi\mathbf{1}}_{g}(r)$ and $\tilde{G}^{\mathbf{1}\phi}_{g}(r) = \tilde{G}^{\phi\mathbf{1}}_{g}(r)$ by symmetry, but ${}^{*}\tilde{G}^{\mathbf{1}\phi}_{g}(r) \neq {}^{*}\tilde{G}^{\phi\mathbf{1}}_{g}(r)$ in general.

$$= \int d^n x \sqrt{g(x)}\ \mathrm{Vol}\, S_x(r)\phi(x)$$

$$G_g^{\mathbf{1}\phi}(r) = G_g^{\mathbf{11}}\tilde{G}_g^{1\phi} = G_g^{\mathbf{11}}(r)\,\overline{\hat{\phi}(r)}. \tag{7.13}$$

We see that the normalized $\tilde{G}_g^{\mathbf{1}\phi}(r)$ can be interpreted as $\overline{\hat{\phi}(r)}$, an r-dependent weighted average[10] of ϕ, with the weights as defined in (7.8). To see how this weighted average $\overline{\hat{\phi}}(r)$ differs from the manifold average ϕ, we show an example[7] of the vertex degree $\phi = c$ in 2D EDT (Euclidean dynamical triangulation)[11] in Fig. 7.2. From this figure one can see that the weighted mean is higher than the normal manifold average for small r, and for large r, nearing the effective size of the triangulation, the weighted mean[12] is slightly smaller. In a maximally symmetric Riemannian space like a sphere, we have $\mathrm{Vol}\, S_x(r) = \overline{\mathrm{Vol}\, S(r)}$ for all x, and we find that the weighted average $\overline{\hat{\phi}(r)} = \overline{\phi}$ is equal to the manifold average. In this case (7.11) simplifies to

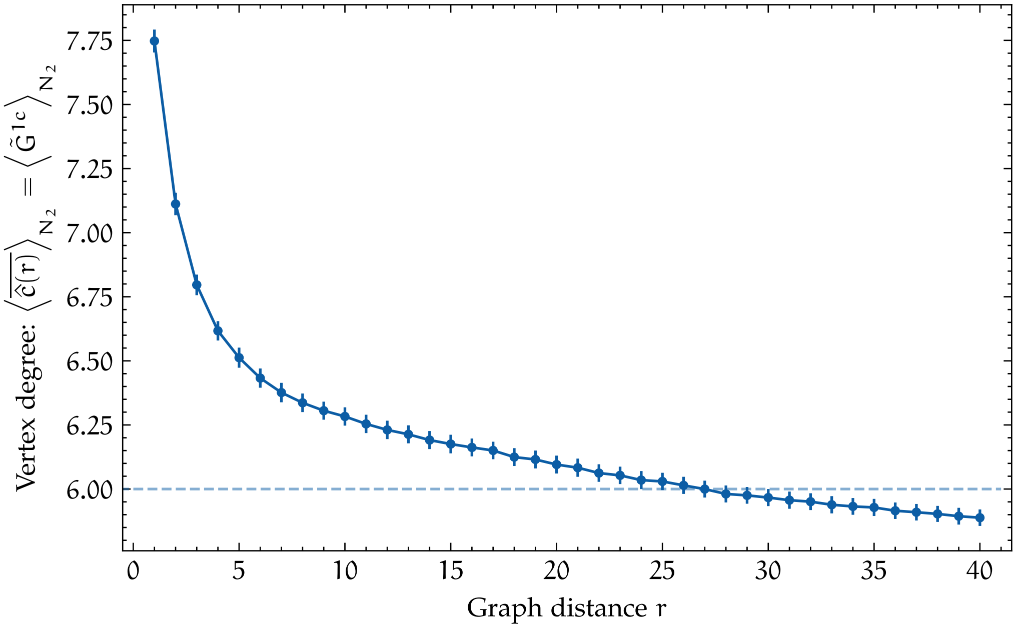

Figure 7.2: Ensemble average of weighted mean of the vertex degree $\left\langle \overline{\hat{c}(r)} \right\rangle_{N_2} = \left\langle \tilde{G}_{N_2}^{\mathbf{1}c}(r) \right\rangle$ for 2D EDT for $N_2 = 200\mathrm{k}$. Note that the ensemble average of the vertex degree $\bar{c} = 6(1 - 2/N_2) \approx 6$ is indicated with the dashed line.

$$\tilde{\mathcal{G}}_{1,g}^{\phi_1\phi_2}(r) = \tilde{G}_g^{\phi_1\phi_2}(r) - \overline{\phi}_1\overline{\phi}_2, \tag{7.14}$$

---

[10] Note that in the other normalization (7.7), we have ${}^*\tilde{G}_g^{\phi\mathbf{1}}(r) = \overline{\phi}$, which is just the standard (unweighted) manifold average. ${}^*\tilde{G}_g^{\mathbf{1}\phi}(r)$ can be seen as a weighted manifold average, but it has a lot more complicated weights, ${}^*\hat{\phi}(x;r) = \phi(x)\int_{S_x(r)} d^{n-1}y\,\sqrt{h(y)}\,\mathrm{Vol}\, S_x(r)^{-1}$.

[11] We include an example of 2D EDT instead of CDT, because for this theory the differences are larger, making it a clearer example.

[12] In [25] they propose that in the discrete theory two-point function $G_{N_2}^{\mathbf{1}\phi}(r)$ shows the behaviour

$$G_{N_2}^{\mathbf{1}\phi}(r) = \langle\overline{\phi}\rangle\, G_{N_2}^{\mathbf{11}}(r+\delta),$$

for some shift δ. This does indeed appear to be the case for our measurements of the vertex degree c and the average sphere distance $\bar{d}(\delta)$ if the correlation distance r is larger than the coarse-graining region of the ASD. So one can also use these shifted $G_g^{\mathbf{11}}(r+\delta)$ two-point functions for the normalization and defining the connected two-point function, as is done in [25]. However, we observed no significant difference to the connected two-point functions of the quantities we measured. We will therefore not discuss this option in this thesis, but it is an interesting possibility to look at in other quantum-gravitational two-point functions.

which is the familiar expression for a connected two-point function.

Then, since $\tilde{G}_g^{\mathbf{1}\phi}(r) = \overline{\hat{\phi}(r)}$ is a (weighted) average of ϕ we might also consider defining the connected two-point function using $\tilde{G}_g^{\mathbf{1}\phi}(r)$ as a mean instead. This leads us to suggest a second unnormalized connected (integrated) two-point function, as first considered in the context of the quantum theory by [27] and later by [25, 26],

$$\mathcal{G}_{2,g}^{\phi_1\phi_2}(r) = \int d^n x\,\sqrt{g(x)} \int d^n y\,\sqrt{g(y)} \Big(\phi_1(x) - \tilde{G}_g^{\phi_1\mathbf{1}}(r)\Big)\Big(\phi_2(y) - \tilde{G}_g^{\mathbf{1}\phi_2}(r)\Big)\,\delta(d_g(x,y) - r), \tag{7.15}$$

where the mean used is now the r-dependent weighted manifold average $\tilde{G}_g^{\mathbf{1}\phi}(r) = \overline{\hat{\phi}(r)}$ as defined in (7.8). This connected two-point function can also be rewritten to yield

$$\begin{aligned}\mathcal{G}_{2,g}^{\phi_1\phi_2}(r) &= \int d^n x\,\sqrt{g(x)} \int d^n y\,\sqrt{g(y)} \Big(\phi_1(x) - \tilde{G}_g^{\mathbf{1}\phi_1}(r)\Big)\Big(\phi_2(y) - \tilde{G}_g^{\mathbf{1}\phi_2}(r)\Big)\,\delta(d_g(x,y) - r)\\ &= G_g^{\phi_1\phi_2}(r) - \tilde{G}_g^{\mathbf{1}\phi_1}(r)\,\tilde{G}_g^{\mathbf{1}\phi_2}(r)\,G_g^{\mathbf{11}}(r),\end{aligned} \tag{7.16}$$

which has only two terms, as some terms cancel with this weighted average, resulting in a simpler expression.

Applying the standard normalization of (7.3) yields

$$\tilde{\mathcal{G}}_{2,g}^{\phi_1\phi_2}(r) = \tilde{G}_g^{\phi_1\phi_2}(r) - \overline{\hat{\phi}_1(r)}\;\overline{\hat{\phi}_2(r)}. \tag{7.17}$$

Using the alternative asymmetric normalization of (7.7), where we use ${}^*\tilde{G}_g^{\phi_1\mathbf{1}}(r)$ and ${}^*\tilde{G}_g^{\mathbf{1}\phi_2}(r)$ as the means in (7.15) respectively, gives

$$\begin{aligned}{}^*\tilde{\mathcal{G}}_{2,g}^{\phi_1\phi_2}(r) &= \frac{1}{\mathrm{Vol}\,M} \int d^n x\,\sqrt{g(x)} \frac{1}{\mathrm{Vol}\,S_x(r)} \int d^n y\,\sqrt{g(y)}\\ &\qquad \Big(\phi_1(x) - {}^*\tilde{G}_g^{\phi_1\mathbf{1}}(r)\Big)\Big(\phi_2(y) - {}^*\tilde{G}_g^{\mathbf{1}\phi_2}(r)\Big)\,\delta(d_g(x,y) - r)\\ &= {}^*\tilde{G}_g^{\phi_1\phi_2}(r) - \overline{\phi}_1\;{}^*\tilde{G}_g^{\mathbf{1}\phi_2}(r).\end{aligned} \tag{7.18}$$

Comparing this result to (7.12), we see that the two definitions of the normalized connected two-point functions are in fact equivalent when using the asymmetric normalization (7.7).

To show how the connected two-point function definitions (7.9) and (7.15) are different we include an example of the ensemble average[7] of the connected two-point functions of the vertex degree in 2D EDT[11] in Fig. 7.3. From this figure we can see that the connected two-point functions quickly go to 0 for large r, indicating that there are no long-range two-point correlations. Moreover, we see that the two different definitions for the connected two-point function have different behaviour for small $r < 15$. The small r behaviour can be attributed to discretization effects [25], so the differences in the definitions of the connected two-point functions are also attributed to discretization effects. Since the large r behaviour shows no correlations for both definitions as we expect in two dimensions, this example gives us no reason to prefer either (7.9) or (7.15).

7.1.3 Discretization

Now we have definitions for the two-point function on a given manifold, our next task is to discretize these definitions for a triangulation, so they can be used for 2D CDT. Discretizing (7.1) for a given triangulation T we obtain the (integrated) two-point function[13]

$$G_T^{\phi_1\phi_2}(r) = \sum_{p,q\in T} \phi_1(p)\phi_2(q)\,\delta_{d_T(p,q),r}\,, \tag{7.19}$$

---

[13] We use the subscript T to denote a two-point function on a given triangulation T.

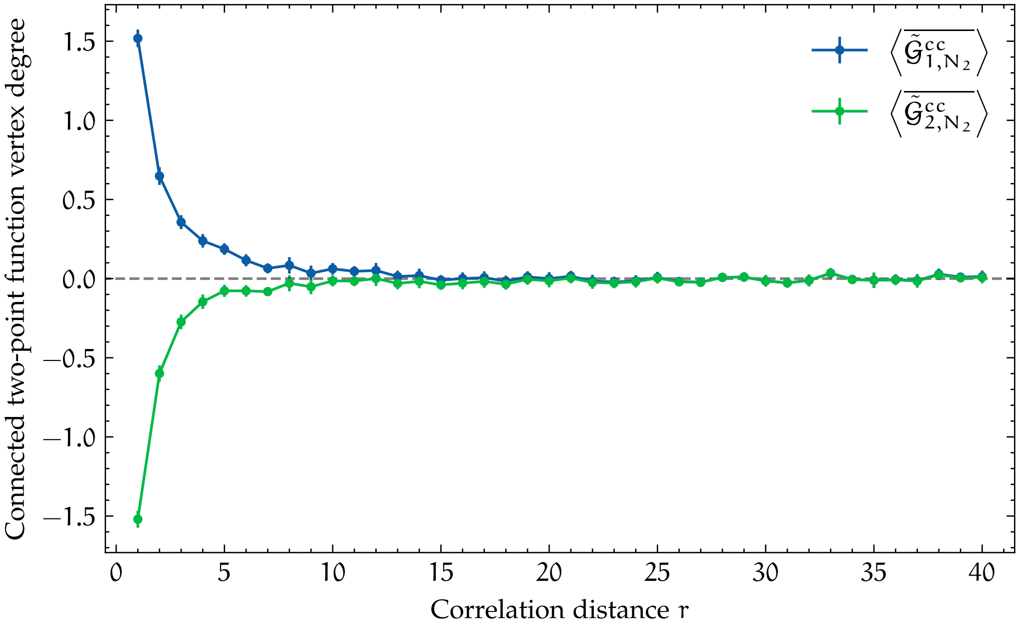

Figure 7.3: Ensemble average of the connected two-point functions $\tilde{\mathcal{G}}^{cc}_{i,N_2}(r)$, $i = 1, 2$, of the vertex degree c for 2D EDT with $N_2 = 300\,\mathrm{k}$.

where the sum is over the vertices of the triangulation[14] T, and the field quantities $\phi_1(p), \phi_2(q)$ live on the vertices. The selection of pairs is realized using the Kronecker delta, where $d(p, q)$ now denotes the geodesic distance on the vertex graph, which we take to be the link distance. Note that the local volume elements are 1 by our choice of discretization, such that $\operatorname{Vol} T = N_0$, the number of vertices in the triangulation. In this way we define the two-point function of field quantities that live on the vertex graph of the triangulation. One might also consider the two-point function of field quantities on the dual graph, in which case the geodesic distance becomes the graph distance in the dual graph and the sum is over triangles. For this thesis we only performed two-point function measurements on the vertex graph.

Using the same discretization, the normalized two-point function (7.3) becomes

$$\tilde{G}_T^{\phi_1\phi_2}(r) = \frac{G_T^{\phi_1\phi_2}(r)}{G_T^{\mathbf{11}}(r)} = \frac{\sum_{p,q} \phi_1(p)\phi_2(q)\,\delta_{d_T(p,q),r}}{\sum_{p,q} \delta_{d(p,q),r}}. \tag{7.20}$$

Eq. (7.7) becomes

$$^{*}\tilde{G}_T^{\phi_1\phi_2}(r) = \frac{1}{\operatorname{Vol} T} \sum_{p\in T} \frac{1}{\operatorname{Vol} S_p(r)} \sum_{q\in S_p(r)} \phi_1(p)\phi_2(q)\,\delta_{d(p,q),r}, \tag{7.21}$$

where the geodesic sphere is given by the set $S_p(r) = \{q \in T \mid d(p, q) = r\}$, and the local volume element on the sphere is also 1, such that $\operatorname{Vol} S_x(r)$ is the number of vertices in the sphere.

Finally, the connected two-point functions (7.9) and (7.15) become

$$\mathcal{G}_{1,T}^{\phi_1\phi_2}(r) = \sum_{p,q} \left(\phi_1(p) - \overline{\phi_1}\right)\left(\phi_2(q) - \overline{\phi_2}\right) \delta_{d(p,q),r}\,, \tag{7.22}$$

and

$$\mathcal{G}_{2,T}^{\phi_1\phi_2}(r) = \sum_{p,q} \left(\phi_1(p) - \tilde{G}_T^{\phi_1\mathbf{1}}(r)\right)\left(\phi_2(q) - \tilde{G}_T^{\phi_1\mathbf{1}}(r)\right) \delta_{d(p,q),r}\,. \tag{7.23}$$

---

[14] Note that we also use T to denote the set of vertices. It should be clear from context if the triangulation or its vertices are meant.

The manifold average $\overline{\phi}$ is given by

$$\overline{\phi} := \frac{1}{\mathrm{Vol}\,T} \sum_{p \in T} \phi(p),$$

in parallel to the continuum.

7.1.4 Point-pair sampling

Now that we have discrete definitions for the two-point functions, we can in principle measure them on the triangulations obtained from the 2D CDT Monte Carlo simulation. However, if the field observable ϕ of interest is computationally expensive to compute – like is the case for average sphere distance – it may be useful to approximate the point-pair sum by a sampling. This is analogous to approximating the manifold average by taking the sample average of a limited number of points. For sampling single points, one simply defines uniform sampling to be the sampling such that the selection probability of a given point is proportional to the local volume element, as this will give the same result as the manifold average for large samples. However, for sampling point pairs it is not immediately evident what uniform sampling means.

Coming from the delta-restricted double sum of (7.19) it seems natural for a given triangulation to consider the set of all pairs of points separated by distance r

$$\Pi_T(r) := \Big\{(p,q) \mid p,q \in T,\ d_T(p,q) = r\Big\}, \tag{7.24}$$

where it is important to note that (p,q) is an *ordered* pair. This is chosen, since (7.19) also sums over ordered pairs, but since both orderings appear once in the sum the total is still symmetric. Note that in our discretization the number of elements[15] in the set

$$\big|\Pi_T(r)\big| = G_T^{\mathbf{11}}(r) = \mathrm{Vol}\,T\,\overline{\mathrm{Vol}\,S(r)} \quad \text{and} \quad \Big|\bigcup_{r \geqslant 0} \Pi_T(r)\Big| = \big|T\big|^2 = \mathrm{Vol}(T)^2.$$

We can uniformly sample from $\Pi_T(r)$ by selecting each ordered pair with equal probability, i.e. with sampling probability

$$\mathcal{P}_T^0(p,q;r) = \frac{1}{\big|\Pi_T(r)\big|} = \frac{1}{\mathrm{Vol}\,T\,\overline{\mathrm{Vol}\,S(r)}}, \quad \text{such that} \sum_{(p,q)} \mathcal{P}_T^0(p,q;r) = 1, \tag{7.25}$$

where $(p,q) \in \Pi_T(r)$. The expectation value of $\phi_1(p)\phi_2(q)$ under this sampling probability $\mathcal{P}^0$ is then found to be

$$\begin{aligned}
\mathbf{E}_{\mathcal{P}^0}\big[\phi_1\phi_2(r)\big] &:= \sum_{(p,q)\in\Pi_T(r)} \mathcal{P}^0(p,q;r)\,\phi_1(p)\phi_2(q) \\
&= \frac{1}{\big|\Pi_T(r)\big|} \sum_{(p,q)} \phi_1(p)\phi_2(q) \\
&= \frac{1}{G_T^{\mathbf{11}}(r)} \sum_{p,q} \phi_1(p)\phi_2(q)\,\delta_{d_T(p,q),r} = \tilde{G}_T^{\phi_1\phi_2}(r).
\end{aligned} \tag{7.26}$$

We find that this sampling $\mathcal{P}^0$ reproduces the integrated two-point function in the standard normalization form (7.20).

---

[15] We use $|\ldots|$ to denote the cardinality or number of elements in a set.

However, numerically realizing this uniform $\mathcal{P}^0$ sampling is computationally expensive. We could identify $\Pi_T(r)$ for all required r, and then sample uniformly from this list, as per the definition of the sampling. This identification of all point pairs is computationally expensive as it requires $\mathrm{Vol}\,T$ breadth-first searches up to the maximum required r. This is especially inefficient if only a small sample is necessary. In this case, we could also use rejection sampling. This means we sample both points p and q uniformly from T and reject them if $d(p,q) \neq r$. In general, this has a small acceptance rate of $\overline{\mathrm{Vol}\,S(r)}/\,\mathrm{Vol}\,T$, and requires a breadth-first search for each (p,q) pair to check their separation distance.

An alternative sampling of point pairs is to first sample one of the points and then sample the second point from the sphere around the first, more accurately:

1. Uniformly sample a *first point* p from T;
2. Identify the geodesic sphere $S_p(r)$;
3. Uniformly sample a *second point* q from $S_p(r)$.

This sampling only requires a single breadth-first search for every point pair and has no rejections, making it a lot less computationally expensive than the two previously suggested methods. It seems that in previous papers [26, 27] this sampling is used instead of the uniform sampling, although we do not know this as the specific computational method is not explicitly stated. However, this method does not sample uniformly from $\Pi_T(r)$, but has the sampling probability

$$\mathcal{P}'_T(p,q;r) = \frac{1}{|T|\,|S_p(r)|} = \frac{1}{\mathrm{Vol}\,T\ \mathrm{Vol}\,S_p(r)}, \quad \text{such that} \sum_{(p,q)} \mathcal{P}'_T(p,q;r) = 1, \tag{7.27}$$

where $(p,q) \in \Pi_T(r)$; hence $\mathcal{P}' \neq \mathcal{P}^0$. Important to note is that the sampling $\mathcal{P}'_T(p,q;r)$ is now *asymmetric* in p and q, stemming from the fact that we consider the point pairs to be *ordered*. Using the sampling procedure $\mathcal{P}'$, the expectation value of $\phi_1\phi_2$ becomes

$$\begin{aligned}
\mathbb{E}_{\mathcal{P}'}\big[\phi_1\phi_2(r)\big] &:= \sum_{(p,q)} \mathcal{P}'(p,q;r)\, \phi_1(p)\phi_2(q) \\
&= \frac{1}{|T|} \sum_{(p,q)} \frac{1}{|S_p(r)|}\, \phi_1(p)\phi_2(q) \\
&= \frac{1}{\mathrm{Vol}\,T} \sum_p \frac{1}{\mathrm{Vol}\,S_p(r)} \sum_q \phi_1(p)\phi_2(q) = {}^*\tilde{G}_T^{\phi_1\phi_2}(r).
\end{aligned} \tag{7.28}$$

We see that sampling in this way reproduces the integrated two-point function with an alternative normalization (7.21). Thus, these different sampling methods are in general not equivalent as they estimate two-point functions with different normalizations, which themselves are non-equivalent as discussed in section 7.1.1.

Nevertheless, if one desires the standard normalization (7.20) but prefers sampling with $\mathcal{P}'$, one can still obtain this by weighting the samples. That is, we can compute a weighted expectation value instead of (7.28) to obtain the standard normalization, namely

$$\begin{aligned}
\frac{\mathbb{E}_{\mathcal{P}'}\big[(\mathrm{Vol}\,S(r)\phi_1)\phi_2(r)\big]}{\mathbb{E}_{\mathcal{P}'}\big[\mathrm{Vol}\,S(r)\big]} &:= \frac{\sum_{(p,q)} \mathcal{P}'(p,q;r)\ \mathrm{Vol}\,S_p(r)\phi_1(p)\phi_2(q)}{\sum_{(p,q)} \mathcal{P}'(p,q;r)\ \mathrm{Vol}\,S_p(r)} \\
&= \frac{\sum_{(p,q)} \phi_1(p)\phi_2(q)}{\sum_{(p,q)} \mathbf{1}} \\
&= \frac{1}{G_T^{\mathbf{11}}(r)} \sum_{p,q} \phi_1(p)\phi_2(q)\, \delta_{d_T(p,q),r} = \tilde{G}_T^{\phi_1\phi_2}(r),
\end{aligned} \tag{7.29}$$

where the $\mathrm{Vol}\, S(r)$ is with respect to the first sampled point. For the construction of the sampling the sphere $S_p(r)$ has to be determined in any case, so determining $\mathrm{Vol}\, S(r)$ has no additional computational cost.

To check the relation between the different samplings, we have measured the ensemble average of the two-point function for the vertex degree using different methods for 2D CDT. We have performed the full sum over all point pairs, directly following (7.20), and we have estimated the sum using the two different samplings methods (7.26), (7.28). The results of all these measurements are displayed in Fig. 7.4, where we also show the result of the weighted expectation value of the $\mathcal{P}'$ sampling (7.29). From the results it is evident that the uniform sampling (7.26) and the weighted alternative sampling (7.29) indeed yield the same result within statistical error as performing the full sum (7.20) as expected. We also see that the alternative sampling (7.28) in itself produces a different result, which corresponds to the alternative normalization (7.21).

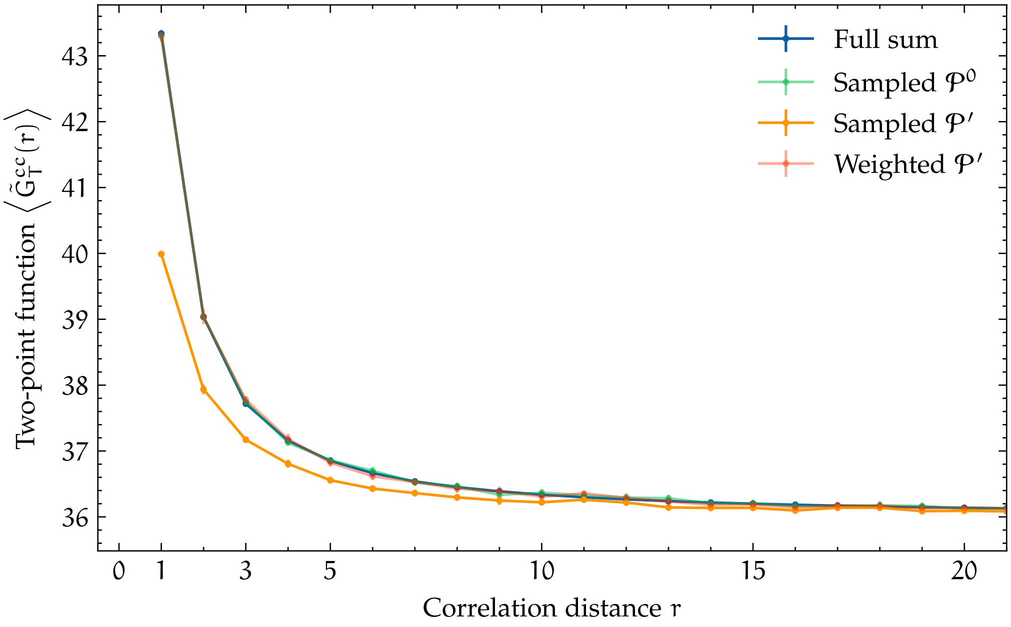

Figure 7.4: Comparison of different sampling methods and the full sum for the two-point function of vertex degree c: $\phi_1 = \phi_2 = c$. Results from ensemble averages of measurements of triangulations with $N_2 = 200\text{k}$ and $\tau = 179$. *Full sum* directly computes (7.20), the sampled results use their respective samplings, and *Weighted* estimates (7.29). It may not be completely evident from the figure, but all curves except *Sampled* $\mathcal{P}'$ lie on top of one another. The error bars give 95% confidence intervals.

7.2 Quantum two-point functions

In the previous section we have presented several diffeomorphism-invariant definitions of a two-point function. The two-point functions are valid observables, which we can measure in our quantum theory of causal dynamical triangulation. So we can define two-point functions of our quantum theory as ensemble averages of the two-point function observables we defined in the previous section. However, there are different ways in which the ensemble average can be applied, which is what we will discuss in this section.

For this thesis we consider the constant-volume[16] ensemble $\mathfrak{M}_V$ – this is discussed for the discrete theory in section 3.2. We define the (unnormalized) two-point function for quantum gravity as

$$G_V^{\phi_1\phi_2}(r) = \left\langle G_g^{\phi_1\phi_2}(r)\right\rangle_V = \frac{1}{Z_V}\int_{\mathfrak{M}_V}\mathcal{D}[g]\, G_g^{\phi_1\phi_2}(r), \tag{7.30}$$

where the subscript V denotes that the ensemble average is taken over the constant-volume ensemble, and Z_V is the partition function of this ensemble. We only consider ensemble averages over the constant-volume ensemble in the rest of this chapter, so we drop the subscript V in the following expressions to avoid notational clutter. We have two unique definitions of the normalized two-point function. The most straightforward one is the ensemble average of the normalized two-point function of a single geometry $\tilde{G}_g^{\phi_1\phi_2}$,

$$\tilde{G}_V^{\phi_1\phi_2}(r) = \left\langle \tilde{G}_g^{\phi_1\phi_2}(r)\right\rangle = \frac{1}{Z_V}\int_{\mathfrak{M}_V}\mathcal{D}[g]\,\frac{G_g^{\phi_1\phi_2}(r)}{G_g^{\mathbf{11}}(r)}, \tag{7.31}$$

which is the normalization that has been used in the previously shown figures. However, one might alternatively consider

$$'\tilde{G}_V^{\phi_1\phi_2}(r) = \frac{\left\langle G_g^{\phi_1\phi_2}(r)\right\rangle}{\left\langle G_g^{\mathbf{11}}(r)\right\rangle} = \frac{\displaystyle\int_{\mathcal{M}_V}\mathcal{D}[g]\, G_g^{\phi_1\phi_2}(r)}{\displaystyle\int_{\mathcal{M}_V}\mathcal{D}[g]\, G_g^{\mathbf{11}}(r)}. \tag{7.32}$$

These definitions are not identical as $G_g^{\mathbf{11}}(r) = \mathrm{Vol}\,\mathcal{M}\overline{\mathrm{Vol}\,S(r)} = V\ \mathrm{Vol}\,\overline{S(r)}$, and $\overline{\mathrm{Vol}\,S(r)}$ is not constant as a function of g.

The difference between these definitions depends on the correlation between $G_g^{\phi_1\phi_2}(r)$ and $\overline{\mathrm{Vol}\,S(r)}$ as a function of g. In 2D CDT we observe (see Fig. C.1) that $\sigma_{\mathrm{Vol}\,S(r)}$, the deviation of $\mathrm{Vol}\,S_p(r)$, given by

$$\sigma^2_{\mathrm{Vol}\,S(r)} := \left\langle \overline{\mathrm{Vol}\,S_p(r)^2}\right\rangle_{N_2} - \left\langle \overline{\mathrm{Vol}\,S(r)}\right\rangle_{N_2}^2, \tag{7.33}$$

is independent of the volume N_2 for r smaller than the effective linear size of the triangulation. We assume interchangeability between the manifold and ensemble average, in the sense that for increasing volume the ensemble becomes dominated by triangulations that have $\overline{\mathrm{Vol}\,S(r)} = \left\langle \overline{\mathrm{Vol}\,S_r}\right\rangle$. In this case, $\sigma_{\overline{\mathrm{Vol}\,S(r)}}$, the deviation of the manifold average of the sphere volume $\overline{\mathrm{Vol}\,S(r)}$, can be expected to decrease with increasing volume V (which is what we observe (C.2)). In the infinite-volume limit we are interested in, the deviation of $\overline{\mathrm{Vol}\,S(r)}$ is expected to go to zero, and the different ensemble averages (7.31) and (7.32) will be equivalent for r smaller than the effective linear size. Moreover, in measurements of the normalized two-point function $\tilde{G}_{N_2}^{cc}(r)$ for vertex degree c and $\tilde{G}_{N_2}^{\bar{d}\bar{d}}(r)$ for the average sphere distance $\bar{d}$ in 2D CDT and EDT, we find that the differences between the normalizations (7.31) and (7.32) are smaller than our statistical accuracy. Other authors have noted [27] that for their measurements of the Regge curvature two-point function in 4D EDT the difference is also negligible, using a similar argument. We conclude that for the two-point function we measure for this thesis there is no significant difference between (7.31) and (7.32) for r smaller than the linear size of the system. Since this is what we are interested in, we will not differentiate between these forms of normalization, and use (7.31) for the rest of this thesis.

Next, we consider the non-uniqueness of the connected (unnormalized) two-point functions. The most straightforward definitions for the connected two-point function for quantum gravity are the ensemble averages of (7.9) and (7.15), giving

$$\mathcal{G}_{1,V}^{\phi_1\phi_2}(r) = \left\langle \mathcal{G}_{1,g}^{\phi_1\phi_2}(r)\right\rangle \tag{7.34}$$

---

[16] We denote the constant volume in continuum by V and in the discrete 2D CDT theory with the two-volume N_2.

and

$$\mathcal{G}^{\phi_1\phi_2}_{2,V}(r) = \left\langle \mathcal{G}^{\phi_1\phi_2}_{2,g}(r) \right\rangle . \tag{7.35}$$

Recall that these two different definitions compute the two-point function of the deviation from different means. The connected two-point function $\mathcal{G}^{\phi_1\phi_2}_{1,V}$ uses the manifold average $\overline{\phi}$ as the mean, and $\mathcal{G}^{\phi_1\phi_2}_{2,V}$ uses the normalized **1**-ϕ two-point function $\overline{\hat{\phi}(r)}$ as the mean. In the full quantum gravity setting, we can also consider taking an ensemble-averaged quantity as the mean, specifically $\langle\overline{\phi}\rangle$ and $\left\langle\overline{\hat{\phi}(r)}\right\rangle$. Using these ensemble-averaged means, the connected (unnormalized) two-point functions for quantum gravity can be defined as[17]

$$\mathcal{G}^{\phi_1\phi_2}_{q1,V}(r) = \left\langle \int d^n x\, \sqrt{g(x)} \int_{S_x(r)} d^{n-1}y\, \sqrt{h(y)} \Big(\phi_1(x) - \langle\overline{\phi}_1\rangle\Big)\Big(\phi_2(y) - \langle\overline{\phi}_2\rangle\Big) \right\rangle , \tag{7.36}$$

and

$$\mathcal{G}^{\phi_1\phi_2}_{q2,V}(r) = \left\langle \int d^n x\, \sqrt{g(x)} \int_{S_x(r)} d^{n-1}y\, \sqrt{h(y)} \Big(\phi_1(x) - \left\langle \tilde{G}^{\phi_1 \mathbf{1}}_{1,g}(r)\right\rangle\Big)\Big(\phi_2(y) - \left\langle \tilde{G}^{\mathbf{1}\phi_2}_{1,g}(r)\right\rangle\Big) \right\rangle . \tag{7.37}$$

These definitions of the connected two-point function can be interpreted as correlations of quantum fluctuations, since they are two-point functions of the deviation from a quantum average. Writing out these definitions of the connected two-point functions, we obtain

$$\tilde{\mathcal{G}}^{\phi_1\phi_2}_{1,V}(r) = \langle \tilde{G}^{\phi_1\phi_2}_{g}(r)\rangle - \left\langle \overline{\hat{\phi}_1(r)}\,\overline{\phi}_2 \right\rangle - \left\langle \overline{\phi}_1 \overline{\hat{\phi}_2(r)} \right\rangle + \langle \overline{\phi}_1 \overline{\phi}_2 \rangle , \tag{7.38}$$

$$\tilde{\mathcal{G}}^{\phi_1\phi_2}_{q1,V}(r) = \langle \tilde{G}^{\phi_1\phi_2}_{g}(r)\rangle - \left\langle \overline{\hat{\phi}_1(r)} \right\rangle \langle \overline{\phi}_2 \rangle - \langle \overline{\phi}_1 \rangle \left\langle \overline{\hat{\phi}_2(r)} \right\rangle + \langle \overline{\phi}_1 \rangle \langle \overline{\phi}_2 \rangle , \tag{7.39}$$

and

$$\tilde{\mathcal{G}}^{\phi_1\phi_2}_{2,V}(r) = \langle \tilde{G}^{\phi_1\phi_2}_{g}(r)\rangle - \left\langle \overline{\hat{\phi}_1(r)}\; \overline{\hat{\phi}_2(r)} \right\rangle , \tag{7.40}$$

$$\tilde{\mathcal{G}}^{\phi_1\phi_2}_{q2,V}(r) = \langle \tilde{G}^{\phi_1\phi_2}_{g}(r)\rangle - \left\langle \overline{\hat{\phi}_1(r)} \right\rangle \left\langle \overline{\hat{\phi}_2(r)} \right\rangle . \tag{7.41}$$

Hence, we find that the difference between using the ensemble average and manifold average as reference is given by the correlation of the different combinations of the averaged quantities $\overline{\phi}$ and $\overline{\hat{\phi}(r)}$. These correlations are bounded[18] by the variance of the observables, for example,

$$\Big(\langle \overline{\phi_1}\; \overline{\phi_2} \rangle - \langle \overline{\phi_1} \rangle \langle \overline{\phi_2} \rangle \Big)^2 \leqslant \Big(\left\langle \overline{\phi_1}^2 \right\rangle - \langle \overline{\phi_1} \rangle^2 \Big) \Big(\left\langle \overline{\phi_2}^2 \right\rangle - \langle \overline{\phi_2} \rangle^2 \Big) \coloneqq \sigma^2_{\overline{\phi_1}} \sigma^2_{\overline{\phi_2}} . \tag{7.42}$$

This implies the upper bounds on the differences between the connected two-point functions,

$$\left| \tilde{\mathcal{G}}^{\phi_1\phi_2}_{q1,V}(r) - \tilde{\mathcal{G}}^{\phi_1\phi_2}_{1,V}(r) \right| \leqslant \sigma_{\overline{\hat{\phi}_1(r)}}\, \sigma_{\overline{\phi_2}} + \sigma_{\overline{\phi_1}}\, \sigma_{\overline{\hat{\phi}_2(r)}} + \sigma_{\overline{\phi_1}}\, \sigma_{\overline{\phi_2}} \tag{7.43}$$

$$\left| \tilde{\mathcal{G}}^{\phi_1\phi_2}_{q2,V}(r) - \tilde{\mathcal{G}}^{\phi_1\phi_2}_{2,V}(r) \right| \leqslant \sigma_{\overline{\hat{\phi}_1(r)}}\, \sigma_{\overline{\hat{\phi}_2(r)}} . \tag{7.44}$$

These differences only contain deviations of manifold-averaged quantities like $\sigma_{\overline{\phi_1}}$. Like we argued for $\sigma_{\overline{\mathrm{Vol}\,S(r)}}$, we expect $\sigma_{\overline{\phi}}$ to go to 0 in the infinite-volume limit. This is because the manifold average is taken over an increasingly larger volume, causing the deviation of the manifold average to go down. Here we again need to assume that for increasing volume the manifold average of almost all triangulations approaches the ensemble average. Also, the deviation will not vanish if the quantity ϕ grows too quickly with increasing volume, but this does not appear to be the case for the vertex degree c and average sphere distance $\bar{d}(\delta)$ we consider in this thesis. Thus, for 2D CDT and the quantities we consider, we expect the difference between the different definitions for the connected two-point functions (7.34) and (7.35), and between (7.36) and (7.37) to be negligible, if the volume N_2 is large enough and finite-size effects are negligible. Moreover, test measurements of the connected two-point functions of the vertex degree c and average sphere distance $\bar{d}(\delta)$ in 2D CDT showed no differences within our statistical accuracy.

---

[17] Note that we use a subscript q1 and q2 to denote the connected two-point functions with ensemble-averaged means.

[18] By means of the Cauchy-Schwarz inequality.

In conclusion, interchanging the manifold averaging and ensemble averaging in a constant volume does not seem to make a significant difference to the connected two-point functions, at least for the vertex degree c and average sphere distance $\bar{d}$. It seems reasonable that for large enough system sizes the atypical parts of manifolds are 'washed out' in the manifold averaging, such that the deviations from the ensemble average vanish. We will not differentiate between the definitions of the connected two-point functions with respect to the two different means, and will only work with the connected two-point functions (7.36) and (7.37) that are defined with respect to the ensemble-averaged means. However, it would be interesting to investigate the differences further and investigate our assumption on the interchangeability of the manifold and ensemble average in greater detail.

8. QRC Correlations

Now that we have definitions for two-point functions in quantum gravity we can try and measure them in 2D CDT for the quantum Ricci curvature (QRC) introduced in chapter 5. For the two-point functions, we will use the normalization as defined by (7.31). We consider both definitions (7.36) and (7.37) of the connected two-point function. We make use of the uniform sampling as given by the sampling probability (7.25), estimating the point pair sums of the two-point functions by (7.26). We will estimate the fixed-volume ensemble average (3.4) using the Markov chain Monte Carlo methods as discussed in section 3.3.

8.1 Average sphere distance as curvature

To measure curvature two-point functions we will analyse the two-point functions of the average sphere distance, or more accurately the curvature profile $\bar{d}(\delta)/\delta$. In order to compute these two-point functions we need to associate an ASD value to every point of the triangulation. To accurately represent the coarse-graining regions of the triangulation, we want this association to be a one-to-one map, i.e. each point should be mapped to a unique coarse-graining region. We will only consider ASD for $\epsilon = 0$, i.e. the ASD of two fully overlapping spheres. In this case, we choose the one-to-one mapping of the coarse-graining region $S_p(\delta)$ with the origin point p. We use the field quantity: $p \mapsto d_p(\delta)/\delta$, for some fixed δ. If one is interested in measuring curvature two-point functions with directional information one can consider ASD for $\epsilon = \delta$. However, making an association between the coarse-graining region given by the two δ-separated spheres is more challenging, the details of which are described in section B.4.

As discussed in section 5, the average sphere distance is related to the quantum Ricci scalar $K(p;\delta)$ according to (5.5),

$$\bar{d}_p(\delta)/\delta = c'_q\big(1 - K(p;\delta)\big),$$

where c'_q is a prefactor, which is known to be point-independent on a smooth Riemannian manifold. Assuming c'_q is constant in 2D CDT one can interpret the two-point functions[1] $\tilde{G}^{\bar{d}\bar{d}}_{N_2}(r)/\delta^2$ of $\bar{d}_p(\delta)/\delta$ as two-point functions of $K(p;\delta)$, as they are related by

$$\begin{aligned}
\frac{\tilde{G}^{\bar{d}\bar{d}}_{N_2}(r)}{\delta^2} &= \left\langle \frac{1}{\mathrm{Vol}\,T\,\overline{\mathrm{Vol}\,S(r)}} \sum_{p\in T}\sum_{q\in T} \frac{\bar{d}_p(\delta)}{\delta}\frac{\bar{d}_q(\delta)}{\delta}\,\delta_{d(p,q),r} \right\rangle_{N_2} \\
&= \left\langle \frac{c'^2_q}{\mathrm{Vol}\,T\,\overline{\mathrm{Vol}\,S(r)}} \sum_{p\in T}\sum_{q\in T} (1 - K(p;\delta))(1 - K(q;\delta))\,\delta_{d(p,q),r} \right\rangle_{N_2} \\
&= c'^2_q\big(1 - 2\tilde{G}^{1K}_{N_2}(r) + \tilde{G}^{KK}_{N_2}(r)\big),
\end{aligned} \tag{8.1}$$

and for the connected two-point functions this becomes

$$\frac{\tilde{\mathcal{G}}^{\bar{d}\bar{d}}_{N_2}(r)}{\delta^2} = c'^2_q\tilde{\mathcal{G}}^{KK}_{N_2}(r). \tag{8.2}$$

Assuming c'_q is constant we can interpret the two-point functions of ASD as scaled two-point functions of QRC. However, note that in 2D CDT c'_q can be point-dependent because of the non-uniform nature of the lattice. It is non-trivial to determine c'_q for a given $d_p(\delta)/\delta$. So we are not able to extract $K(p;\delta)$ for each $\bar{d}_p(\delta)$ measurement separately. Thus, we will simply present the two-point functions of ASD as they are. These are strongly related to the two-point functions of QRC, but keep in mind that they cannot directly be interpreted as the two-point functions of QRC, because they may be mixed with the two-point functions of c'_q.

---

[1] To avoid notational clutter we will denote the two-point functions of $\bar{d}_p(\delta)/\delta$ by the quotient $G^{\bar{d}\bar{d}}(r)/\delta^2$, which is algebraically equivalent as δ is constant.

8.2 Results

First, we measure the normalized two-point function $\tilde{G}^{\bar{d}\bar{d}}_{N_2}(r)$ (the discretized version of (7.31)) of the curvature profile $\bar{d}_p(\delta)/\delta$ with fully overlapping spheres ($\epsilon = 0$) for 2D CDT. We have performed these measurements at fixed volumes $N_2 = 100\text{k}$, 200k, and 300k and for fixed coarse-graining scales δ up to 18. The ensemble average is estimated using 150 configurations sampled using the Markov chain Monte Carlo simulation. In each triangulation, the two-point function is estimated using 5000 uniform point-pair samples (7.26). All statistical error bars presented in the following figures are 95%-confidence intervals based on the sampling[2]. The resulting normalized two-point function $\tilde{G}^{\bar{d}\bar{d}}_{N_2}(r)/\delta^2$ is shown on the left in Fig. 8.1. On the right of the same Fig. 8.1 we show the ensemble average of the r-dependent weighted average, i.e. the (local-volume, ASD) two-point function $\tilde{G}^{1\bar{d}}_{N_2}(r)/\delta = \left\langle \hat{\bar{d}}(\delta;r) \right\rangle$ (7.13). Based on the results of $\tilde{G}^{1\bar{d}}_{N_2}(r)/\delta$ we can see that for ASD we find that $\overline{\hat{\bar{d}}(\delta;r)} \neq \overline{\bar{d}(\delta)}$, reflecting the irregular geometries of CDT. It is also clear that $\overline{\hat{\bar{d}}(\delta;r)}$ is considerably larger than $\bar{d}$ around $r = \delta$, indicating that spheres with larger volume $\mathrm{Vol}\, S_p(r)$ have larger $\bar{d}(S_p(r), S_p(r))$. Finally, the shape of $\tilde{G}^{\bar{d}\bar{d}}_{N_2}(r)/\delta^2$ can be seen to be very similar to $\tilde{G}^{1\bar{d}}_{N_2}(r)/\delta$. In fact, $\left(\tilde{G}^{1\bar{d}}_{N_2}(r)/\delta\right)^2$ is almost identical to $\tilde{G}^{\bar{d}\bar{d}}_{N_2}(r)/\delta^2$, reflecting the fact that the

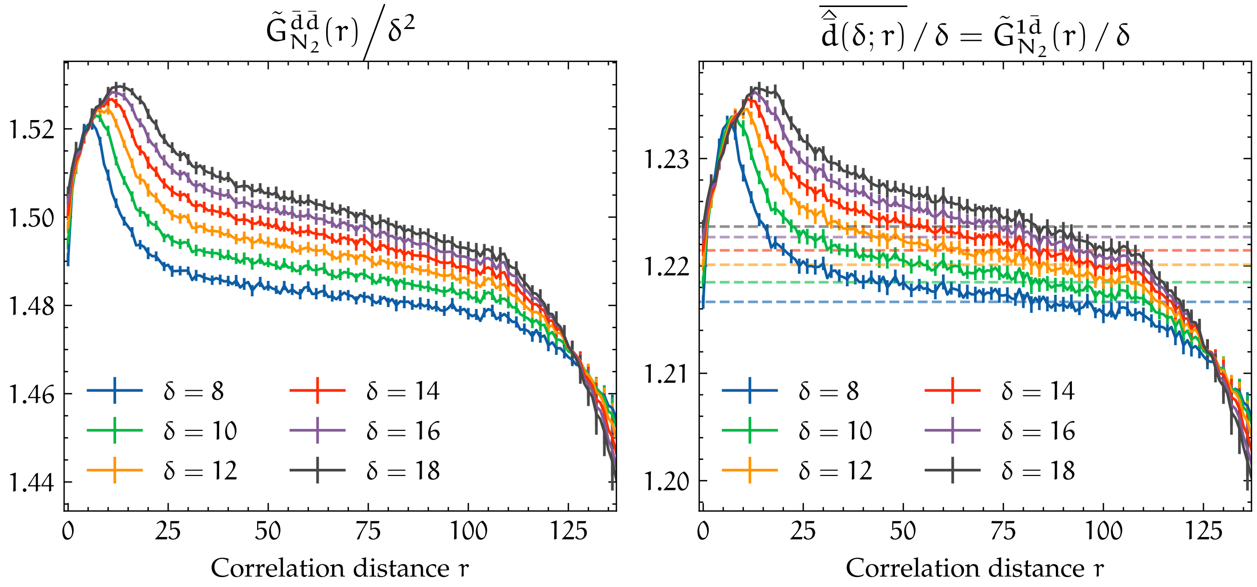

Figure 8.1: Left: the normalized two-point function $\tilde{G}^{\bar{d}\bar{d}}_{N_2}(r)$ for the average sphere distance $\bar{d}(\delta)/\delta$ (7.31). Right: the r-dependent mean of the average sphere distance $\frac{\left\langle \hat{\bar{d}}(\delta;r) \right\rangle}{\delta}$, i.e. $\tilde{G}^{1\bar{d}}_{N_2}(r)/\delta$, together with the standard triangulation average $\frac{\langle \bar{d} \rangle}{\delta}$. Both are measured for $\delta \in [8, 18]$ for CDT at fixed volume $N_2 = 300\text{k}$ and $\tau = 219$.

---

[2] Note that the different samples in each triangulation are not independent, so the error is only estimated based on the average of each triangulation, considering each triangulation to be independently sampled. This has been verified to be the same as computing the error using a batched bootstrapping method to account for any statistical correlation.

connected two-point function $\tilde{\mathcal{G}}^{\bar{d}\bar{d}}_{q2,N_2}(r)/\delta^2 = 0$ for most r, as we will show in a moment.

To make further interpretations of curvature correlations we will look at the connected correlators. In Fig. 8.2 we show the result of the normalized connected two-point function $\tilde{\mathcal{G}}^{\bar{d}\bar{d}}_{q1,N_2}(r)$ (that is the normalized and discretized version of (7.36)) of the ASD $\bar{d}$. On the right the same normalized connected two-point function is displayed, but it is rescaled with $\tilde{\mathcal{G}}^{\bar{d}\bar{d}}_{1,N_2}(r=0)/\delta^2$, which is precisely the variance of $\bar{d}/\delta$ over the triangulation. Additionally, the correlation distance r is rescaled with the coarse-graining scale δ, giving us an "additionally normalized" correlation function. This is done, such that we can interpret the shape without needing to account for the δ-dependence. From this result on the right of Fig. 8.2 we can clearly see that this rescaling removes all δ-dependence and perfectly overlaps the curves for different δ. From this we see that for small r the two-point function starts off positive, which makes sense as in this case the coarse-graining regions used to compute the ASD have a lot of overlap, causing the resulting ASDs to be (positively) correlated. If we are interested in physical correlations that are still present in the continuum limit we should only consider correlation distances $r \gg \delta$. Indeed, for $r > 2\delta$ where the coarse-graining regions given by geodesic spheres of radius δ no longer overlap, we see that the correlation is 0. This is precisely what we would expect for 2D quantum gravity, as a non-vanishing correlation would have an emergent physical length-scale associated with it, and we know that classically there are no propagating degrees of freedom. There is only a single length scale, which in our model is already fixed by the global size of the triangulation. So we expect no additional length scale to emerge. This is indeed what we see, the only length scale being δ which is put in by construction. Note that in the region around $r = \delta$ a negative correlation appears, which corresponds to the region where the spheres half overlap. We have been unable to give an explanation for this feature, which we would like to understand. However, as discussed this region is irrelevant from a continuum perspective, where we have $r \gg \delta$, so for this purpose it suffices to say this is simply a discretization feature of the coarse-graining observable. Furthermore, notice the deviation from 0 appearing for $r > 120$, which is when finite-size effects start to appear. We are interested in "local" curvature correlations, in the sense that we want to consider correlation distances $2r \ll d_{\text{eff}}$,

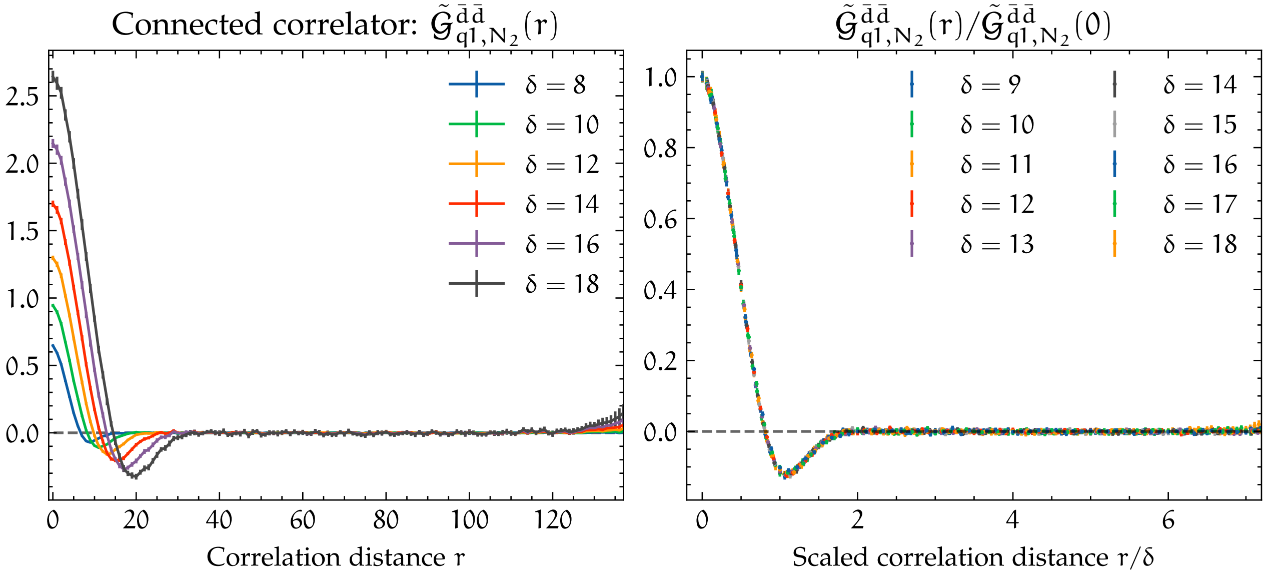

Figure 8.2: Left: normalized connected two-point function $\tilde{\mathcal{G}}^{\bar{d}\bar{d}}_{q1,N_2}(r)$ for average sphere distance $\bar{d}(\delta)$ using the subtraction prescription (7.36). Measured in 2D CDT with $\delta \in [8, 18]$ with $N_2 = 300\text{k}$ and $\tau = 219$. Right: the same connected two-point function but rescaled like $\tilde{\mathcal{G}}^{\bar{d}\bar{d}}_{q1,N_2}(r)/\tilde{\mathcal{G}}^{\bar{d}\bar{d}}_{q1,N_2}(0)$ against the rescaled correlation distance r/δ. This allows us to better compare the two-point correlation for different δ.

where d_{eff} is the effective diameter of the triangulation. For the analysis of topological effects on sphere volumes (see section 6.2) we used a lower bound of around $r_{\max} \approx 60$ for $N_2 = 300\text{k}$, which indicates that $d_{\text{eff}} \approx 120$. To be able to interpret the two-point function as reflecting the "local" geometry we should look no further than $r_{\max} = 60$. Thus, $r > 120$ is definitely subject to global topological effects. Note that we only present the results of $N_2 = 300\text{k}$ here; for the smaller volumes the same results are obtained, except for the finite-size effects starting for smaller r as expected.

Finally, we will consider the difference between the two different connected two-point functions (7.36) and (7.37). Specifically, we compare the normalized connected two-point functions $\tilde{\mathcal{G}}^{\bar{d}\bar{d}}_{q1,N_2}(r)$ and $\tilde{\mathcal{G}}^{\bar{d}\bar{d}}_{q2,N_2}(r)$, the results of which are shown in Fig. 8.3 for $\delta = 15$ (the result is very similar for other δ). From this result we see that in the region of interest ($r \in (30, 110)$) both correlators are 0 as expected. The only differences of $\tilde{\mathcal{G}}_2$ compared to $\tilde{\mathcal{G}}_1$ are a slightly smaller negative correlation around $r = \delta = 15$, and even less finite-size effects for $r > 110$. Based on these results in 2D CDT where the correlation is 0 we cannot meaningfully distinguish between the two definitions of the connected two-point function (7.36) and (7.37), and we cannot favour one or the other.

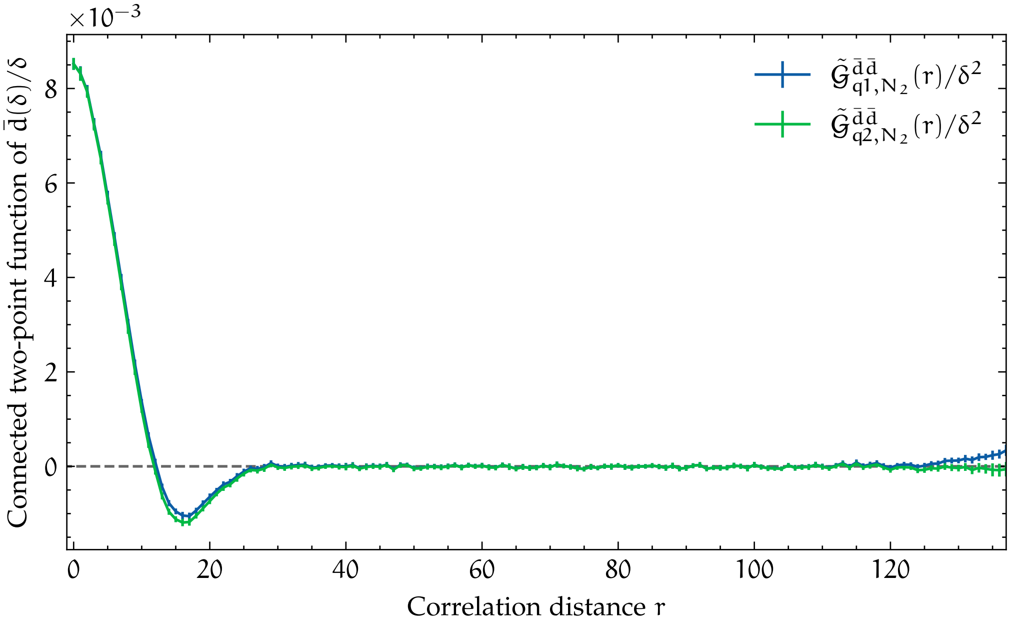

Figure 8.3: Comparison between the different definitions $\tilde{\mathcal{G}}^{\bar{d}\bar{d}}_{q1,N_2}(r)/\delta^2$ and $\tilde{\mathcal{G}}^{\bar{d}\bar{d}}_{q2,N_2}(r)/\delta^2$ of the connected two-point functions (7.22) and (7.23) for the curvature profile or normalized average sphere distance $\bar{d}(\delta)/\delta$ for $\delta = 15$.

To gain more insight in curvature two-point functions it would be interesting to analyse them in a model where there are propagating degrees of freedom and where we might expect nontrivial correlations to emerge, like the full theory of 4D CDT. This may give one a more "fine-grained" understanding of the behaviour of curvature in quantum gravity, to get a better idea of the geometry of the quantum spacetimes. And it may allow one to gain more insight in the differences between the different definitions of the connected two-point function.

Finally, we note that additional research is necessary to understand how strongly the correlations of the curvature profile $\bar{d}(\delta)/\delta$ are mixed with the correlation of the prefactor c'_q, as discussed in section 8.1. In other words, we do not yet understand how different the correlation of the quantum Ricci curvature (or scalar in our case) $K(p;\delta)$ is from the correlation of the curvature profile $\bar{d}_p(\delta)/\delta$. There is ongoing research [28] in defining alternative definitions of scalar curvature in a quantum gravity settings, which aim to avoid having to introduce an unknown prefactor like c'_q.

If such a definition of scalar curvature can successfully be found, this could provide a helpful tool in understanding the impact of the c'_q correlations. However, at this stage we do not know if this can be successfully done.

9. Conclusion

In this thesis we presented a numerical investigation of the behaviour of two-point functions in two-dimensional causal dynamical triangulations (2D CDT). To be able to perform numerical measurements we developed a numerical model based on Markov chain Monte Carlo methods to simulate 2D CDT. We should note that at the time of performing our measurements, we incorrectly implemented the simplicial manifold condition (see chapter 2). Our implementation allowed all spatial slices with length $l \geqslant 1$, which violates the simplicial manifold condition for $l \leqslant 2$. However, for the sizes of triangulations we used in our measurements the probability of creating a triangulation with short spatial slices that violates the simplicial manifold condition is close to 0. We conclude that the effect that the incorrect implemention of the simplicial manifold condition has on our results is negligible.

We measured the local Hausdorff dimension to be $d_H = 2.23 \pm 0.01$, which is significantly different from the theoretically expected $d_H = 2$. We argued that the method used, which is based on the small-radius behaviour of the geodesic sphere volume, is not well suited for the estimation of the Hausdorff dimension. However, we have not performed other measurements of the Hausdorff dimension as this is not the primary focus of this thesis. Additionally, we measured the spectral dimension to be $d_s = 2.013 \pm 0.007$, which is found to be consistent with the theoretically expected $d_s = 2$ and other numerical results.

In quantum gravity, the observables that are often considered are manifold averages of local field quantities, because observables need to be diffeomorphism-invariant. Two-point functions give us a way to get a more “fine-grained” look at the geometry of the dynamical triangulations, by expressing how the relation between two field quantities changes over distance. We discuss the several ambiguities in defining two-point functions. There are multiple ways to normalize the two-point function and multiple possible definitions for the connected two-point function. We also argued that one should be careful when estimating the average over point pairs using a sampling method, as the sample average of point pairs may not estimate what one expects.

Finally, we measured the two-point functions of the average sphere distance in 2D CDT. These can be interpreted as the two-point functions of the quantum Ricci curvature, with some caveats (see chapter 8). From the results of the connected two-point functions we conclude that there is no correlation between curvatures in 2D CDT, which aligns with our expectations of 2D gravity. For future research it would be interesting to further investigate the two-point functions of the quantum Ricci curvature in full 4D CDT, where we may expect to see non-trivial curvature correlations.

Acknowledgments

Firstly, I would like to thank my supervisor, Renate Loll, for the many long interesting discussions we have had. Her interest in my project and supervision during it were very motivating and greatly appreciated, and her thorough reading of my thesis was very helpful in finalizing it. I also want to thank Thijs Niestadt, Agustín Silva and Tom Gerstel for being great to work with and for discussing many aspects of my project with me. Finally, I would like to thank Timothy Budd for sparking my interest in dynamical triangulations with his wonderful course on Monte Carlo techniques.

A. Numerical implementation

For this thesis I have implemented a numerical model from scratch in the Rust[1] programming language. In doing so I came across a lot of difficulties, which required some thought to be implemented effectively. Some of the choices I made are discussed in this thesis, but most are not relevant to the presented research and thus left out. However, I think it can be very helpful to have a good reference if one needs to implement a numerical dynamical triangulations model oneself. So, I hope to provide such a reference implementation for 2D CDT.

My implementation is available via a GitLab repository at `https://gitlab.com/dynamical-triangulation/dyntri` as an open-source library/crate in the Rust programming language. As a library it provides all the functionality to perform simulations and measurements, which one can use in a binary application to set up the simulations in whatever configuration one would like. An example implementation of such a binary application, which was used to set up the measurements for this thesis is also provided along with this library. Moreover, I tried my best to make the library well-documented and its source code clearly written, such that my implementation is hopefully easy to understand to anyone who wants to see an example of numerical 2D CDT. If one wants to read our implementation of some part of the numerical model the easiest option is likely to use the documentation (as provided with the repository) to search for the relevant functions and data structures.

Besides simulating 2D CDT and performing measurements on the triangulation, the library also implements importing and exporting of graphs. This allows one to perform measurements of all the quantities presented in this thesis, like average sphere distance and two-point functions on any graph generated by external programs, for example, the vertex graphs of EDT. The library also implements some embeddings for 2D CDT triangulations, which can be used to make visualizations, like the one presented on the title page and all other triangulation visualizations in this thesis. Finally, just because I really enjoy looking at these visualizations, here is a bonus:

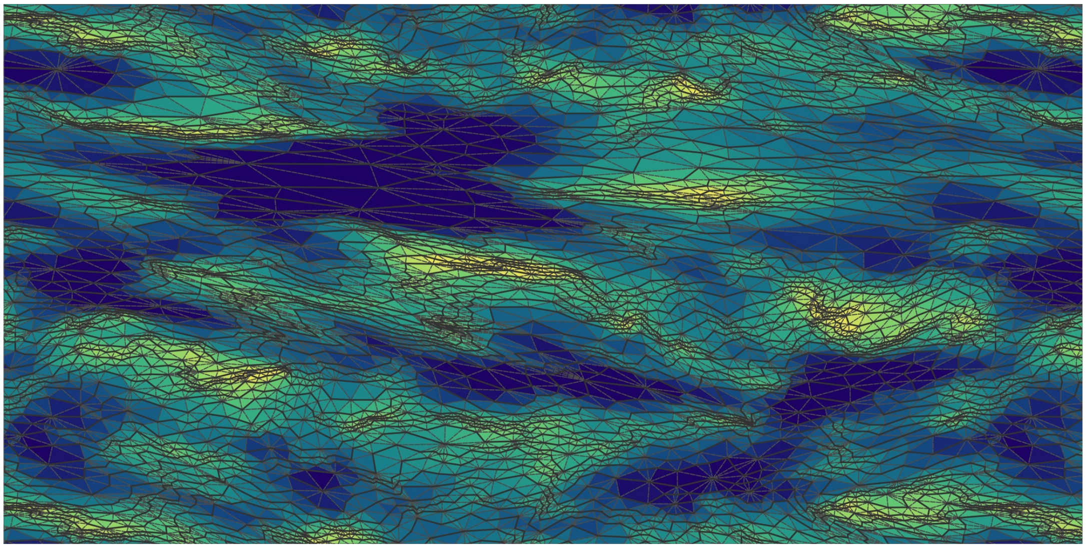

Figure A.1: A visualization of the average sphere distance on a single toroidal 2D CDT triangulation using a Tutte embedding. The triangulation is folded out and repeated; features can be seen to repeat around the edges of the image. Each triangle is coloured based on the average ASD $\bar{d}_p(\delta = 8)$ $(\epsilon = 0)$ of their vertices. Blue corresponds to high $\bar{d}$ and yellow to low $\bar{d}$.

---

[1] See `https://www.rust-lang.org/`

B. Additional material

This chapter contains sections discussing topics relevant to the main text, but not crucial for the main story. They are included here for the readers that are interested.

B.1 Average sphere distance derivation

We want to show that in a two-dimensional Riemannian manifold the small-δ expansion of the average sphere distance (ASD) $\bar{d}_x(\delta) = \bar{d}\big(S_x(\delta), S_x(\delta)\big)$ for the fully overlapping spheres $S_x(\delta)$ is given by

$$\frac{\bar{d}\big(S_x(\delta), S_x(\delta)\big)}{\delta} = \frac{4}{\pi} - \frac{R}{9\pi}\,\delta^2 + O(\delta^3) \approx 1.273 - 0.0354R\,\delta^2 + O\big(\delta^3\big).$$

For this we follow the derivation Nilas Klitgaard presents in his PhD thesis [29] for ASD where the spheres are separated with distance δ. In our case, where the spheres are fully overlapping, the situation is a lot simpler.

This derivation is performed in Riemann normal coordinates (RNC) [30]. As an expansion point for RNC we use x, the origin of the sphere $S_x(\delta)$, for which we wish to compute the average sphere distance. With this choice of origin and in RNC, $S_x(\delta)$ looks like a regular sphere in Euclidean space for sufficiently small δ. So, we can parameterize a point y on the sphere $y \in S_x(\delta)$ with an angle ϕ like

$$y(\phi) = \big(\delta\cos\phi, \delta\sin\phi\big). \tag{B.1}$$

The distance $L(x_i, x_j)$ between two points x_i and x_j in RNC is given by [30]

$$L^2_{x_i,x_j} = g_{ab}\,\Delta x^a_{ij}\,\Delta x^b_{ij} - \frac{1}{3}R_{abcd}x^a_i x^b_j x^c_i x^d_j + O\big(\delta^5\big) \tag{B.2}$$

where $\Delta x_{ij} = x_j - x_i$, and g_{ab} and R_{abcd} are the metric and Riemann tensor at x in RNC. The average sphere distance $\bar{d}$ can then be determined by calculating

$$\bar{d}(\delta) = \frac{1}{\mathrm{Vol}\,S_x(\delta)^2}\int_0^{2\pi}\int_0^{2\pi} d\phi_1\,\sqrt{h(\phi_1)}\,d\phi_2\,\sqrt{h(\phi_2)}\;L\big(y(\phi_1), y(\phi_2)\big), \tag{B.3}$$

where h is the determinant of the induced metric on $S_x(\delta)$.

To determine a local expansion of h_{ab}, we consider the infinitesimal distance between two points $y(\phi)$ and $y(\phi + d\phi)$ on the sphere, and obtain

$$L^2\big(y(\phi), y(\phi + d\phi)\big) = \delta^2\,d\phi^2 - \frac{1}{3}R_{1212}\delta^4 + O\big(\delta^5\big) = h_{\phi\phi} + O\big(\delta^5\big). \tag{B.4}$$

Note that in two-dimensions $R = 2\,R_{1212}$, where R is the Ricci scalar. We find that the measure $\sqrt{h}$ is given by

$$\sqrt{h} = \sqrt{h_{\phi\phi}} = \delta\sqrt{1 - \frac{1}{6}R\delta^2 + O(\delta^4)} = \delta\left(1 - \frac{1}{12}R\delta^2\right) + O\big(\delta^5\big).$$

With this measure we can compute the sphere volume

$$\mathrm{Vol}\,S_x(\delta) = \int_0^{2\pi} d\phi\,\sqrt{h} = 2\pi\delta\left(1 - \frac{1}{12}R\delta^2\right) + O\big(\delta^5\big). \tag{B.5}$$

We obtain the integral (B.3) for $\bar{d}$,

$$\begin{aligned}
\bar{d}(\delta) &= \frac{1}{4\pi^2}\int_0^{2\pi}\int_0^{2\pi} d\phi_1\, d\phi_2\, \sqrt{2\delta^2(1-\cos(\phi_1-\phi_2)) - \frac{1}{6}R\delta^4\sin(\phi_1-\phi_2)^2} + O(\delta^3) \\
&= \frac{\delta}{4\pi^2}\int_0^{2\pi}\int_0^{2\pi} d\phi_1\, d\phi_2\, \left(\sqrt{2}\sqrt{1-\cos(\phi_1-\phi_2)} - \frac{R}{12\sqrt{2}}\delta^2\frac{\sin(\phi_1-\phi_2)^2}{\sqrt{1-\cos(\phi_1-\phi_2)}}\right) + O(\delta^3) \\
&= \frac{\delta}{4\pi^2}\left(\sqrt{2}\cdot 8\sqrt{2}\pi - \frac{R}{12\sqrt{2}}\frac{16\sqrt{2}\pi}{3}\,\delta^2\right) + O(\delta^3) \\
&= \delta\left(\frac{4}{\pi} - \frac{1}{9\pi}R\,\delta^2\right) + O(\delta^3).
\end{aligned} \tag{B.6}$$

This concludes the derivation.

B.2 Hausdorff dimension

In section 4.2 we discuss the local Hausdorff dimension and define it to be

$$d_H = 1 + \lim_{r\to 0}\frac{d\log\left(\left\langle\overline{\mathrm{Vol}\,S(r)}\right\rangle_V\right)}{d\log r}, \tag{B.7}$$

in a continuum setting. In a discrete setting we cannot take this limit $r \to 0$, so instead we used a power-law fitting procedure to extract d_H from the average sphere volume $\left\langle\overline{\mathrm{Vol}\,S(r)}\right\rangle$, as discussed in that section. However, we could take definition (B.7) and analyse it in the discrete setting of 2D CDT directly without considering the limit. We define a "quasi-local" Hausdorff dimension $d_H(r)$ for 2D CDT as

$$d_H(r) = \frac{d\log\left(\left\langle\overline{\mathrm{Vol}\,\mathcal{B}(r)}\right\rangle_N\right)}{d\log r}, \tag{B.8}$$

where the ensemble average is taken over the fixed-volume ensemble with two-volume $N_2 = N$. Note that we now use the volume of the full geodesic ball $\mathcal{B}(r)$ instead of its boundary, the sphere $S(r)$. We do this because we used the discrete ball volume in our measurements, but the same could be done for the sphere volume.

For our measurements we estimate the ensemble average using 1000 triangulations, where for each one the manifold average is estimated using 100 samples. The results of these measurements of $d_H(r)$ are presented in Fig. B.1. From the figure it seems clear that, after a region of discretization artefacts to about $r = 15$, a plateau is formed at around $d_H = 2.24$. This indicates that the start of this plateau may be reasonably used as an estimate of the $r \to 0$ limit. Doing so gives us the same estimate for the local Hausdorff dimension as presented in section 4.2. We can also consider $d_H(r)$ for larger r, although then it does not necessarily reflect the local Hausdorff dimension any more, and can contain curvature corrections. Zooming in on the plateau of $d_H(r)$ (see right of Fig. B.1) we can see a very slow decrease in $d_H(r)$. This might indicate that $d_H(r)$ is significantly smaller than 2.24 for very large r, but we clearly do not have the statistical accuracy to make conclusions about this long-distance behaviour. It could also be possible that this slight decrease is a non-trivial finite-size effect and that it will disappear in the infinite-volume limit.

B.3 Distance matrix ASD

For the measurements of many of the quantities we present in this thesis we need to be able to measure geodesic distance on the triangulation, which for our measurements is taken to be the

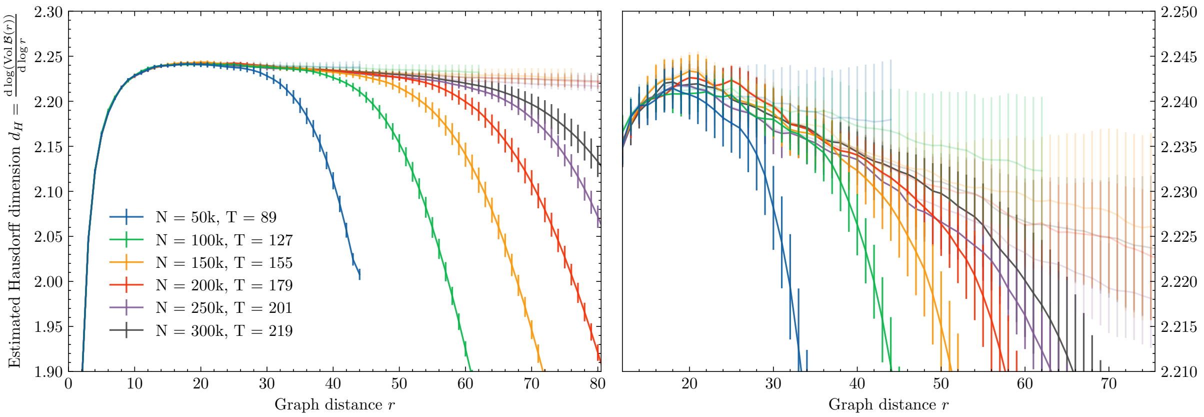

Figure B.1: "Quasi-local" Hausdorff dimension for several system sizes N_2, where the right figure is a zoomed-in version of the left. These figures also include the measurement results of the Hausdorff dimension as measured on the cut-open triangulation (see chapter 6) in lower opacity. The error bars show 95% confidence intervals.

link distance. This includes sphere volumes for the Hausdorff dimension, point pair sampling, and average sphere distance. If many of these quantities need to be measured for a significant number of the vertices of the triangulation, it may happen that one computes the distance between vertices several times over. In this case it could be useful to precompute the distance between all pairs of points in the triangulation and store them in a distance matrix. If one has such a distance matrix, this also allows one to perform uniform sampling of point pairs as discussed in section 7.1.4. Moreover, the average sphere distance can be easily computed from the distance matrix by making use of matrix multiplication, which can be done very efficiently on a computer. How this works is what we present here for a general graph G, where one can think of this graph as the vertex graph of a triangulation.

Given a finite graph G, let D be the distance matrix, such that

$$D_{ij} = d_G(i,j) \tag{B.9}$$

is the geodesic or link distance of the graph between node i and j. Let $S(r)$ be the binary distance-r matrix, such that

$$S_{ij}(r) = \begin{cases} 1 & \text{if } d_G(i,j) = r, \\ 0 & \text{otherwise.} \end{cases} \tag{B.10}$$

Thus, $S(r)$ acts like a mask of all elements of D that equal r, so we have that $\sum_r r\,S_{ij}(r) = D_{ij}$. With these matrices we can compute the discrete average sphere distance $\bar{d}_{ij}(\delta)$ (5.9) as

$$\bar{d}_{ij}(\delta) = \frac{\displaystyle\sum_{k,l} S_{ik}(\delta)\, D_{kl}\, S_{lj}(\delta)}{\displaystyle\sum_m S_{im}(\delta) \sum_n S_{nj}(\delta)} = \frac{\big(S(\delta)\, D\, S(\delta)\big)_{ij}}{\big(S(\delta)\, \mathbf{1}\, S(\delta)\big)_{ij}}, \tag{B.11}$$

where $\mathbf{1}$ represents the matrix where each element is 1. Note that $\bar{d}_{ij}(\delta)$ gives the average sphere distance $\bar{d}(S_i(\delta), S_j(\delta))$ regardless of the distance between i and j, specifically $d_G(i,j) = \epsilon$.

We see that it is possible to calculate the average sphere distance for all combinations of ϵ and δ between all pairs of points by performing a double matrix multiplication. Note that the size of the distance matrix is $N_0 \times N_0$, where N_0 is the number of nodes in the graph G. This means the number of matrix elements can get very large for the triangulations we consider. In fact, for a triangulation of $N_2 = 300\text{k}$ the distance matrix has 2.25×10^{10} elements. If we store each matrix element as a 16-bit integer, the resulting distance matrix has a size of 45 GB, which is higher than the computer memory we can easily access for our simulations. So if one wishes to use this distance matrix approach, one likely needs to resort to storing the distance matrix on disk, as we have done. Then, one can access the distance matrix data by reading one section at a time from disk. Only being able to read one section at a time is no problem, as a matrix product can easily be split up in a sum of matrix products of parts of the full matrix.

Consequently, if one wants to compute the average sphere distance for many or even all points in the triangulation, it can be very effective to precompute the distance matrix and compute the ASD from that. In addition, having this distance matrix allows one to perform other measurements using the distance without the need to compute those distances separately.

B.4 ASD midpoint

In section 8.1 we discussed that in order to measure two-point functions we need to associate a field value to each vertex p. If one wishes to use the average sphere distance $\bar{\mathrm{d}}_{\mathrm{q},\mathrm{q}'}(\delta)$ with $\epsilon = \delta$ as a field, this association is non-trivial. The average sphere distance $\bar{\mathrm{d}}_{\mathrm{q},\mathrm{q}'}(\delta)$ uses a coarse-graining region as given by the two spheres $S_{\mathrm{q}}(\delta)$ and $S_{\mathrm{q}'}(\delta)$. We need to choose a mapping of a point p to a coarse-graining region, such that each p maps to a unique region, i.e. we need to find a one-to-one map $\mathrm{p} \mapsto \big(S_{\mathrm{q}(\mathrm{p})}(\delta), S_{\mathrm{q}'(\mathrm{p})}(\delta)\big)$. A natural choice is to let p be the midpoint of the geodesic connecting q to q', because this is the closest to the "centre" of the coarse-graining region. However, this may not always be possible in a triangulation, as it can happen that a point is not the midpoint of any geodesic. To see this, imagine we wish to measure the ASD in the spatial direction, meaning we consider all δ-separated $(\mathrm{q}, \mathrm{q}')$ pairs with time separation 0. Then there can exist vertices like those in the configuration presented in Fig. B.2, which are not the midpoint of any geodesic, because the paths along the dashed blue lines are always shorter. Instead, one can choose to associate the point with the origin of either one of the spheres. Then we get the field, defined by the map $\mathrm{p} \mapsto \bar{\mathrm{d}}_{\mathrm{p},\mathrm{p}'}(\delta)$, where p' is a point at geodesic distance δ from p. Which p' is chosen is determined by the direction condition one wishes to impose, for example, the maximally spacelike separation we considered before. One could also choose a condition that allows for multiple p' points, in which case one could average over of all possible points p'.

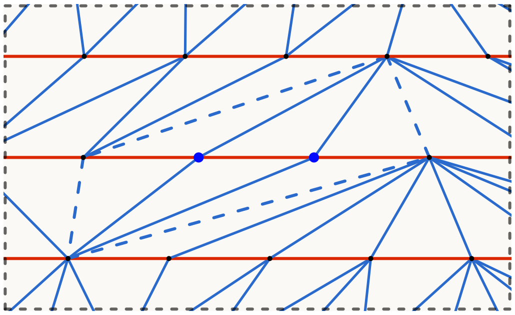

Figure B.2: Example of vertices (in blue) that are not midpoints of any geodesic with separation distance $\geqslant 2$ between maximally spacelike separated ($\Delta t = 0$) points. Note that spacelike edges are marked red and timelike edges are marked blue.

C. Additional figures

This section includes figures that support the main text, but would take up too much space when included in the main text body.

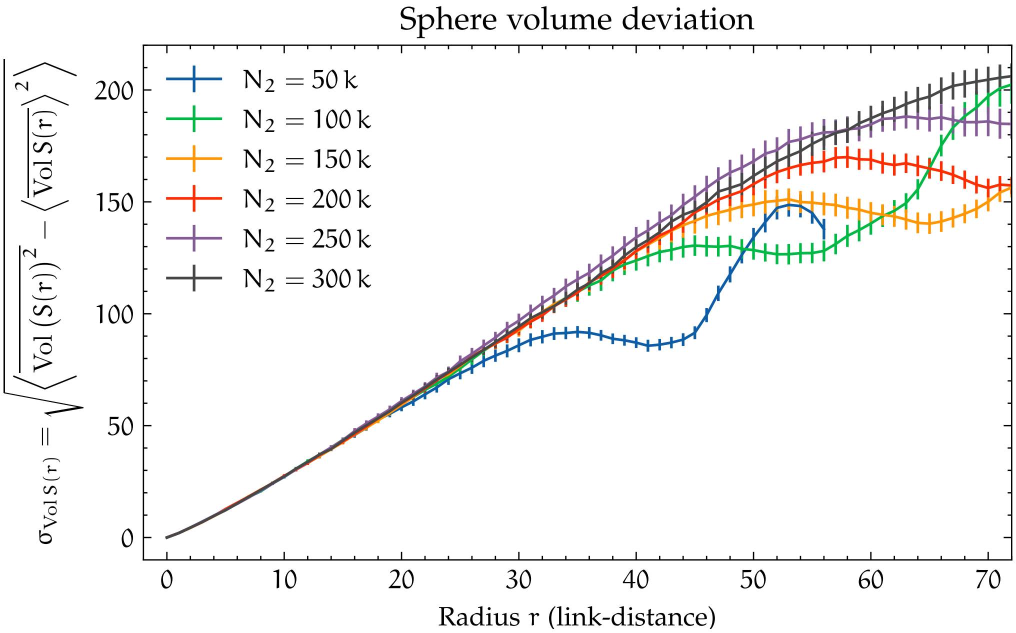

Figure C.1: Standard deviation of the sphere volume $\sigma_{\mathrm{Vol}\,S(r)}$ for 2D CDT, given by $\sigma^2_{\mathrm{Vol}\,S(r)} = \left\langle \overline{\mathrm{Vol}\,S(r)^2} \right\rangle_{N_2} - \left\langle \overline{\mathrm{Vol}\,S(r)} \right\rangle^2_{N_2}$. The measurements are performed at several volumes N_2 with $\daleth = \tau^2/N_2 = 0.32$ and show 95%-confidence intervals. This shows the standard deviation of the sphere volume $\mathrm{Vol}\,S(r)$ is independent of the total triangulation volume N_2 for r smaller than the effective linear size of the triangulation.

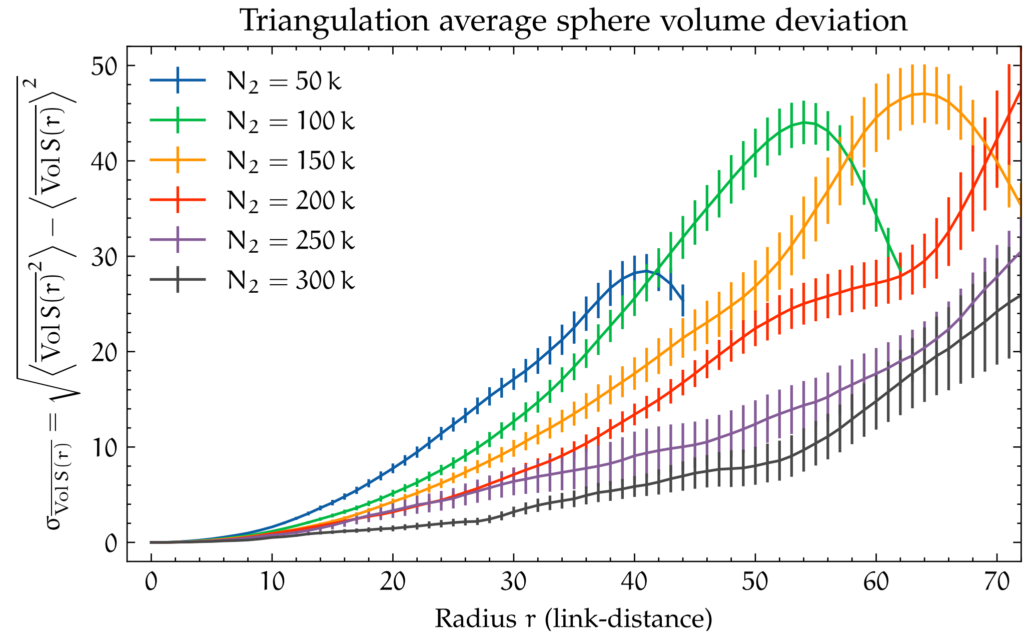

Figure C.2: Standard deviation of the manifold/triangulation average of the sphere volume $\sigma_{\overline{\mathrm{Vol}\,S(r)}}$ for 2D CDT, given by $\sigma^2_{\overline{\mathrm{Vol}\,S(r)}} = \left\langle \overline{\mathrm{Vol}\,S(r)}^2 \right\rangle_{N_2} - \left\langle \overline{\mathrm{Vol}\,S(r)} \right\rangle^2_{N_2}$. The measurements are performed at several volumes N_2 with $\daleth = \tau^2/N_2 = 0.32$ and show 95%-confidence intervals. This shows the standard deviation of the manifold/triangulation average of the sphere volume $\overline{\mathrm{Vol}\,S(r)}$ goes down with the triangulation volume N_2 for r smaller than the effective linear size of the triangulation.

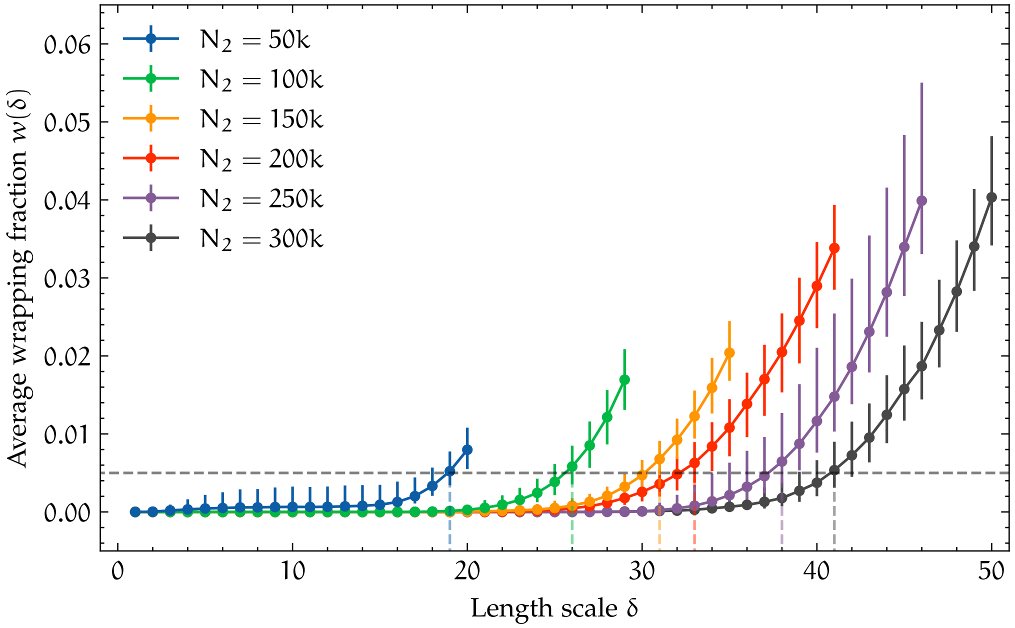

Figure C.3: Average wrapping fraction $w_{p,p}(\delta)$ (6.2) for average sphere distance $\delta_p(\delta)$ with $\epsilon = 0$ in 2D CDT with $\daleth = 0.32$. As an example, we include the $\delta_{\max}$ using a vertical dashed line for each triangulation volume N_2 for a maximum allowed wrapping fraction of $w(\delta_{\max}) = 5 \times 10^{-3}$ (this is a lot larger than what is actually considered an acceptable amount of wrapping effects). The error bars give a 95%-confidence interval.

Bibliography

[1] J. Ambjørn and R. Loll, 'Non-perturbative Lorentzian quantum gravity, causality and topology change', Nuclear Physics B **536**, 407 (1998), arXiv:`hep-th/9805108`.

[2] N. Klitgaard and R. Loll, 'Introducing quantum Ricci curvature', Physical Review D **97** (2018), arXiv:`1712.08847`.

[3] R. Loll, 'Quantum gravity from causal dynamical triangulations: a review', Classical and Quantum Gravity **37**, 013002 (2019), arXiv:`1905.08669`.

[4] J. Ambjørn, A. Görlich, J. Jurkiewicz and R. Loll, 'Nonperturbative quantum gravity', Physics Reports **519**, 127 (2012), arXiv:`1203.3591`.

[5] D. Benedetti and J. Henson, 'Imposing causality on a matrix model', Physics Letters B **678**, 222 (2009), arXiv:`0812.4261 [hep-th]`.

[6] J. Ambjørn, M. Carfora and A. Marzuoli, 'Triangulations', in *The geometry of dynamical triangulations* (Springer Berlin Heidelberg, Berlin, Heidelberg, 1997), pp. 17–37.

[7] J. Ambjørn, A. Görlich, J. Jurkiewicz, R. Loll, J. Gizbert-Studnicki and T. Trześniewski, 'The semiclassical limit of causal dynamical triangulations', Nuclear Physics B **849**, 144 (2011), arXiv:`1102.3929`.

[8] B. Ruijl, 'Locally causal dynamical triangulations', Master's thesis (Radboud University Nijmegen, 2013).

[9] J. F. Monahan, 'Markov chain Monte Carlo methods', in *Numerical methods of statistics*, 2nd ed., Cambridge Series in Statistical and Probabilistic Mathematics (Cambridge University Press, 2011), pp. 375–402.

[10] J. Ambjørn, B. Durhuus and T. Jonsson, *Quantum geometry: a statistical field theory approach*, Cambridge Monographs on Mathematical Physics (Cambridge University Press, 1997).

[11] N. Metropolis, A. W. Rosenbluth, M. N. Rosenbluth, A. H. Teller and E. Teller, 'Equation of state calculations by fast computing machines', The Journal of Chemical Physics **21**, 1087 (2004), eprint: `https://pubs.aip.org/aip/jcp/article-pdf/21/6/1087/8115285/1087\_1\_online.pdf`.

[12] J. Ambjørn, K. N. Anagnostopoulos and R. Loll, 'New perspective on matter coupling in 2d quantum gravity', Physical Review D **60** (1999), arXiv:`hep-th/9904012`.

[13] N. Klitgaard and R. Loll, 'Quantizing quantum Ricci curvature', Physical Review D **97**, `10.1103/physrevd.97.106017` (2018), arXiv:`1802.10524`.

[14] J. Ambjørn, K. Anagnostopoulos and R. Loll, 'Crossing the c=1 barrier in 2d Lorentzian quantum gravity', Physical Review D **61** (2000), arXiv:`hep-lat/9909129`.

[15] J. Barkley and T. Budd, 'Precision measurements of Hausdorff dimensions in two-dimensional quantum gravity', Classical and Quantum Gravity **36**, 244001 (2019), arXiv:`1908.09469`.

[16] J. Ambjørn, J. Jurkiewicz and Y. Watabiki, 'On the fractal structure of two-dimensional quantum gravity', Nuclear Physics B **454**, 313 (1995), arXiv:`hep-lat/9507014`.

[17] R. Loll and B. Ruijl, 'Locally causal dynamical triangulations in two dimensions', Physical Review D **92** (2015), arXiv:`1507.04566`.

[18] D. Vassilevich, 'Heat kernel expansion: user's manual', Physics Reports **388**, 279 (2003), arXiv:`hep-th/0306138 [hep-th]`.

[19] D. Benedetti and J. Henson, ‘Spectral geometry as a probe of quantum spacetime’, Physical Review D **80**, `10.1103/physrevd.80.124036` (2009), arXiv:`0911.0401 [hep-th]`.

[20] B. Durhuus, T. Jonsson and J. F. Wheater, ‘On the spectral dimension of causal triangulations’, Journal of Statistical Physics **139**, 859 (2010), arXiv:`0908.3643`.

[21] Y. Ollivier, ‘Ricci curvature of Markov chains on metric spaces’, (2007), arXiv:`math/0701886 [math.PR]`.

[22] J. Brunekreef and R. Loll, ‘Quantum flatness in two-dimensional quantum gravity’, Physical Review D **104**, `10.1103/physrevd.104.126024` (2021), arXiv:`2110.11100`.

[23] R. Loll, ‘Quantum curvature as key to the quantum universe’, 2023, arXiv:`2306.13782 [gr-qc]`.

[24] J. Brunekreef and R. Loll, ‘Curvature profiles for quantum gravity’, Physical Review D **103**, `10.1103/physrevd.103.026019` (2021), arXiv:`2011.10168`.

[25] J. Ambjørn, J. Jurkiewicz and P. Bialas, ‘Connected correlators in quantum gravity’, Journal of High Energy Physics **1999**, 005 (1999), arXiv:`hep-lat/9812015`.

[26] P. Bialas, ‘Correlations in fluctuating geometries’, Nuclear Physics B - Proceedings Supplements **53**, Lattice 96, 739 (1997), arXiv:`hep-lat/9608029`.

[27] B. V. de Bakker and J. Smit, ‘Two-point functions in 4D dynamical triangulation’, Nuclear Physics B **454**, 343 (1995), arXiv:`hep-lat/9503004`.

[28] A. Silva and J. van der Duin, in preparation.

[29] N. Klitgaard, ‘New curvatures for quantum gravity’, PhD thesis (Radboud University Nijmegen, 15th Apr. 2022), eprint: `https://www.ru.nl/highenergyphysics/theses/phd-theses/`.

[30] L. C. Brewin, ‘Riemann normal coordinates’, Department of Mathematics Preprint, Monash University, Clayton, Vic. 3168. Also available online at `https://users.monash.edu.au/~leo/research/papers/files/lcb96-01.pdf`, 1997.